ISSN 1880-8468

Technical Report of
International Development Engineering

国際開発工学報告

TRIDE-2013-02 March 1, 2013

Abstracts of Bachelor Theses
Presented in March 2013

Department of International Development Engineering,
Graduate School of Science and Engineering,
Tokyo Institute of Technology
http://www.ide.titech.ac.jp/TR

Preface

Bachelor theses of Department of International Development Engineering, Tokyo Institute of Technology were presented successfully on August 3, 2012, March 1, 2013. This technical report consists of the abstracts of those theses.

Technical Report of International Development Engineering
TRIDE-2013-03b

Table of Contents

E-Learning System Based on Wisdom of Crowds on Android and its Vietnamese Version

Students Number: 08_20565 Name: Huynh Dao Hoang Nam Supervisor: Yukihiko Yamasita

July 31, 2012

1 Introduction

E-learning (consisting of electronic learning) comprises all forms of electronically supported learning and teaching. The information and communication systems, whether networked or not, serve as specific media to implement the learning process. In recent years, with the increase of the importance with e-learning, not only in Japan or Vietnam, but also in many countries, more and more people study by e-learning. However we have been facing with large problems in the creation or management of teaching materials.

The tobe (Text Oriented Bi-stream Explanation) system may solve those problems with wisdom of crowds. However, PC is necessary to learn by the tobe system. As a result, we can not use it when we are on the way to school or company.

I focus on the increase of use of the tablet and smartphone and the highest share of Android OS. N. Takemura made a tobeML player on Android devices [1]. In this paper, I improve the system by multilingualization and pointing function to highlight an important area.

2 Tobe System

Tobe system is an e-learning system for which anyone can make the contents. The contents are described using tobeML (tobe markup language). The process of creating and studying contents is as follows:

1. Creators all over the world describe the tobeML documents using text editor on the web.
2. The tobeML documents are stored in the server.
3. Users receive the tobeML documents from the server, and load them into Expositor (Figure 1), that is a lecture style player of tobeML documents.

The format of tobeML documents is based on XML. A virtual teacher in Expositor can point an important area in text or figure and read the explanation.

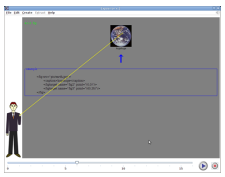

Figure 1: Expositor

3 Tobe Player on Android

There are two main reasons that I use Android devices for my research.

1. It is the most popular mobile OS in the world. Its share 79.6 % in Japan[2] and 28.7 % in Vietnam[3].
2. Its applications can be developed by Java.

Table 1:
Worldwide Share of OS Smartphone in 2012Year[4]

No	Company	4Q12 Units	Share(%)	4Q11 Units	Share(%)
1	Android	81,067.4	56.1	36,350.1	36.4
2	iOS	33,120.5	22.9	16,883.2	16.9
3	Symbian	12,466.9	8.6	27,598.5	27.7
4	RIM	9,939.3	6.9	13,004.0	13.0
5	Bada	3,842.2	2.7	1,862.2	1.9
6	Microsoft	2,712.5	1.9	2,582.1	2.6
	Others	1,242.9	0.9	1,495.0	1.5
	Total	144,391.7	100.0	99,775.0	100.0

In order to realize e-learning in mobile environment, I develop a tobeML player on Android devices.

3.1 Text To Speech

We use Text To Speech (TTS) to generate speech from text. This system sends text data to Google Translate, and gets mp3 data from there. We can play and save that mp3 date on the device. Furthermore, we can replay the data even when we cannot connect device to Internet. TTS in Google Translate can deal with a lot of languages. Android has an own TTS system. However, its quality is not so high and the number of languages is fewer. Therefore, I used Google Translate for my system. In my research, I conducted experiments in English, Japanese, and Vietnamese.

3.2 Structure of the player

In Figure 2, we can review the structure of the main window of player.

Figure 2: Display of this System

1. Image Area: Show the image to explain the text.
2. Teacher: Virtual teacher can point an important area in image.
3. Text Area: Show the text.
4. Play Button: Start speech.
5. Back Button: Return to the previous slide.
6. Next Button: Skip to the next slide.
7. Language Button: Change the language.

In this program, we use some important methods and resources as follows:

- onCreate(): This method is called at first when the application starts.
- onClick(): This method is called when a button is clicked.
- getHttpRequestFile(): This method is called when this application sends the text to Google Translate. Its return is an mp3 file.
- setLocale(): This method is called to specify the locale of the response.
- invalidate(): If this method is called, onDraw method will be called again. In this application, it is used to reload the language in the same page when we want to change language.
- Toast.makeText(): A toast notification is a message that pops up on the surface of the window.
- Canvas.Drawline(): Draw a line segment with the specified start and stop points in (x,y) coordinates, using the specified paint. In this application, I use to draw the pointer of teacher.

The process to use the proposed system is as follows:

1. Install this application.
2. Set the resources (texts, texts for speech, images, coordinations of lines)
3. Start and choose a language, and a content.
4. Push the button to play, back, or skip.
5. Push 'Language' button if you want to change the language.
6. Delete mp3 file if you want to renew the content of that file.

In the language selection, if you click "OK" button without selection, "Please select a language" is displayed in the bottom.

4 Evaluation Experiment

I had taken the survey to evaluate the proposed system by 8 subjects. Result is as follows:

- Good point:
  - With using sounds, pointing and multilingualization, it is easy understanding.
  - We can change language at the same slide.
- Points to improve:
  - Pronunciation of Vietnamese is not so good.
  - The size of text or image should be increased.
  - The system should proceed to the next slide automatically.

5 Conclusions

I have discussed on tobeML player on Android that is an e-Learning system using wisdom of crowds, and I have developed it on Android. With using images, texts and sounds, and pointing an important area, it enabled easy understanding comparing to text only or English only system. We totally can use this system not only for e-learning but also for the manual of products, sharing of the information, or distance training.

References

[1] N. Takemura, *"E-Learning System based on wisdom of crowds on Android"*, Master thesis, Tokyo Tech, 2012 .

[2] Gartner News, *http://www.gartner.com/*,

[3] VietNam marketing, *http://marketing.24h.com.vn*,

[4] ITMedia, *http://www.itmedia.co.jp/*,

[5] Google Translate, *http://translate.google.co.jp/*,

[6] Android Learning, *http://developer.android.com/*,

[7] Jakarta Project, *http://www.jajakarta.org/*.

Titan Aerocapture for Saturn Orbit Insertion

Student Number: 08B21381 Name: Seiya Furuki Supervisor: Yoshihiro Mochimaru

1. Introduction

Saturn and its moons have many mysterious points. Particularly, Titan, one of Saturn's moons, is the only one , except for Earth, that has a dense atmosphere and a dynamic climate system in our solar system.

In order to observe a planet from an orbit around it, a spacecraft is required to reduce its speed from hyperbolic. Conventionally, thrusters are used to reduce the speed. However, the method requires much extra propellant. Since specific impulse of the chemical rocket is not so large, the ratio of propellant mass to total mass becomes large, which leads to reduction of the payload mass.

For planets having atmosphere, it is possible to use a technique called aerocapture, shown in Fig. 1. Aerocapture is a technique to reduce a spacecraft speed by aerodynamic drag. This technique could drastically reduce to required propellant mass. However, the spacecraft during atmospheric entry receives severe aerodynamic heating. Moreover, the range of entry angle for aerocapture is very narrow, and accurate control of flight trajectory is required.

As for Saturn, it is possible to reduce a spacecraft speed by Titan aerocapture as shown in Fig. 2. Saturn aerocapture for orbit insertion around Saturn requires an acceleration to prevent the spacecraft from atmospheric entry. Titan aerocapture for orbit insertion around Saturn does not requires an the maneuver.

This study compares the Titan aerocapture with Saturn aerocapture for an orbit insertion around Saturn.

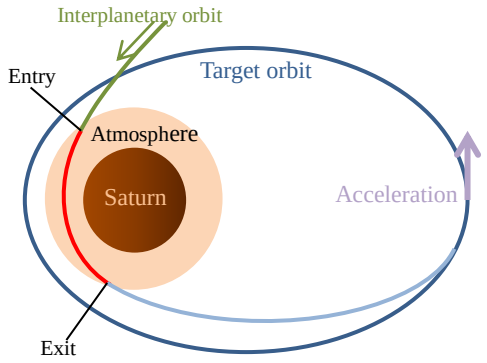

Fig. 1 Aerocapture

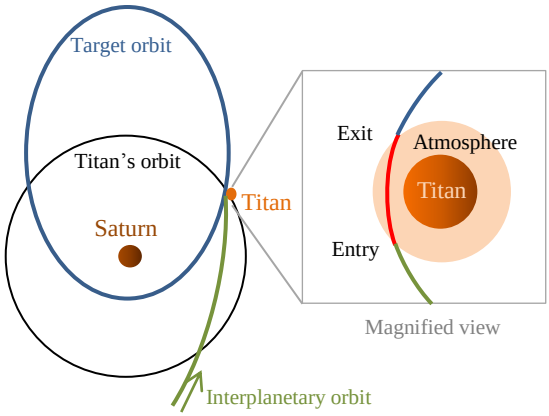

Fig. 2 Titan aerocapture for orbit insertion around Saturn

2. Flight trajectory calculation method

2.1 Trajectory during atmospheric entry

Forces on the spacecraft are modeled as shown in Fig. 3. Equations of motion are given by

$$\frac{dr}{dt} = -v\sin\theta \tag{1}$$

$$\frac{d\varphi}{dt} = \frac{v}{r}\cos\gamma \tag{2}$$

$$\frac{dv}{dt} = g\sin\theta - \frac{1}{2}\rho v^2\frac{1}{\beta} \tag{3}$$

$$\frac{d\gamma}{dt} = \left(\frac{g}{v} - \frac{v}{r}\right)\cos\theta \tag{4}$$

$$\beta = \frac{m}{C_D S} \tag{5}$$

where v is the velocity of spacecraft, θ is the flight path angle, r is the distance from the center of planet, ρ is the atmospheric density, m is total mass of the spacecraft, S is the frontal area, C_D is drag coefficient, and β is the ballistic coefficient. The equations of motion are calculated by using Runnge-Kutta method.

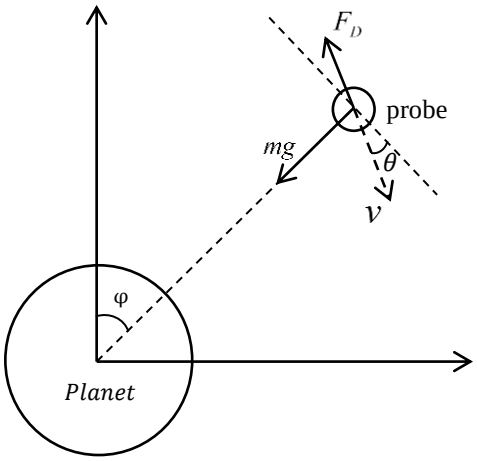

Fig. 3 Trajectory calculation model during atmospheric entry

2.2 Aerodynamic heating estimation

The heating rate $\dot{q}$ W/m^2 are given from the folloing equations

Saturn aerocapture

$$\dot{q} = 0.25\times\frac{\rho}{\sqrt{R_N}}\times v^3 \tag{6}$$

Titan aerocapture

$$\dot{q} = 1.35\times10^{-4}\times\sqrt{\frac{\rho}{R_N}}\times v^{3.04} \tag{7}$$

where v is the velocity of spacecraft, ρ is the atmospheric density, and R_N is the nose radius.

3. Flight trajectory calculation results

3.1 Saturn aerocapture for Saturn orbit insertion

Figure 4 shows the peat heat flux for various entry velocities and entry angles. The ballistic coefficient is$10.0\ \mathrm{kg/m^2}$. The aerocapture is not available at entry conditions in black area in Fig. 4.

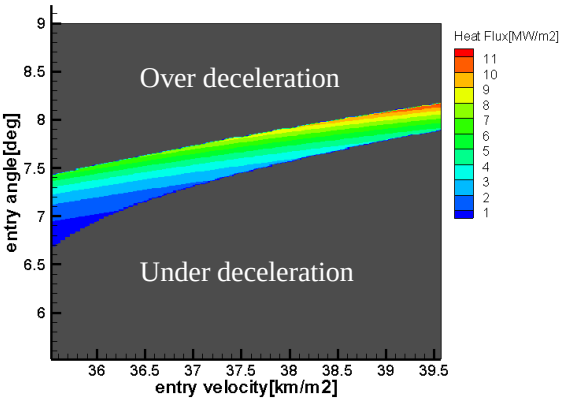

Fig. 4 Peak heat flux at Saturn aerocapture

3.2 Titan aerocapture for Saturn orbit insertion

An angle between the velocity vector of a probe and the revolution velocity vector of Titan is γ. Figures 5-7 show the peak heat flux for various entry velocities and entry angles. The ballistic coefficient is $10.0\ \mathrm{kg/m^2}$. The aerocapture is not available at entry conditions in black area in Figs. 5-7. The aerodynamic heating increases with γ. The range of entry corridor increases with γ.

Table 1 shows comparison between Saturn and Titan aerocapture for orbit insertion around Saturn.

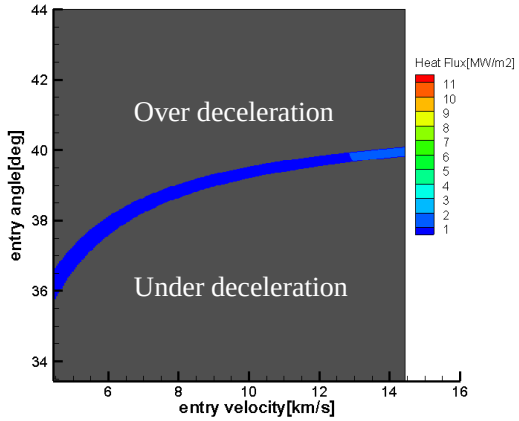

Fig.5 Peak heat flux at Titan aerocapture (γ =0.0 deg)

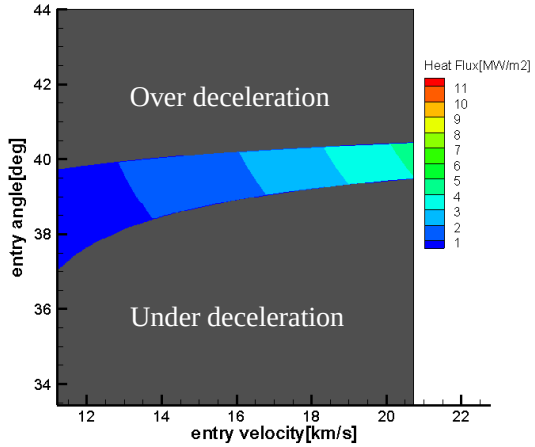

Fig.6 Peak heat flux at Titan aeroocapture (γ =90.0 deg)

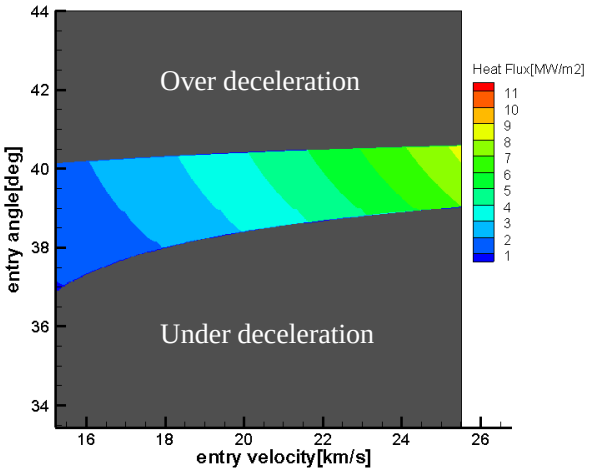

Fig.7 Peak heat flux at Titan aerocapture (γ =180.0 deg)

Table 1 Comparison between Saturn and Titan aerocapture

	Saturn	Titan
Aerodynamic heating	0.36~11.0 $\mathrm{MW/m^2}$	0.03~8.28 $\mathrm{MW/m^2}$
Aerocapture corridor	0.26~0.73 deg	0.25~3.2 deg

4. Conclusion

Titan aerocapture for Saturn orbit insertion has advantages, compared with Saturn aerocapture, in the aerodynamic heating during atmospheric entry and in the range of atmospheric entry corridor. Additionally, Titan aerocapture for Saturn orbit insertion does not require an acceleration at apoapsis, so that the spacecraft does not need a propulsion system.

References

[1] Hiroshi Hirayama, “The slowdown of Saturn probe using the Titan atmosphere”, Bachelor Thesis, 1991

[2] Eiko Nakazawa, “Feasibility Study on Low Bllistic Coefficient Aerocapture Vehicle with Membrane Decelerator for Planetary Exploration”, Master Thesis, Tokyo University, 2003

[3] Kumiko Nakamura, “Feasibility of the low ballistic coefficient aerocapture satellite in Saturn”, Master Thesis, Tokyo University, 2006

[4] M. E. Tauber, and J. V. Bowles, “Use of Atmospheric Braking During Mars Missions”, Journal of Spacecraft and Rockets, vol. 27, Sept-Oct, 1990, p. 514-521

[5] Toshio Kawasaki, “Thieory and technology or astronautics”, chijinnsyokann, 1986

Freight mode choice from Vietnam to Thailand

School register: 09B20278, Name: Vu Mai Phuong, Supervisor: Dr. Shinya Hanaoka

1. INTRODUCTION

ASEAN is one of the largest export markets of Vietnam. According to Vietnam general statistics (2011), about 14% of export turnover is generated from ASEAN export.

Sea transport is the most popular transport to transfer cargo from Vietnam to Thailand. Road transport does not gain sufficient attraction. One reason of low popularity of road transport is crossing third country border. This situation is changing with the opening of East-West Economic Corridor (EWEC). EWEC connects Vietnam, Laos, Thailand and Myanmar (Figure 1).

Figure 1 Vietnam-Thailand route

The cargo transport cost by road from Hanoi, Vietnam to Bangkok, Thailand is more than twice as transported by sea mode. However, road transport is 3 times faster than sea transport. Therefore, sea transport will retain its advantage in bulk transport, but because of rapidity, expectation for road is high.

This research aims to find out the reasons why shippers and logistics companies use route between road and sea, through data analysis, estimation designing mode choice model with stated preference (SP) data and qualitative survey.

2. DATA COLLECTION

(1) Data analysis

The export statistics from Vietnam to Thailand in December, 2011was collected from Vietnam general administration of customs. It has 14,639 samples and each sample includes: custom, border, mode and item. In Vietnam, products are declared in the custom, transported through the border and to Thailand.

(2) Estimation

A SP survey with assumption that there are two routes to transport a container cargo from Hanoi (or Northern Vietnam) to Bangkok. Two routes are differed in terms of mode (road and sea), shipment expense per FEU including customs, average shipment time and customs procedure. Actual, it takes 3 days and 3800$/FEU to transport cargo by road, 10 days and 2000$/FEU to transport cargo by sea. Cost and time of these routes of SP survey are designed based on these values.

Contact with 16 companies and request them to choose one route which they prefer to transport.

(3) Qualitative survey

Interview 14 companies to answer these below questions:

(a) In mode choice from Vietnam to Thailand, is there any specific factors more than time and cost?
(b) Why do you choose road rather than sea?
(c) Why do not you choose road rather than sea?
(d) How to make shippers change their choice from sea transport to road transport?
(e) What kind of goods do you transport by mainly road or mainly sea? Why?
(f) If you choose road transport, which route do you choose?
(g) Is there the route of road transport that cross the border of Lang Son? Why?

3. RESULTS

(1) Data analysis results

Table 2 shows the ratio of samples of export from each region to Thailand by different transports in December, 2011.

Table 2 Export from Vietnam to Thailand

	North	Middle	South	Total
Road	26.8%	10.4%	0.2%	8.8%
Sea	64.8%	71.9%	87.6%	80.2%
Air	8.2%	13.1%	10.9%	10.0%

The ratio of export by sea transport is biggest (about 80% and 65% for northern) and the ratio of export by road transport is small (about 9% and 27% for northern).

When companies use road transport, the main borders of middle region are: Cau Treo (HaTinh), Cha Lo (QuangBinh) and Lao Bao (Quang Tri). Notice to cargo of northern and middle region, from data table, we can see that the ratio of transport that go through Cha Lo border is 88%. The ratio that goes through Lao Bao and Cau Treo is very few (only 6% for each border).

Data table also shows types of goods that transported by road. They're farm product, clothes, paper product, plastic product (e.g. shoe, bag), metal product (e.g. accessory), watch, motorbike.

(2) Estimation of mode choice model

Make utility functions as below:

$V\_R = \alpha + \beta_C * R\_Cost + \beta_T * R\_Time$ (1)

$V\_S = \beta_C * S\_Cost + \beta_T * S\_Time$ (2)

(α, β_C, $\beta_T$are are coefficients to be estimated.
R_Cost, R_Time, S_Cost, S_Time which are the two variables of the model associated with each alternative.)

Model was executed by open source software biogeme. We get the following output:

Table 3 Results of mode choice model

Name	Value	t value	Standard error
α	-2.2700	-0.59	3.820
β_C	-0.0053	-5.58	0.001
β_T	-0.6800	-1.15	0.593
Null log-likelihood			-88.728
Final log-likelihood			-37.709
Rho-square			0.575
Adjusted rho-square			0.541
Number of samples			128

From the value of Rho-square, we can judge that model can explain the real mode choice well.

The sign of value of β_C and β_T is minus. It means there will be a negative impact to the selection, when value of cost or time is increased.

Absolute value of t of β_C is greater than 1.96. It means that cost is a significant variable. Absolute value of t of β_C is smaller than 1.96, so it means that time is not significant.

(3) Results of qualitative survey

(a) In general, cost is the most important factor and followed by customs procedure, safety and infrastructure.
(b) Reasons of choosing road rather than sea are quick lead time, high frequency, flexibility the time shipment. Besides, they can delivery in many places.
(c) However they have also many reasons to not choose road rather than sea. For example: high expense, complex of customs procedure, lack of safety, one-way cargo, not good quality road (especially Laos), custom (accustomed to sea transport), unstable political situation in Thailand.

Shipper and logistics companies regard road transport as an alternative to other transports. The reasons of using one route between road and sea is: at that moment, shippers focus on what kind of factor. For example, in emergency case, to keep up progress, they choose road transport or even air transport regardless of very high cost. Other reasons that mentioned such as: type of goods, spot of starting point and destination, amount of cargo.
(d) To make shippers change their choice from sea transport to road transport, many companies answer that the most important factor is reduce the cost of road transport. It is also necessary to simplify customs procedure, improve infrastructure, persuade shipper (through advertisement, increase performance).
(e) Types of goods that they transport by road are farm product (need fast transport), car, motorbike (high price product). Almost goods can be transported by sea.
(f) Relate to borders, according to companies, currently, mainly used borders are Cau Treo border and Lao Bao border. Logistics companies are familiar with which customs and border police, they will choose that border. Beyond that, they also consider based on spot of starting point and destination. Because newly completed, Cha Lo border is not yet known, but it is expected to this border will develop from now on.
(g) Border of Lang Son: Many cargos from China are transported to Thailand via by road transport.

4. CONCLUSION

The most important factor of choosing route between road and sea is cost. In current situation, shipper and logistics companies choose road transport only in emergency case and regard road transport as an alternative to other transports. Improvement of cost and procedure will bring high expectation for road.

REFERENCES

1) Import – export department [Accessed 1. 2012].
2) General administration of customs [Accessed 2. 2012].
3) General statistics office [Accessed 6. 2012].
4) Ministry of the industrial and commercial [Accessed 6].

Fundamental Study on Proposed Efficient Repair with Combination of Electro-chemical Methods

ID: 04-09083　Name: Daisuke KUNIOKA　Supervisor: Prof. Nobuaki OTSUKI

1. Introduction

Steel bars in reinforced concrete (RC) are easily corroded by the influence of carbonation and chloride ion. It can cause cracks, and if cracks are not repaired, it leads to further structural deterioration. In early stage of deterioration, there are no cracks on the surface of RC, but causes of corrosion are contained in it. They have to be removed from RC. Therefore, different repairing method should be applied according to the presence of cracks.

Realkalization, Desalinatin and Electrodeposition are the kind of electro-chemical method. Realkalization is the method to recover pH of RC. Desalination is the method to remove inner chloride ion. Electrodeposition is the method to close cracks and coat surface with electrodeposits. Those three methods are based on the same electro-chemical system, which is the electrification between inner steel bars and external anode with solutions. Hence, if they are combined, it is expected that repair of concrete is achieved efficiently by using the common equipments. Also, by using the combination of electro-chemical methods, it is expected that the effect of each method will be highly enhanced. However, the removing effect of corrosion factors is not clarified enough. Hence, the objectives of this study are as follows.

1) To clarify influence of solution type on the removal effect of corrosion factors such as chloride ion or pH degradation.
2) To propose the most efficient electro-chemical combination method against chloride attack and carbonation.

2. Experimental procedure

2.1 Specimen

Mortar specimens in prism shape (40mm×40mm×160mm) were used in this research. Steel bar embedded in mortar was located at 15mm from mortar surface. Table 1 shows types of specimen.

Table.1: Types of specimen

Causes of corrosion	Presence of cracks	
	without cracks	with cracks
Carbonation	Carbonated	Carbonated
Chloride attack	Chloride ($4kg/m^3$)	Chloride ($8kg/m^3$)

2.2 Evaluation

Effectiveness of repair was evaluated from four points of view.

① Characteristics of electrodeposits
② Removing effect of causes of corrosion
③ Improvement of resistance to permeation
④ Protecting effect against corrosion of steel bars

2.3 Pattern of combination

Table.2 shows the solution used for each method; and Table.3 shows the pattern of combination. Pattern 1, 2 and 3 were applied for both specimens with crack and specimens without crack. Pattern 4 and 5 were applied only for specimen with crack. Electrification was conducted for one week in each step. After the repair, carbonated specimens were exposed to carbonation, and chloride attacked specimens were submerged into 3.5% NaCl aq, so that to evaluate the resistance to permeation.

Table.2: Solutions used for each method

Method	Solutions	Concentration
Realkalization	K_2CO_3 aq	0.5(mol/L)
Desalination	Li_3BO_3 aq	2N
Electrodeposition	$Mg(CH_3COO)_2$ aq	0.1(mol/L)

Table.3: Patterns of combination

	Step 1 (for a week)	Step 2 (for a week)	Step 3 (for a week)
Pattern.1	ED		
Pattern.2	Re or De		
Pattern.3	Re or De	ED	
Pattern.4	ED	Re or De	
Pattern.5	ED	Re or De	ED

ED: Electrodeposition　Re: Realkalization
De: Desalination

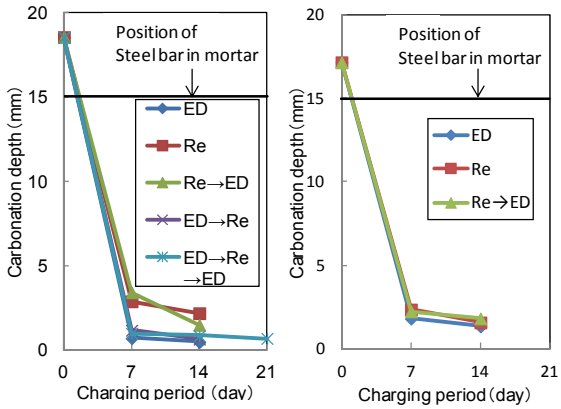

(a) with crack (b) without crack

Fig.1 Changes of carbonation depth during repair (W/C=0.55, carbonation)

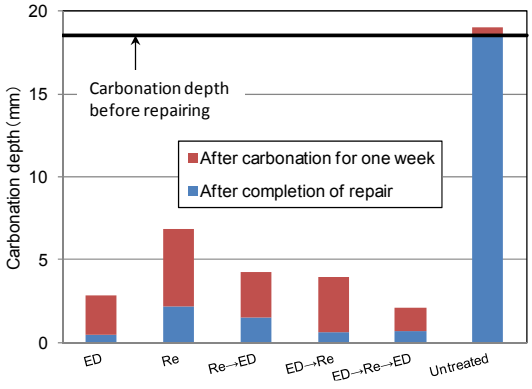

Fig.2 Increase of carbonation depth by carbonation after repairing (W/C=0.55, with crack, carbonation)

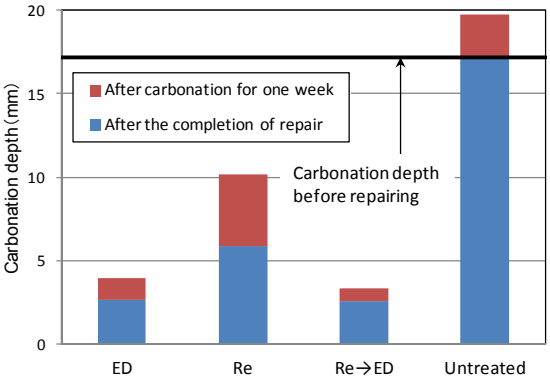

Fig.3 Increase of carbonation depth by carbonation after repairing (W/C=0.55, without crack, carbonation)

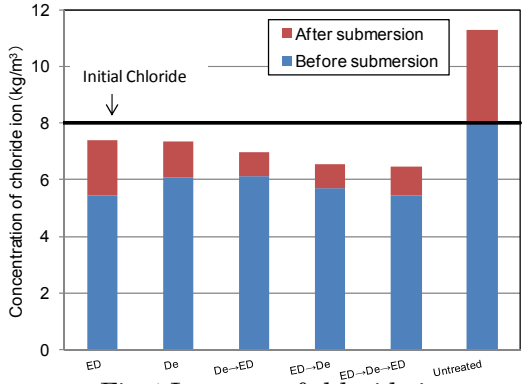

Fig.4 Increase of chloride ion by submersion test after repairing (W/C=0.55, with crack, chloride attack)

3. Experimental result

3.1 Carbonation

Carbonation depth decreased regardless the pattern of combination or solution type as shown in Fig 1. This tendency was also observed in the case of specimen without crack. It means that the realkalizing effect is almost the same in each pattern regardless the presence of crack.

Fig 2 shows the increase of carbonation depth by carbonation after repairing of specimens with crack, and Fig 3 shows that of specimens without crack. The resistance to permeation of CO_2 is highly improved by repair. Especially, in the case of specimens with crack, when the pattern "ED→Re→ED" is applied, the resistance became highest. In the case of specimens without crack, pattern "Re→ED" obtained highest resistance. These results are shown in Table 4.

3.2 Chloride attack

The removing effect of chloride ion had almost same tendencies as realkalizing effect against carbonation; that means solution type and pattern of combination has very little influence on the removing effect.

The resistance to permeation of chloride ion was improved by repair compared with untreated specimen as shown in Fig 4. Especially, by applying combination pattern, the resistance became higher.

These tendencies were also observed in the case of specimen without crack.

Table.4: Most effective combination for each corrosion type

Causes of corrosion	Presence of cracks	
	without crack	with crack
Carbonation	Re → ED	ED → Re → ED
Chloride attack	De → ED	ED → De or ED → De → ED

4. Conclusions

1) The influence of solution type on the removal effect of corrosion factors such as pH degradation or chloride ion is small and this effect is followed by charging periods.
2) The most effective combinations of electro-chemical repair method for carbonation can be proposed as listed in Table 4. For chloride attack, combination pattern is more effective than each single electro-chemical method.

5. Reference

1) Hitoshi AKIYAMA: An Experimental Study on Closure of Cracks and Removal of Chloride Ion by Combining Electrodeposition and Desalination; bachelor thesis, Tokyo institute of technology, 2007.2

Adhesion Phenomemon between Rigid Body and Tapering Elastic Beam

Student number: 04B04387 Name: Boqing Wang Supervisor: Kunio TAKAHASHI

1 Introduction

Geckos have micro,nano-hierarchical hair structure, i.e. setas and spatulas, on their feet. They use them to climb wall and move on ceiling[1]. Therefore the adhesion mechanism of gecko's foot hair is important for the design of grip-and- release applications.

In order to analyse the adhesion mechanism of the hair structure, Sekiguchi assumed the hair to be an elastic beam of cuboid shape [2], and considered elastic energy, surface energy to discuss the adhesion force between the elastic beam and rigid body. But, in actuality, gecko's foot hairs are not cuboid, therefore, analysis of the effects of the beam shape on adhesion is significant for understanding adhesion mechanism of the hair structure.

In this study, a model of tapering elastic beam was constructed. Elastic energy, surface energy and shape of the beam are considered to analyse the phenomemon of adhesion between rigid body and the elastic beam.

2 Model of tapering elastic beam contact with rigid body

Figure 1 shows that an elastic beam contacts with rigid body at static condition. Slope at root of the beam is defined as θ and θ is infinitesimal. There are two kinds of contact at this model: line contact and area contact Fig.1 (a), (b). Force acted on the beam is defined as f_z. Displacement of the beam is defined as d and the origin of d is defined at the surface of the rigid body. Length of non-adhesion area of the beam is defined as l in case of area contact.

Length, width and height of elastic beam are L, W and H, the moment of intertia of area is I Fig2. (a). Height and moment of intertia of area at the root of beam is H_0 and I_0. The surface of beam which contacts with rigid body and the surface of rigid body are flat. In order to get a general result, H is defined as

$$H = H_0(1 - x/L)^{n/3}, n \geq 0 \qquad (1)$$

Neutral axis of beam is considered as straight line, thus moment of intertia of area can be defined by Linear beam theory[3] as

$$I = I_0\left(1 - \frac{x}{L}\right)^n \qquad (n \geq 0) \qquad (2)$$

By using eq. (2), the relation between length and moment of intertia of area can be drawn as Fig2. (b). By using eq. (1) we can know the shape of the beam as Fig2. (c) when n=0,n=1,n=3.

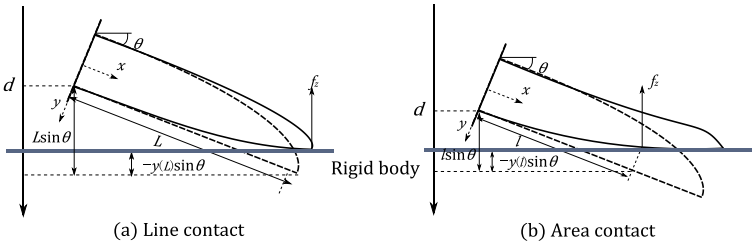

Fig.1 :Model of the contact between an elastic beam and a rigid body

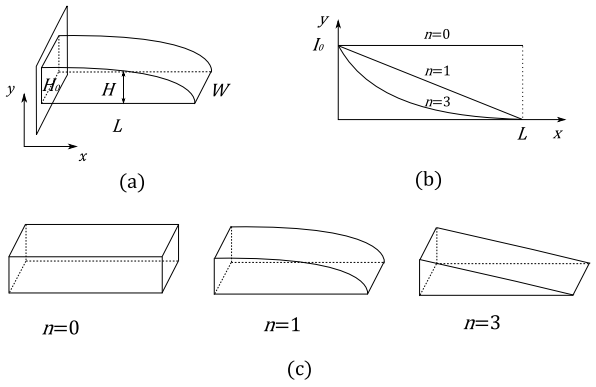

Fig.2: Image of model of tapering elastic beam

3 Relation between adhesion force and displacement of beam

At line contact Fig2. (a), by using flexure of beam by Linear beam theory[3] and geometric relation between beam and rigid body, relation between displacement and force can be calculated as

$$\tilde{f}_z \frac{\cos\theta}{\tan\theta} = \frac{3-n}{12}\left(\frac{\tilde{d}}{\sin\theta} + 1\right) \quad (3)$$

Where, $\tilde{f}_z = f_z/(12EI_0/L^2)$, $\tilde{d} = d/L$.

When the slope at the tip of the beam equals θ, the line contact will become area contact. At this moment displacement and force is

$$\left(\frac{\tilde{d}}{\sin\theta}, \tilde{f}_z \frac{\cos\theta}{\tan\theta}\right) = \left(\frac{1}{n-3}, \frac{2-n}{12}\right) \quad (4)$$

At area contact Fig2. (b), elastic energy of beam and surface energy can be defined as U_{elastic} and U_{surface} as

$U_{\text{elastic}} = \int_0^l \frac{{M_x}^2}{2EI} dx$, $U_{\text{surface}} = -\Delta\gamma(L-l)W$

E:Young's modulus, M_x:bending moment, $\Delta\gamma$: work of adhesion per unit area.Total energy of this model can be defined as U_{total}

$$U_{\text{total}} = U_{\text{elastic}} + U_{\text{surface}}$$

Length of non-adhesion area l settled at minimum of total energy

$$\frac{\partial U_{\text{total}}}{\partial l} = 0 \quad (5)$$

Thus, by numerical analyzing eq. (5), relation between Displacement d and Length of non-adhesion area l can be calculated. When $l = L$ the area contact will become line contact. Then, by using eq. (3), (4) and flexure of non-adhesion area and geometric relation, relation between displacement and force can be calculated and the relation curve can be drawn as Fig3.

From Fig3, we can know if n becomes greater, the adhesion force becomes smaller, adhesion happens with smaller displacement, and when $n \geq 2$, line contact does not happen.

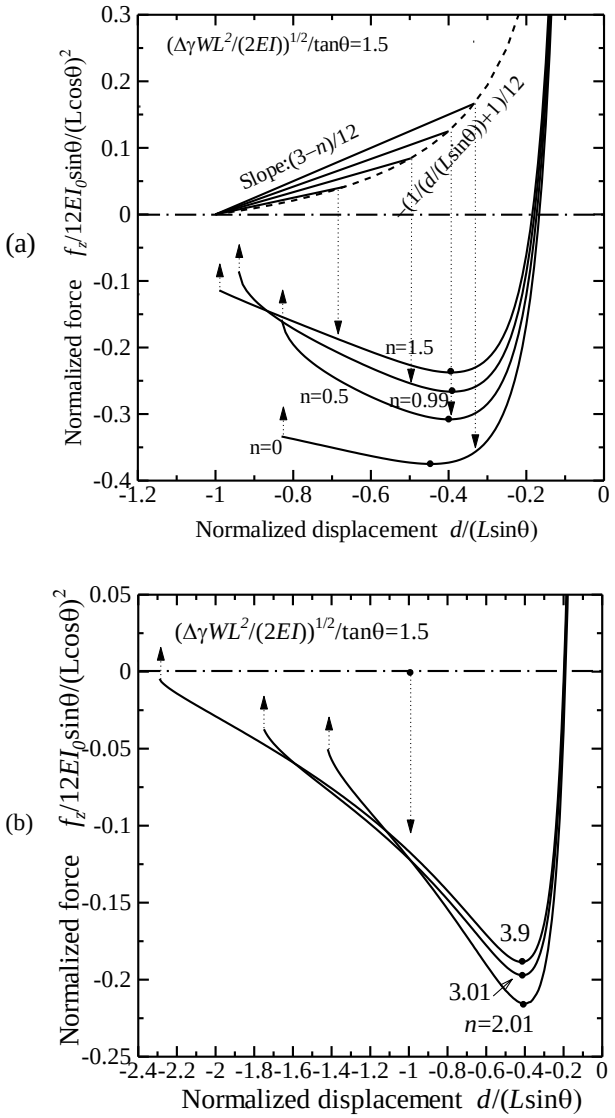

Fig.3.1:The relation between normalized force and normalized displacement when $(\Delta\gamma WL^2/(2EI))^{1/2}/\tan\theta=1.5$

Fig.4 Image of beam with s-shaped bending

4 Conclusion

In this study, we can know if n becomes greater, the adhesion between rigid body and elastic beam is likely to occur, but the adhesion force becomes smaller. The condition for which the linear beam theory can be applied in adhesion between elastic beam and rigid body theory is when the relation between displacement and Length of non-adhesion area of beam satisfies $-d/\sin\theta > l$.

References

[1]Adhesive force of a single gecko foot-hair, K. Autumn, et al., *Nature* Vol. 405, 681-685, 2000

[2]Journal of Adhesion Science and Technology, Y.sekiguchi,vol.26,No.23,December.2012,2615-2626

[3] 材料力学最新機械工学シリーズ１４　渥美光　鈴木幸三　三ヶ田賢次　森北出版

The Research of the Reinforcement Learning for Humanoid robot's walk control

Student Number : 07-04050 Name : Soichi Uchiyama Super visor : Yukihiko YAMASHITA

1 Introduction

Humanoid robots can easily fit into people's daily lives comparing to other types of robots. In recent years, the robots are used in many fields. To adapt to complex and diverse environments, a number of researchers study how to get a decision policy for the robot by its self-learning. The reinforcement learning is one of approaches, and many studies have been done. In the learning stage, the reinforcement learning is not necessary to teach the action in advance and the environment. Only the compensation for its action is necessary. Therefor learning can be done autonomously so that it is very effective.

In this paper, in order to make a humanoid robot adapt to its many degrees of freedom, I develop a simulator for a humanoid robot to be able to acquire the walking motion by using Q-learning with the dynamic structuring of exploration space based on genetic algorithm (QDSEGA). QDSEGA is an approach which combines evolutionary computing and reinforcement learning.

Fig.1 shows the outline of QDSEGA. First, the features of the robot are incorporated into the learning device so that the learning device can limit the search space and extract a subset of the search space. Next, the extracted search space is adapted to the reinforcement learning. Then, the subset is rebuilt with the knowledge gained from the reinforcement learning. By repeating this process, an effective subset and a policy for the reinforcement learning are obtained. Usefulness of simulation using QDSEGA is indicated by Ito [4].

I apply this algorithm to the walking behavior acquisition problem for a humanoid robot, and verify the usefulness of results of the simulation.

2 Learning Algorithm

Q-learning is a typical approach in the reinforcement learning. Q-learning has a theoretical framework regarding to optimazation. If the degree of freedom of action is small, Q-learning is very effective. However, for the problem of multi-degree-of-freedom, such as a humanoid robot, Q-learning is difficult to adapt because the state space and freedom of action are too large.

The classifying system is trained by genetic algorithm (GA). If we try to learn a policy in a large space, such as that of humanoid robots, it is difficult to acquire of an effective policy becase of the difficulties of maintaining consistency between the set of states indicated by the condition and the set of possible state transitions by the action.

QDSEGA approach can solve the problems. QDSEGA is designed for complicated systems with large action-state space like a robot with the redundant degrees of freedom.

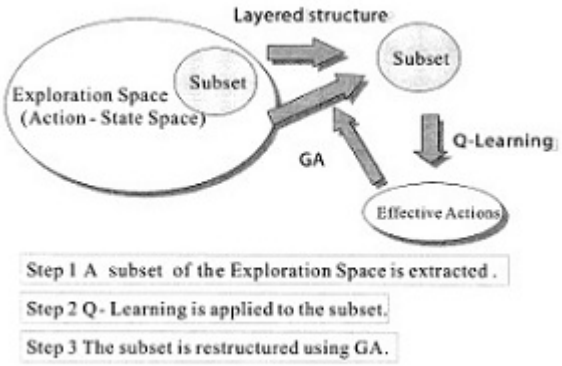

Fig. 1: Outline of QDSEGA

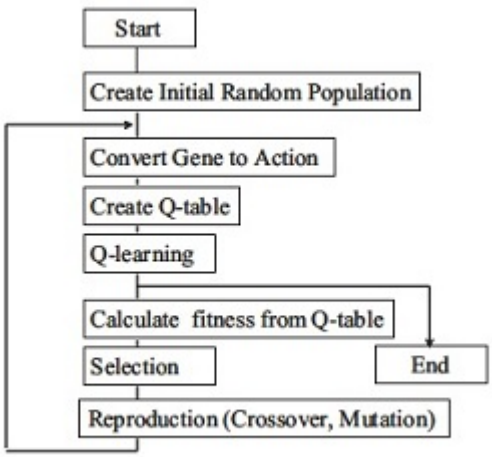

Fig. 2: Learning algorithm of QDSEGA

Fig.2 shows the flowchart of learning algorithm of QDSEGA. The learning algorithm is composed of a combination of action generating dynamics with GA and behavior acquiring dynamics with Q-learning. Actions are recorded as a gene and generated by GA. First, the initial population is generated randomly. Q-table is generated from the elements of the actions and the possible states. Q-learning is performed using this Q-table (Fig.3). If Q-learning is done sufficiently, Q-learning exits the learning stage and the fitness of each action evaluates based on the Q-value. According to the evaluation, parents are selected. Then, a new set of individuals is created from the parents by crossover and mutation. By repeating this process, a set of effective actions and a policy are obtained.

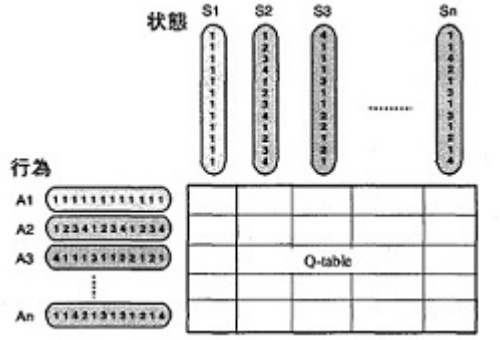

Fig. 3: Example of Q table

3 Simulator

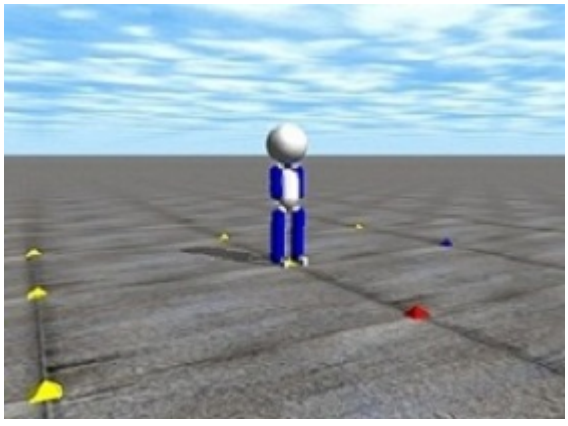

Fig. 4: Screen of Simulator

I apply this algorithm to the walking behavior acquisition problem for a humanoid robot, and verify the usefulness of results of the simulation. In addition, by introducing a multi-modal reward, the acquired behaver is optimized.

Action acquisition process using reinforcement learning algorithm usually needs very long running time. In addition, as this paper, for learning of waking behavior acquisition, wide range position measurement is required. Therefore, even if we produce a real robot, we need to use its kinetic simulator. In this paper, I built a simulator for a humanoid robot by using open-source 3D physics engine called Open Dynamics Engine(ODE). Usefulness of simulation using the ODE is indicated by Endo [5]. In this paper, I don't use an actual robot, and verify by using the simulator.

Fig.4 shows the screen of the simulator.

4 Conclusion

I made a walking simulator, and its possibility. For the future works it is necessary to set an appropriate action space against the explosion of the number of dimension, generate a Generate a value function with a multi-modal, and apply the results to real robots.

References

[1] Kazuyuki Ito, "The Robot Intelligence -the evolutionary computing and the reinforcement learning-," Ohmsha, Tokyo, 2007 (in Japanese)

[2] Kosei Demura, "Simple! Practice! The robotic simulation," Morikita publishing firm, Tokyo, 2007 (in Japanese)

[3] "Open Dynamics Engine"http://www.ode.org/

[4] Kazuyuki Ito, Fumitoshi Matsuno, "Control of Real Robot Using QDSEGA -Extension of Layered Structure and Application to Snake-like Robot" JRSJ Vol.21 No.5, 2003 (in Japanese)

[5] Gen Endo, Keisuke Arikawa, Shigeo Hirose, "Quantitative Evaluations of Open Dynamics Engine as a Research Tool -Comparison of Joint Torque and Power Using Quadruped Robot TITAN-VIII-," 28th RSJ's academic meeting, 2010 (in Japanese)

[6] Masatoshi Yamaguchi, Tadahiko Murata, "The Effectiveness of Neighboring Crossover for Controlling Multi-Legged Robot Using QDSEGA" 16th RSJ's intelligent system symposium, 2006 (in Japanese)

Application of TIV for multi-scale atmospheric flows

学籍番号：08B00019　氏名：アーリフ ムタズ　指導教官：神田 学

1　はじめに

TIV (Thermal image velocimetry) はサーモカメラで撮影された熱画像の時間的な変位を追跡することで，物体表面近傍の速度場を同定する手法である．本手法の適用例はこれまでに屋外大気環境下における建物鉛直壁面において精度検証が行われているのみであり，今後様々な場への応用が期待される[1].

本研究ではその手始めとして，（1）様々な空間スケールの流れの観測と，（2）複雑形状に沿った流れの計測についての応用を検討した．（1）に関して，本手法の測定範囲はカメラの撮影範囲とほぼ等価であるため，数 km に渡る広範な領域から，数 m 以下の領域への適用も原理的には可能であるが，その技術的側面について実観測に基づいた検討を行った。（2）の複雑形状への応用については主にその方法論について記述する．

2　測定手法

TIV はサーモカメラで撮影した一連の連続熱画像データから，表面近傍の風速場を定量的に推定する。測定原理は PIV(Particle image velocimetry)[2]とほぼ同じであるが，粒子画像の代わりに熱画像を利用するため，場の不均一性に起因した温度むらを，ハイパスフィルターを用いて除去する操作が必要である[3].

上記の解析を行う上で，3 つのパラメータを設定する必要がある．それは，画像相関を行う検査領域の大きさ S，ハイパスフィルターの平均化時間 T_{ave}，そして比較する 2 枚の画像の時間間隔 dt である．本研究では，これらのパラメータの撮影領域依存性（画像解像度依存性）について検討し，パラメータを決定する指標を作ることを試みる．

3　観測概要

本観測では，空間スケールの大きく違う領域を選んだ。その中から紹介するのは（1）人工芝の運動場（約 100 m 四方），（2）屋外に曝したスタイロフォーム平板（約 50 ㎝四方），（3）鋸山山麓（樹冠部，約 1 km 四方）、（4）スタイロフォーム円柱（約 30 ㎝四方），の 4 つであり，これに既往の研究で行われた（5）建物壁面観測結果を加えて比較を行う．（1），（2），（5）は平坦な場であるが，その空間スケールが大きく異なる．（3），（4）は平面ではなく立体面の流れの計測を実施する．

これらの領域の共通項として，撮影面が小さな熱慣性を持ち，大きな表面温度変動が期待できるためである．表 1 に各種観測概要について記す．

表 1：サーモカメラの撮影領域と時空間解像度

ケース	L [m]	ds [mm/pixel]	F [Hz]
山	～1000	～1000	50
人工芝	～100	～100	100
壁	20 x 3	30	30
円柱	0.3 x 0.5	1.8	100
平板	0.58 x 0.46	1.8	166

L: domain size, *ds*: resolution, *f*: sampling frequency

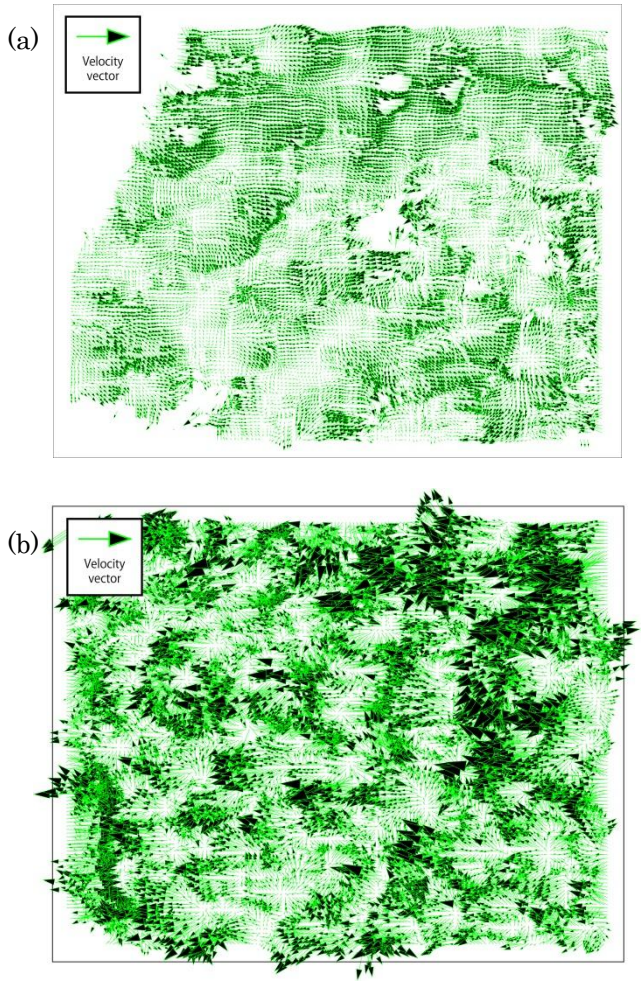

図 1： 移流速度ベクトル分布

(a) 人工芝グラウンド, (b)スタイロフォーム平板

4　スケール依存性

平面の 2 つのケースと壁面のケースについて，各種解析パラメータを比較する。図 1 はグラウンドとスタイロフォーム平板の観測結果であり、流れの様

子が風速ベクトルにより表現されている．適切なパラメータの選択は目視に基づいており，誤ベクトルの少なさや実際の風向との一致などを判断基準に行った．

次に各観測例における最適な解析パラメータについて見てみる（図 2）．主なパラメータとしては，画像相関を検定する領域の大きさS，時間フィルターの大きさT_{ave}，画像間の時間幅dtなどがある．まずSに関してはスケールに依らずピクセル数で決まっており，スケールにはあまり依存しない傾向が見られた．つまり画像相関という統計手法の制約で決まる．T_{ave}，dtについては明確なスケール依存性があり，それは流れ場の速度と画像の空間解像度によって主に決められるためである．

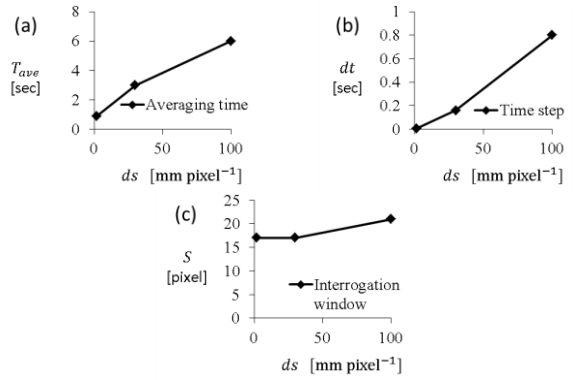

図 2: 画像解像度に対する(a)平均化時間 T_{ave}，(b)画像相関の時間間隔 dt，(c)検査領域サイズ S 依存性

5 複雑な地形への応用

次に複雑な物体表面周りの流れの計測について，適用可能性を検討した．図 3 は鋸山とスタイロフォーム円柱の観測結果である．解析パラメータは図 2 の結果を参考に，表 2 のように決定した．図 3 は時間フィルターを施した温度変動の画像であり、それぞれ鋸山（図 3a）とスタイロフォーム円柱（図 3b）の観測結果である。鋸山の場合は画像に移る前後の山の空間的な連続性が無いため、温度画像をパッチ状に切り分けて解析を行った。その結果流れに沿って温度分布が引き伸ばされている様子が見て取れる。

速度ベクトルを算出する際、平坦と異なり 2 次元で表示される速度ベクトルを 3 次元形状の面にそれぞれ投影することで、実際のベクトルが算出可能であると考えられるが、これについては今後の課題である。

表 2 ：TIV の各種解析パラメータ

ケース	S [pixel]	T_{ave} [sec]	dt [sec]
山	21	6	0.8
円柱	17	0.5	0.01

S: interrogation window size, T_{ave}: averaging time, dt: timespan between two images

6 結論

スケールが違う領域や、複雑な幾何形状を有する面に対して TIV を適用し、その適用可能性について検討した。今回テストした 1m 弱の平板及び、100m 程度のグラウンドでは本手法を適用することが可能であることを定性的に確認した。また空間スケールの異なる 3 つの観測の比較から、時間フィルターの大きさや、解析画像間隔が撮影画像の空間解像度に大きく依存することを示した。その一方で、画像相関を行う検査領域の大きさについてはほぼ一定値であることが分かった。この結果は他の実験を行う際の、パラメータの設定基準に応用することができると考える。複雑形状面への応用については、流れの可視化のみ示した。今後、テクスチャーマッピングによる物体表面への投影により、物体面に沿ったベクトルの計算などができるものと考えられる。

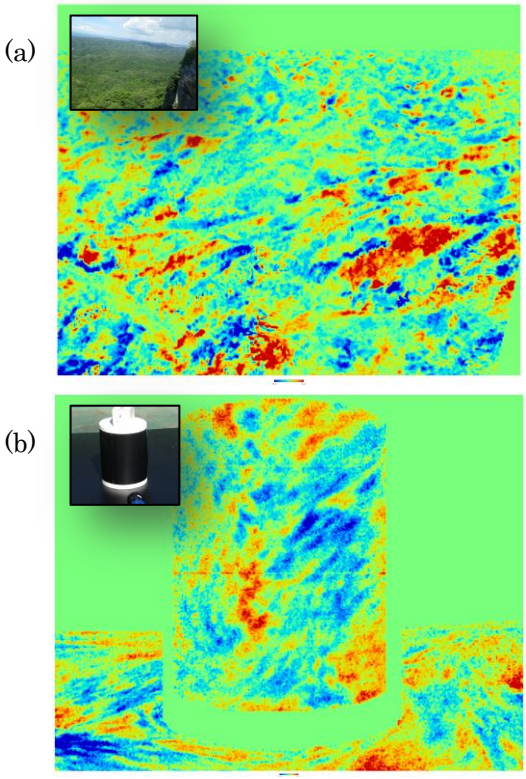

図 3 変動温度

(a)鋸山, (b)スタイロフォーム円柱

コンターは表面温度分布を表し、赤い方が高温である

参考文献

[1] 神田学,稲垣厚史,久米村秀明:“サーモカメラを用いた壁面近傍風速の計測手法開発”,ながれ, Vol.31, pp.491-493, 2012

[2] Adrian RJ (1991) Particle-imaging techniques for experimental fluid mechanics. Annu Rev Fluid Mech 23: 261-304

[3] Christen A, Meier F, Scherer D (2012) High-frequency fluctuations of surface temperatures in an urban environment. Theor Appl Climatol 108: 301-324

Prototype of boost converter for energy harvesting with automatic Maximum Power Point searching

Student number: 08B00597 Name: Ryushi ASAMI Supervisor : Kunio TAKAHASHI

1. Introduction

Energy harvesting, which means gathering unused tiny energy from environments such as lights, vibration, or heat, is mainly used as power source of low power devices. For example, it is used for driving wireless switch [1], and expected for further application such as driving wireless sensor networks.

An optimized storage method of storing tiny electric energy using boost converter, was proposed and studied by Tanaka [2], from which he could achieved storing efficiency of 90%. However, tiny electric energy is sensitive to fluctuation of environmental factors. Therefore, searching Maximum Power Point (MPP) of power source is an essential function needed for the forementioned boost converter.

The purpose of this study is to make a prototype of the boost converter to storage electric energy from solar cell to capacitor, taking into account the searching of MPP.

2. Theory

2.1 Power source's model

In this study, we use a solar cell as a power source with the I-V characteristic and P-V characteristic shown as Fig.1 [3]. The largest output point is called Maximum Power Point, its voltage and current is defined as V_{MP} and I_{MP} respectively. R_{MP} is defined as $\frac{V_{\mathrm{MP}}}{I_{\mathrm{MP}}}$.

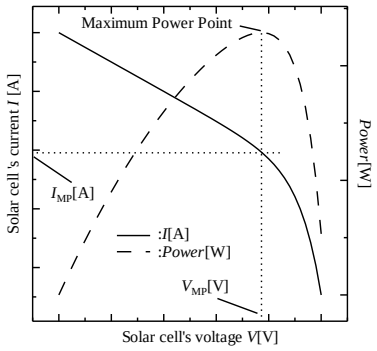

Fig.1: Theoretical characteristics of solar cell

2.2 Circuit model

Figure2 shows the boost converter circuit and its equivalent model. It is assumed that power source works nearby MPP, and V_{C} is constant during one switching period.

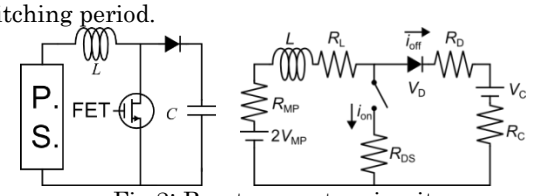

Fig.2: Boost converter circuit and equivalent circuit model

Boost converter works by switching FET on and off. The ratio of FET on-time in one switching period is defined as duty ratio.

2.3 Formula

Optimized duty ratio d_{gt} , maximizing efficiency, is defined as follows[2].

$$d_{\mathrm{gt}} = 1 + \frac{1}{\tilde{T}}\log\left(\frac{\left(\frac{1}{2}-\frac{1}{\tilde{g}_{\mathrm{CD}}}\right)\left(1-\exp(-\tilde{T})\right)}{+\sqrt{\left(\frac{1}{2}-\frac{1}{\tilde{g}_{\mathrm{CD}}}\right)^2\left(1-\exp(-\tilde{T})\right)^2+\exp(-\tilde{T})}}\right)$$

$$\tilde{g}_{\mathrm{CD}} = \frac{V_{\mathrm{C}}+V_{\mathrm{D}}}{V_{\mathrm{MP}}}$$

$$\tilde{T} = \frac{R}{L}T$$

$$R = R_{\mathrm{MP}}+R_{\mathrm{L}}+R_{\mathrm{C}} \approx R_{\mathrm{MP}}+R_{\mathrm{L}}+R_{\mathrm{DS}}$$

We have to know V_{MP}, R_{MP}, and capacitor voltage V_{C} in real time to apply optimized duty ratio.

3. Prototype and experiment

3.1 MPP searching method

We introduce the MPP searching circuit including power source as shown in Fig. 3.

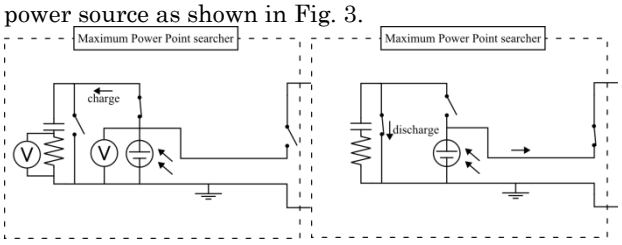

Fig.3: MPP searcher

At first, the capacitor has low voltage, the solar cell starts charging it from low voltage. The Voltage of capacitor increases, and the voltage of the solar cell increases consequently. We can observe a wide range of I-V characteristic of solar cell and decide where MPP is.

3.2 Circuit

We setup the circuit for experiment as shown in Fig.4.

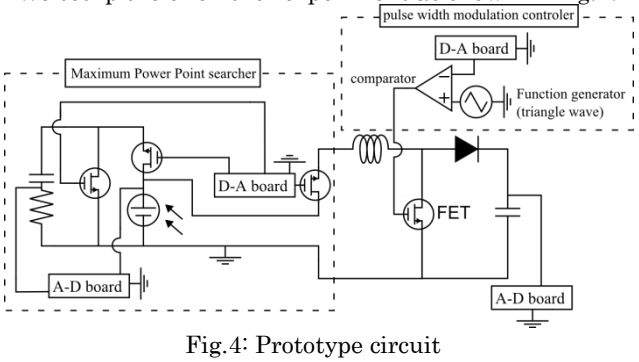

Fig.4: Prototype circuit

The specification of the circuit components are as follows;

Boost converter

Inductor	L: 0.47[mH] R_{L}: 0.21[Ω]
MOS-FET	R_{DS}: 78[mΩ]
Diode	V_{D}: 0.32[V] R_{D}:0.20[Ω]
Capacitor	C: 0.22[F] R_{C}: 6.0[mΩ]

MPP searcher

MOS-FET's D-S on resistance(x 3)	0.1[Ω]
Shunt resistance	1.00[Ω]
Capacitance	1000[μF]

A computer is used to search P-V characteristics shown as Fig.5, measure V_C, calculate d_{gt}, and output voltage to PWM circuit to control FET Switching.

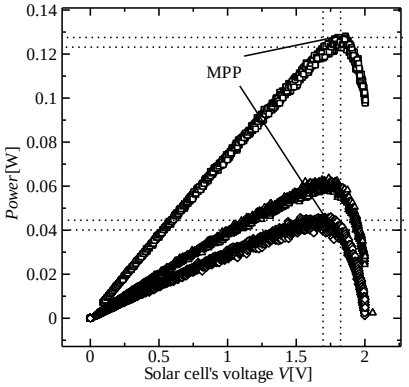

Fig.5: Measurement of P-V characteristics

Measuring V_C is done every 100ms. Measuring V_{MP} and R_{MP} is done every 5000ms. One searching MPP needs to separate the solar cell from boost converter less than 30ms. Measuring V_C, calculating d_{gt}, and outputting don't need to separate

3.3 Experiment

We adjusted the solar cell as V_{MP}=1.9[V], R_{MP} = 24[Ω] and charged capacitor from 2V to 6V by this circuit. After that, we gave to the computer fixed parameter V_{MP}=1.9[V], R_{MP} = 24[Ω], and charged capacitor again.

Next, we adjusted the solar cell as V_{MP}=1.7[V], R_{MP} = 32[Ω] and experiment for both parameters settings again.

3.4 Experimental results

Figure.6 and 7 show the experimental results

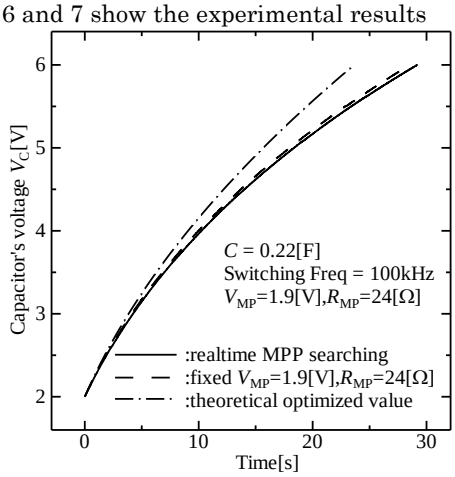

Fig.6: Experimental result

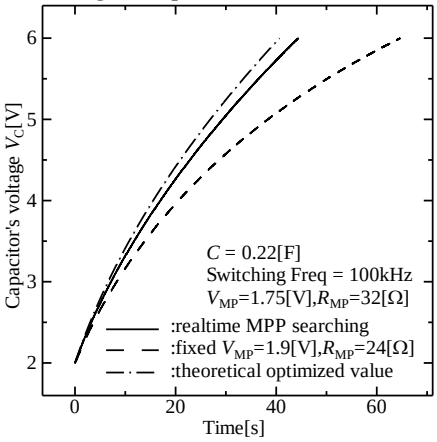

Fig.7: Experimental result

3.5 Discussion

From Fig6, charging efficiency of proposed method, searching MPP and in real time is almost equal to that of MPP parameters fixed. It can be said MPP searching is almost exactly.

From Fig7, efficiency of proposed method is 135% of that of MPP fixed. It can be said proposed method has advantage when MPP changed.

On the other hand, efficiency of proposed method is 80~90% of theoretical value. Figure.8 shows behavior of solar cell when charging. It shows that output voltage of solar cell doesn't follow the theory after FET's switching. It is not clear that switching noises effect efficiency, but if solar cell didn't work enough when switching noises occur, differences between theory and experiment are reasonable. To discuss this defect, we have to make the circuit not to be influenced from any external factor like electromagnetic waves.

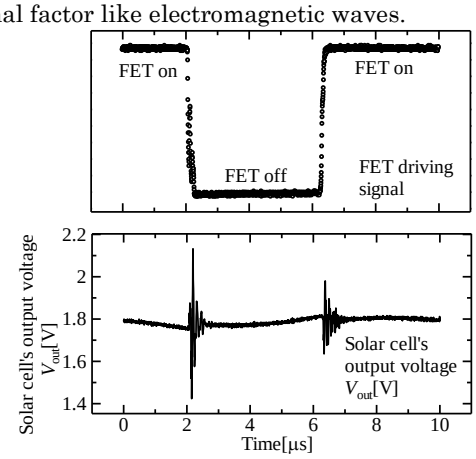

Fig.8: Switching noises

4. Conclusion

We proposed method of the boost converter to search MPP and measure V_C in real time. The proposed method can increase harvest when MPP varied. This MPP searching method is applicable other power sources like a thermoelectric element and also have room for improvement in deciding process of MPP.

To make more harvest, we need to identify what factor make this method less efficient. The switching noises are worth to investigate.

References

[1] EnOcean. http://www.enocean.com/home/

[2] Masanori Tanaka "Optimization of control parameters of a boost converter for energy harvesting" Journal of Physics: Conference Series 379 (2012)

[3] Kiyoshi Takahashi "太陽光発電"(1980)
ISBN： 9784627740303(in Japanese)

Financial Analysis of Vertical Integration and Privatization for Airports in Hokkaido

Students Number : 08-08759 Name : Ryuuhei Kudou Supervisor : Shinya Hanaoka

1 Introduction

Air transport is very important for Hokkaido because of distance between cities, and distance to urban area outside Hokkaido. But the estimation by Hokkaido prefecture government says many of airports in Hokkaido are operated at a loss and deficit in these airports are paid out of government's general account. To reduce the deficit covering by government's general account and to operate more flexibly, it is needs to introduce private capital and operating know-how by privatization.

On the other hands, there is no estimation of each airport's balance until recently, and Airside; facilities of airports is operated by public like The Government, prefectures, and cities, in contrast, Landside like airport buildings is operated by private capital with public, or only private. In abroad cases, the commercial revenues by Landside are made much account for airport operation. So it is need for vertical integration of Airside and Landside before privatization in Japanese airports.

This research aims to calculate financial balances of airports in Hokkaido after vertical integration, and to estimate profit or loss of airports after privatization.

2 Airports in Hokkaido

There are 14 airports in Hokkaido as shown in Figure 1. 4 airports are operated by the central government (●), 2 airports by SDF (Self Defense Force) (☆), 6 airports by Hokkaido prefecture (▲), and 2 airports by their cities government (○). In figure 1, Okushiri, Rishiri and Rebun airport are located in isolated island. Chitose airport has no private schedule air flight service, hence this research excludes this airport from analysis.

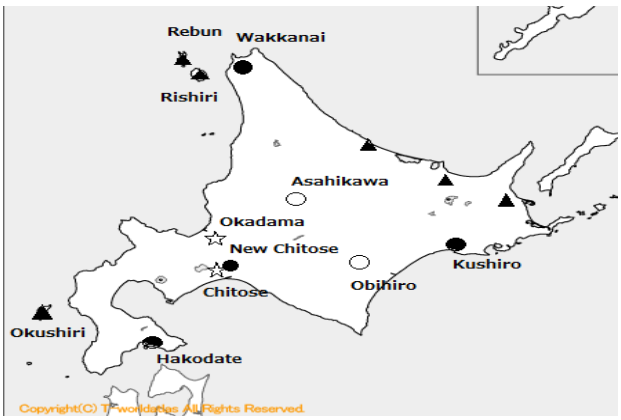

Figure 1, Airports in Hokkaido

3 Methodology and Results

3.1 Calculate items

This analysis is based on form of operating profit and loss; P/L, and deal with subsidies to containing nothing, only fuel tax of plane, or containing all subsidies. I calculated about after vertical integration (VI) and 2 types of privatization, Sale type, and Concession. Table 1 is operating P/L of VI, in Sale type, and in Concession.

Table 1, P/L in BI, Sale type, Concession

VI	Sale type	Concession
Airside income	Airside income	Airside income
Landside income	Landside income	Landside income
Labor cost(A)	Labor cost(A)	Labor cost(A)
Rent for lot and building(A)	Rent for lot and building(A)	
Subsidy for location	Fixed assets taxes	
Depreciation cost(A)	Depreciation cost(A)	
Other costs(A)	Other costs(A)	Other costs(A)
Labor cost(L)	Labor cost(L)	Labor cost(L)
Depreciation cost(L)	Depreciation cost(L)	
Other costs(L)	Other costs(L)	Other costs(L)
Operating profit and loss	Operating profit and loss	Operating profit and loss
P/L with fuel tax	P/L with fuel tax	P/L with fuel tax
P/L with all subsidies	P/L with all subsidies	P/L with all subsidies

There is no difference in P/L about airport operation of after VI and Sale type because the operator and owner of airport translate private to public at same time. But profit on sales will be paid by new owner to current owner, public. 'Subsidy for location' is like fixed assets tax on government properties. Subsidy for location will change to fixed assets tax, because owner changes public to private, but sum won't change.

In case of Concession, operator is private, but owner remain public as VI. Therefore, the expenses that the owner must pay will be paid by owner of airport but not operator. The expenses are 'rent for lot and building', 'subsidy for location', and 'depreciation cost' of Airside and Land.

3.2 Items of P/L

Airside income is assumption of landing fee and rent from lot and building. I use ordinary expenses of airport buildings for 'Landside income'. Because I cannot get data of depreciation cost (A) of Asahikawa and Obihiro, I use the data of airports whose histories of building runway are similar to these airports. Other cost (A) is assumption of building cost, cost of supplies cost for environmental measure, and so on. Because I cannot get labor cost (L), I use number of employee and officer. These number multiple by their salaries and add legal welfare expenses. I deal with part-time officer as 0.163 of full time officer according to the rate of salary in incorporated administrative agency.

Calculation formula is follow;

Labor cost (L) =((number of employee * employee's salary + (number of full-time officer + number of part-time officer*0.163) * officer's salary) * 1.139

Other cost (L) is cost of goods sold and selling and administration costs otherwise labor costs and depreciation costs. But it is difficult to get them, so I use ordinary cost of buildings minus interest expenses, labor cost, and depreciation cost. The rate of fuel tax is different as the operator, so I revise the rate as operator gets all of fuel tax in the airport. I can get other costs.

3.3 Results

Table2 shows the results of calculation based on Table1 about P/L in VI, Sale type privatization, and Concession with conditions of subsidies about 13 airports in Hokkaido.

Table 2, P/L in BI, SALE type, Concession

Opertor	The government				SDF	Hokkaido prefecture						City		
Airport	New Chitose	Wakkanai	Kushiro	Hakodate	Okadama	Memanbets	Nakashibets	Memanbetsu	Okushiri	Rishiri	Rebun	Asahikawa	Obihiro	million
Operating P/L	2,087	-897	-1,048	-817	-343	-449	-340	-347	-277	-281	-6	-343	-440	VI
P/L with fuel tax	4,595	-845	-813	-279	-343	-286	-308	-347	-277	-281	-6	584	543	
P/L with all subsidies	6,915	-796	-577	233	-341	-268	-299	-346	-267	-281	-6	856	928	
Operating P/L	2,087	-897	-1,048	-817	-343	-449	-340	-347	-277	-281	-6	-343	-440	SALE type
P/L with fuel tax	4,595	-845	-813	-279	-343	-286	-308	-347	-277	-281	-6	584	543	
P/L with all subsidies	6,915	-796	-577	233	-341	-268	-299	-346	-267	-281	-6	856	928	
Operating P/L	4,679	-388	-237	506	-169	-116	-201	-167	-83	-218	-5	289	-22	Concession
P/L with fuel tax	7,187	-336	-2	1,043	-169	47	-169	-167	-83	-218	-5	1,215	961	
P/L with all subsidies	9,507	-287	234	1,555	-167	65	-160	-166	-73	-218	-5	1,487	1,346	

According to this result, all airports except New Chitose are operated at a loss in case of VI if there is no subsidy. On the other hand, Concession which needs the lowest operating cost can reduce the airports that operating at a loss to 7 airports, and 3 among them is airports in isolated island. New chitose, Hakodate, Asahikawa, and Obihiro can privatize conditional on subsidies in SALE type. And Kushiro and Memanbetsu may be able to privatize in Concession with subsidies. However, it is needs to note that this table is only about airport's economic balances, and the government must pay owner's cost in case of Concession (Table3).

Table 3, Incomes and Expenses of public

	SALE type	Concession
Incomes	Profit on sales	Initial payment Concession fee
Expenses	(Subsidies)	Rent for lot and building Subsidy for location Depreciation cost (Subsidies)

4 Conclusion

This research analyzes P/L in after vertical integration and privatization with the use of past data of Airside and Landside. There are these future issues; 1) Estimate future items with the use of past data and analyze future privatization use these items. 2) Analyze about operating some airports as a group to privatize more non-profitable airports.

References

[1] Anne Graham: "managing airports", Butterworth - Heinemann, 2008.

[2] Res. Group for Air Transport Policy and Practices in Japan: "About the way of the future airport administration", 2009.

[3] H. Murakami, K. Kato, N. Takahashi, Y. Sakakibara: 'Economics of airport', Minerva syobou, 2008.

Geometrical Shape of Arch Formed by Collapse of Undercut Slope

Student Number: 08B20281 Name: Hidehira HIRAI Supervisor: Thirapong PIPATPONGSA

1. Introduction

A stable arch formed across a pit is beneficial to the design of an undercut slope in open-pit mining; therefore, prediction of the maximum stable undercut width under which the slope does not collapse is needed. The relation between a stable width and an inclined angle has been obtained experimentally to confirm the developed theoretical relations[1)]. The actual engineering application under this theory was immediately tested at the Mae Moh open-pit lignite mine in Thailand in December 2011. Fig.1 shows the stage of excavation as observed in October 2012 on the right side of the pit. At this targeted area, the stability of undercut slope is not only depended on arch action, but is also contributed by some reinforcement to the arch crown using array of shear pins. Because, design of shear pin requires reliable estimation of geometrical arch shape, this study reveals a fundamental research in an attempt to understand criteria of arch shape through a series of physical models using both 10 yen coins and moist silica sand no.6[1-3)].

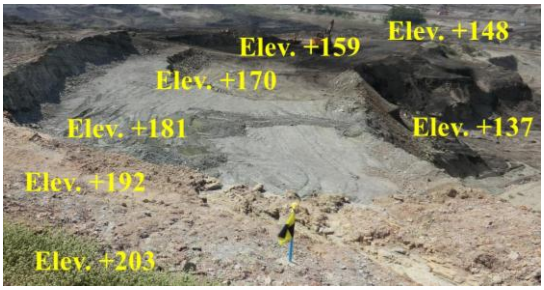

Fig. 1 Actual practice of undercut slope at the Mae Moh lignite mine in Thailand (as of October 2012)

2. Theoretical background

Granular media have ability to transfer load laterally to the stationary zone by readjusting the axes of principal stresses to form the load-bearing structure. This mechanism is known as arching effects[4)]. As shown in Fig.2, a convex upward scarp involves passive arch action where the connecting trajectories of major principal stress represent arch shape confined by the disconnecting paths of minor principal stress. Herein, the stress-free boundary represents zero minor principal stress. Components of contact force F are F_x in the x-axis and F_z in the z-axis. The vertical and horizontal supporting forces are F_v and F_h, respectively. The differential length of curve is δl.

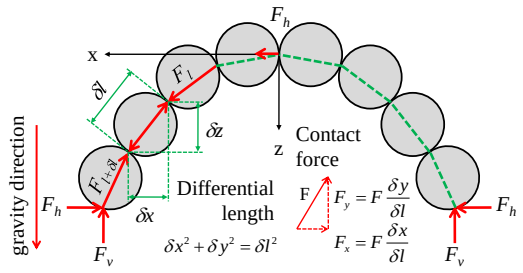

Fig. 2 Formation of stable arch where chain of contact force is connected to transfer load laterally

Contact chains in granular materials are outcome of structural adaptation against the applied loads. Such force patterns can be illustrated by the arrangement of granules with no shearing force acts on any of the contact points. According to Fig.2, equilibrium of forces along the x-axis and the z-axis can formulate differential equations of force along the axis of an arbitrary curvature. Four structures of arch providing the maximum stability are derived under the following symmetrical loading conditions which are also summarized to Table 1.

(1) Axial force exerting along the axis of arch with angle Ψ

$$z = |x| \tan \Psi \tag{1}$$

(2) Uniformly distributed load w along the gravity direction

$$z = \frac{1}{2}\frac{w}{F_h}x^2 \tag{2}$$

(3) Own weight of arch with constant unit weight γ

$$z = \frac{F_h}{\gamma}\left(\cosh\left(\frac{\gamma}{F_h}x\right) - 1\right) \tag{3}$$

(4) Uniformly distributed load ω acting perpendicular to arch

$$\left(z - \frac{F_h}{\omega}\right)^2 + x^2 = \left(\frac{F_h}{\omega}\right)^2 \tag{4}$$

Table 1 Basic geometries of arch under four particular symmetrical loading conditions

Form	Equilibrium along x-axis	Equilibrium along z-axis	Geometrical shape
(1)	$dF_x/dx = 0$	$\frac{dF_y}{dl} = 0$	Triangle
(2)		$\frac{dF_y}{dl} = w\frac{dx}{dl}$	Parabola
(3)		$\frac{dF_y}{dl} = \gamma$	Catenary
(4)	$\frac{dF_x}{dl} = -\omega\frac{dy}{dl}$	$\frac{dF_y}{dl} = \omega\frac{dx}{dl}$	Segment

Structural adaptation instigated by relative displacement and principal stress reorientation implies that both continuum and discrete structures can form stable stacks of arch. Formation of arch observed from free surface or scarp after removal or excavation of basal supports provides useful information about load transmission. Load breaking the arch is its own weight. If static stress adjacent to the scarp is higher than the unconfined compressive strength or buckling resistance of the materials, arch will eventually collapse.

3 Physical model tests

Typical arch shapes based on triangle, parabola, catenary and segment, as expressed in Eqs.(1)–(4), respectively, are employed for back analysis in order to approximate the unknown loading conditions. Two different laboratory tests of undercut slope made of closed-packing of 10 Yen coins placing on acrylic plate (Fig.3) and moist silica sand no.6 placing on acrylic sheet (Fig.4) are considered. Tables 2 and 3 reported the testing criteria of undercut slopes using 10 yen coins and moist silica sand[1,3)] (density 1395 kg/m^3 and water content 10%), respectively.

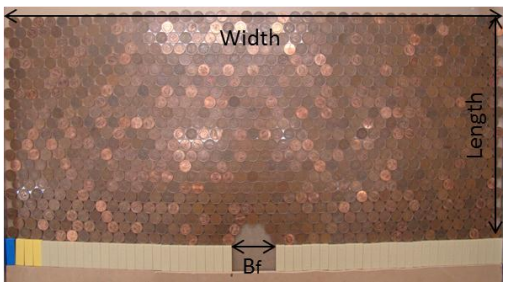

Fig. 3 Slope model made of 10 Yen coins showing a stable scarp after removal of supporting racks

Fig. 4 Slope model made of moist silica sand no.6 with stable undercut span after symmetrical removal of the basal support

4 Results

Photo images taken in normal direction to the stable scarps of stable slope made of 10 Yen coins were digitized. Mean square errors (MSE) in unit of cm^2 obtained from the least square method for interpolating each of typical four arch shapes to the actual shape of scarp were calculated and compared in Table 2 and 3. Numeric values shown in bracket represent the smallest MSE among the choices of typical arch shape. The segment curve obviously exhibits the best fitting geometry with the observed shapes of scarp in physical models.

Table 2 Testing results of undercut slope using 10 Yen coins

Test №	Inclined angle (˚)	Width (cm)	Length (cm)	Shapes of scarp
Case 1	40	40	50	Parabola
Case 2	50			Segment
Case 3	60			Segment
Case 4	40	70		Catenary
Case 5	50			Segment
Case 6	60			Segment
Case 7	70			Segment
Case 8	40	100		Segment
Case 9	50			Segment
Case 10	60			Segment
Case 11	70			Segment

Note: A coin has a diameter 2.35 cm with mass 4.5 gram

Table 3 Testing results of undercut slope using moist silica sand

Test №	Inclined angle	Width (cm)	Length (cm)	W_f (cm)	B_f (cm)	Mode
Test 1	60˚	70	40	55.0	50.3	1
Test 2	65˚			47.5	39.2	2
Test 3	70˚			40.0	32.4	2
Test 4	75˚			35.0	28.0	1
Test 5	80˚			37.5	24.8	2
Test 6	90˚			25.0	20.9	2

Note: Thickness for all series is 5 cm
W_f = actual failure width, B_f = predicted failure width
Mode 1 = scarp failure, Mode 2 = buckling

The results of image processing by particle image velocimetry (PIV) for the slope models made of moist silica sand no.6 are shown in Fig.5 as illustration. In this figure, the displacement vectors show the movement of the slope from the initial condition before excavation until the time just before failure of the slope and Fig.6 shows the contour of the shear strains which are corresponding to the displacement vectors. The lower region in Fig.6 showing the maximum shear strain indicates a possible location of failure. Fig.7 shows the photo of failure at the critical undercut width (W_f). Table 3 also summarized the predicted undercut width (B_f) and mode of failure. The value of W_f acceptably agreed with B_f using the buckling mode[1].

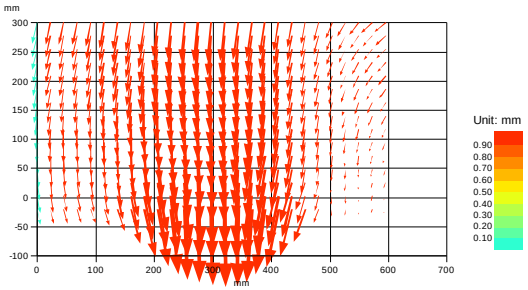

Fig. 5 Displacement vectors plotted from PIV results of Test 5

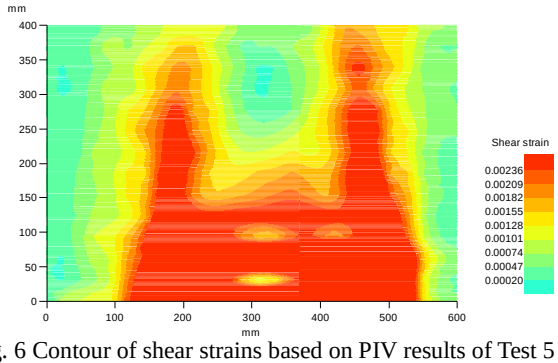

Fig. 6 Contour of shear strains based on PIV results of Test 5

Fig. 7 Collapse of undercut slope in a buckling mode of Test 5

5. Conclusion

Back analysis of loading conditions of undercut slope models using 10 Yen coins consistently confirms that the geometrical shape of arch can be estimated to a segment. Moreover, the segmental arch indicates that the assumption of uniformly distributed load acting along the arch used in the undercut model of moist silica sand is acceptable. The result of this study is benefit to a design of reinforcement to undercut slope by giving the reliable shape of failure zone using the segmental arch.

References

1) M.H. Khosravi: Arching effect in geomaterials with applications to retaining walls and undercut slopes, Department of International Development Engineering, Tokyo Institute of Technology, PhD Dissertation, 2012.
2) M.H. Khosravi, T. Pipatpongsa, A. Takahashi and J. Takemura: Arch action over an excavated pit in a stable scarp investigated by physical model tests, Soils and Foundations, 51(4), pp.723-735, 2011.
3) M.H. Khosravi, L. Tang, T. Pipatpongsa, T. Takemura and P. Doncommul: Performance of counterweight balance on stability of undercut slope evaluated by physical modeling, International Journal of Geotechnical Engineering, 6(2), pp.193-205, 2012.
4) K. Terzaghi: Stress distribution in dry and saturated sand above a yielding trap-door, The First International Conference on Soil Mechanics and Foundation Engineering, Cambridge, pp.307-311, 1936.

Numerical Analysis of Natural Convetion in an Arch Vessel by a Spectral Finite Difference Scheme

Student Number : 08-23457 Name : Keita Mitani Supervisor : Yoshihiro MOCHIMARU

1. Introduction

Computional fluid dynamics is adapted in many fields, e.g. engeneering, medical engeneering and mechanical design. A spectal finite difference scheme is a method in computional fluid dynamics. It has higher acuracy and higher efficiency than others. In this study, a heat and fluid flow field in an arch vessel placed horizontally is analyzed numerically, using a spectral finite difference scheme.

2. Analysis

Fluid enclosed is assumed to be incompressible and Newtonian. The wall of lower part is heated at a uniform temperature, while the other is kept at a lower constant temperature. No slip flow on the wall is assumed.

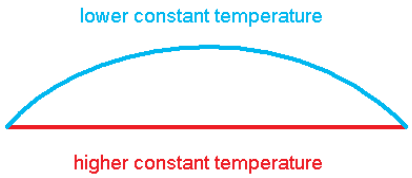

Fig.1 Model in analysis

3. Basic Equations

Equation of motion :

$$\rho\frac{D\boldsymbol{V}}{Dt} = -\nabla p + \mu\nabla^2\boldsymbol{V} + \rho\boldsymbol{g} \tag{1}$$

Equation of continuity (under Boussinesq approximation) :

$$\nabla\cdot\boldsymbol{V} = 0 \tag{2}$$

Energy Equation (with neglecting dissipation):

$$\rho c_p\frac{DT}{Dt} = \kappa\nabla^2 T, \tag{3}$$

where $\boldsymbol{V}$: velosity, t : time, ρ : density of fluid, p : pressure, μ : viscosity, T : temperature, κ : thermal conductivity, c_p : specific heat at constant pressure.

Conformal mapping from physical region $(x, y), (z \equiv x + i\,y)$ to the analytical region $(\alpha, \beta)(-\infty \leq \alpha \leq 0, |\beta| \leq \pi), (w \equiv e^{\alpha + i\,\beta})$ is given by:

$$w = \frac{1 + i\,f}{1 - i\,f}, \tag{4}$$

where f is an analytic function defined by

$$f \equiv \exp\left(a\ln\frac{z+1}{z-1} + b\,i\right) \tag{5}$$

$$a = \frac{\pi}{\pi - \theta}, b = -\frac{\pi\theta}{\pi - \theta} \tag{6}$$

Then, the upside discribes an arc, and the downside a straight line. θ : angle of circumference from the downside to the upside.

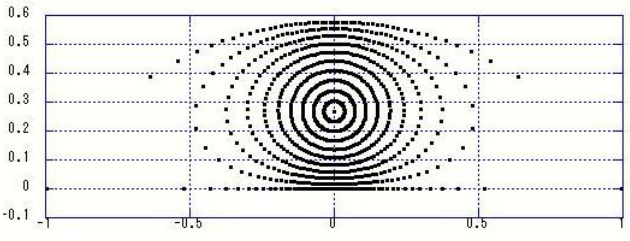

Fig.2 Grid points of physical region

Then Eqs.(1) and (2) lead to the vortisity transport equation in dimensionless form with a change of variables ($r \equiv e^{\alpha}, 0 \leq r \leq 1$):

$$J\frac{\partial \zeta}{\partial t} + r\frac{\partial(\zeta,\psi)}{\partial(r,\beta)} = \frac{1}{\sqrt{Gr}}\left(r^2\frac{\partial^2}{\partial r^2} + r\frac{\partial}{\partial r} + \frac{\partial^2}{\partial \beta^2}\right)\zeta + r\frac{\partial(T,y)}{\partial(r,\beta)} \tag{7}$$

Relation between vorticity and a stream function:

$$J\zeta = -\left(r^2\frac{\partial^2}{\partial r^2} + r\frac{\partial}{\partial r} + \frac{\partial^2}{\partial \beta^2}\right)\psi \tag{8}$$

Enegy Equation:

$$J\frac{\partial T}{\partial t} + r\frac{\partial(T,\psi)}{\partial(r,\beta)} = \frac{1}{Pr\sqrt{Gr}}\left(r^2\frac{\partial^2}{\partial r^2} + r\frac{\partial}{\partial r} + \frac{\partial^2}{\partial \beta^2}\right)T, \tag{9}$$

where ζ : vorticity, ψ : stream function, Gr : Grashoff number, Pr : Prandtl number, $J \equiv \frac{\partial(x,y)}{\partial(\alpha,\beta)}$.

The following Fourier decomposition is used:

$$\begin{aligned}
\zeta(r,\beta,t) &= \sum_{k=0}^{\infty}\zeta_{ck}(r,t)\cos k\beta \\
&\quad + \sum_{k=1}^{\infty}\zeta_{sk}(r,t)\sin k\beta \qquad (10)\\
\psi(r,\beta,t) &= \sum_{k=0}^{\infty}\psi_{ck}(r,t)\cos k\beta \\
&\quad + \sum_{k=1}^{\infty}\psi_{sk}(r,t)\sin k\beta \qquad (11)\\
T(r,\beta,t) &= \sum_{k=0}^{\infty}T_{ck}(r,t)\cos k\beta \\
&\quad + \sum_{k=1}^{\infty}T_{sk}(r,t)\sin k\beta \qquad (12)\\
J(r,\beta) &= \sum_{k=0}^{\infty}J_{ck}(r)\cos k\beta \\
&\quad + \sum_{k=1}^{\infty}J_{sk}(r)\sin k\beta \qquad (13)\\
y(r,\beta) &= \sum_{k=0}^{\infty}Y_{ck}(r)\cos k\beta \\
&\quad + \sum_{k=1}^{\infty}Y_{sk}(r)\sin k\beta \qquad (14)
\end{aligned}$$

Boundary conditions (on $r = 1$):

$$\begin{aligned}
\psi &= 0 \qquad (15)\\
J\zeta &= -\frac{2}{(1-r_{n-1})^2}\psi(r_{n-1}) \qquad (16)\\
T &= 0\,;\, -\pi \leq \beta < 0 \qquad (17)\\
T &= 1\,;\, 0 \leq \beta < \pi, \qquad (18)
\end{aligned}$$

where r_{n-1} is one step before the boundary (r_n) in finite difference approximation.

4. Numerical Results

Calculation was made for the case $Gr = 1, Pr = 0.7$.

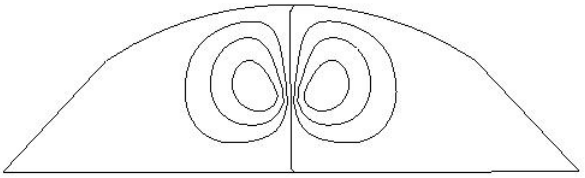

Fig.3 Steady-state streamlines at $Gr = 1(\Delta\psi = 0.0001)$

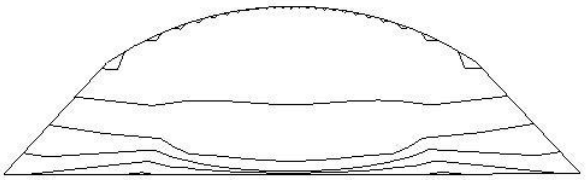

Fig.4 Steady-state isotherms at $Gr = 1(\Delta T = 0.2)$

5. Conclusion

In this study, a heat and fluid flow field in an arch vessel was analyzed numerically, using a spectral finite difference scheme. This result is symmetrical.

References

Y. MOCHIMARU, 'Effectiveness of a Spectal Finite Difference Scheme', *Computional Fluid Dynamics Review 1998*, Vol.1, 379-394, (1998).

ドップラーライダーで観測された流れ場の分類と特性の把握

学籍番号：09-00985　　氏名：有場次郎　　指導教官：神田学

1. はじめに

大気境界層とは地表面の影響（摩擦，放射など）を強く受ける大気層のことを指す．大気境界層では乱流の働きが活発であり，大気や物質の輸送が盛んである。一方で我々は基本的にこの層内で生活しており，大気境界層は都市における汚染物質拡散や局地的豪雨のメカニズムと密接な関係を有している．したがってこれらの問題を解決するためには，大気境界層内の乱流の挙動を知る必要がある．

大気境界層の流れ場を観測する測器の 1 つとしてドップラーライダーがある．ドップラーライダーとは，大気中のエアロゾルに向けてレーザー光を発射して，その反射光を受信して風速を計測するリモートセンシング装置である．ドップラーライダーの観測により都市上空には，水平ロール渦やプリューム構造といった組織的な乱流構造が存在していることが示された[1]．このような乱流構造の発生条件を解明するために本研究では，ドップラーライダーで観測された流れ場を 6 グループに目視分類し，3 つの大気指標と比較することで乱流構造の特性を探った．

2. 流れ場の目視分類法

解析の対象は，2012 年 10 月 3 日から 10 月 13 日の間にドップラーライダーの水平スキャンによって観測された計 2,447 枚の画像である．ドップラーライダー画像には視線方向風速分布と信号対雑音比(SNR)分布の 2 種類がある．本研究では流れ場を“Streak”，“No streak”，“Mixed”，“Fish net”，“Front”，“The others”の 6 グループに目視分類した．以下に各グループの分類基準を，図 1 に各グループの代表的な視線方向風速および SNR の分布を示す．

（a） Streak；視線方向風速の正負の境界が直線状で風向が一定である．風向に沿ったストリークが目視できる．

（b） No streak；(a) と同様に視線方向風速の正負の境界が直線状で風向が一定．ストリークは目立たない．

（c） Mixed （Mixed streak and fish net）；視線方向風速の正負の境界が乱れているが風向は大体一定である．ストリークは不明瞭である．

（d） Fish net；視線方向風速が正の領域と負の領域が入り混じっている．風向も定まらない．

（e） Front；SNR の分布図に明瞭な境界線が確認できる．

（f） The others；上記グループのいずれにも属さない．

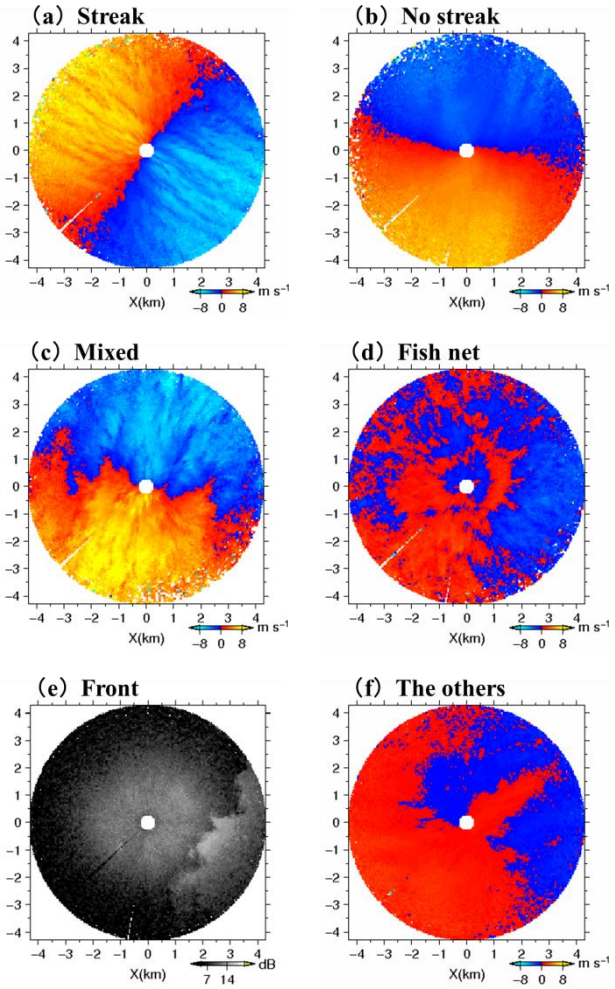

図 1:　目視分類された 6 グループの代表的な視線方向風速および SNR の分布図
（e）Front は SNR 分布，それ以外は視線方向風速分布である．視線方向風速は中心から遠ざかる向きが正で，中心に向かう向きが負である．

3. 目視分類と大気指標との関係

本研究において目視分類と比較を行ったのは水平風速，大気安定度z / L，境界層高度の 3 つである．水平風速とは，流れ場の水平方向の平均的な風速である．本研究では水平スキャンの視線方向風速分布のデータに，VAD 法[2]という手法を適用して算出した．

大気安定度z / Lとはモニンオブコフ相似則[3]における説明変数であり，この値の絶対値が大きいほど浮力の影響が，絶対値が小さいほど摩擦による影響が卓越している．またこの値が正だと大気は安定であり，負だと大気は不安定である．z / Lはドップラーライダーと同期観測した超音波風速計のデータから算出した．

境界層高度とは大気境界層の最上部，すなわち地表面の影響が及ぶ最高高度のことである．本研究では，ドップラーライダーを鉛直断面内でスキャンさせて得た，SNR の鉛直プロファイルから境界層高度を算出している．なおここでは触れないが，境界層高度を算出する際には，従来の方法に独自の改良を加えて行った．

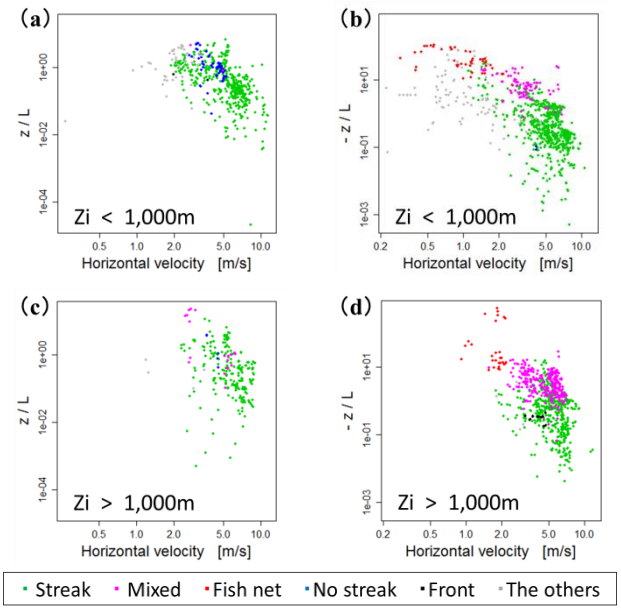

図 2:　目視分類と 3 つの大気指標との関係
z / Lの符号と境界層高度z_iによって次の 4 ケースに分けた．(a) 安定時でz_iが小さい，(b) 不安定時でz_iが小さい，(c) 安定時でz_iが大きい，(d) 不安定時でz_iが大きい．いずれの散布図も横軸が水平風速，縦軸がz / Lの絶対値で，両軸ともに対数表記である．

目視分類と 3 つの大気指標との関係を散布図で示す（図 2）．安定時（a）（c）において，水平風速が大きいときは Streak が，z / Lの絶対値が大きいときは No streak が発生する傾向があった．また不安定時（b）（d）において，水平風速が大きいときは安定時と同様 Streak が，z / Lの絶対値が大きいときは Fish net が発生する傾向があった．また Streak と Fish net のグループの中間に Mixed が分布した．

次に境界層高度の大きさに着目する．境界層高度の大きさによって明確に違ったふるまいを見せたのは No streak および The others のグループである．両者は境界層高度が 1,000m 以下のときには多く発生したが，境界層高度が 1,000m 以上になると事例数は極端に減った．一方 Streak，Mixed，Fish net のグループは，境界層高度が変化しても事例数に大きな変化はなかった．

4. おわりに

目視分類と水平風速，z / Lの比較より以下のことが分かった．Streak は風速が大きく摩擦の影響が強いときに，Fish net は大気が不安定なときに，No streak は大気が安定なときに，Mixed は摩擦と浮力の影響が均衡しているときにそれぞれ発生しやすい．また No streak および The others の境界層高度が低かったことから，The others に分類された流れ場にも一般的性質があり，そして No streak もその性質を共有していることが示唆された．

参考文献

[1] 藤吉康志，山下和也，藤原忠誠，2005：3 次元走査型コヒーレントドップラーライダーによる大気境界層の流れの可視化，天気，52, p.665-666.

[2] Browing, K. A., Wexler, R., 1968: The Determination of Kinematic Properties of a Wind Field Using Doppler Radar, *Journal of Applied meteorology and climatology*, 7, p.105-108.

[3] Monin, A.S., Obkhov, A.M., 1954: Basic laws of turbulent mixing in the ground layer of the atmosphere, *Tr. Akad. Nauk SSSR Geophiz. Inst.*,24, p.163-187.

CoO_x-CeO_2 mixed oxide catalysts for N_2O decomposition

Student Number: 09_04003 Name: Huiting WANG Supervisor: Hirofumi HINODE, Chris SALIM

1. Introduction

Nitrous oxide (N_2O) is one of the main greenhouse gases with an average life time of about 150 years in the atmosphere, and a net greenhouse effect of about 310 times and 21 times of the Global Warming Potential(GWP) of CO_2 and CH_4, respectively[1]. Moreover, N_2O is also identified as a contributor to the destruction of ozone layer in the stratosphere. The abatement of N_2O emissions from industrial plants(adipic acid production, combustion process, etc.) is probably the most feasible by implementing catalytic processes[2]. Catalysts which contain cobalt oxide, are the subject of studies as potential N_2O decomposition catalyst[3]. Combination of CeO_2 with other metal oxides often affects the mobility of oxygen on their surfaces, thus in some cases, modifies the elements's redox ability and catalytic performance[4].

In our laboratory, Co/TiO_2 catalysts using impregnation method and TiO_2-CeO_2 catalysts using manual mixing method for N_2O decomposition has been studied[5-6]. The addition of CeO_2 improved the catalytic activity of TiO_2. Considering both of the researches, in this work, the decomposition of N_2O over CoO_x-CeO_2 mixed oxide catalysts was investigated.

2. Experimental

2.1 Catalyst preparation

CoO_x-CeO_2 mixed oxide catalysts were prepared by manual mixing method. The precursor of cobalt oxide is $Co(CH_3COO)_2 \cdot 4H_2O$ (Kanto Chemical Co., Inc.). And two types of CeO_2 (JRC-CEO-1, Santoku Co. and JRC-CEO-2, Daiichi Kigenso Kagaku Kogyo Co., Ltd.) were used.

CoO_x was prepared by calcining cobalt precursor at 400℃ for 5 hours under air flow. CoO_x and CeO_2 were mixed manually in a mortar using small amount of ethanol for better mixing. The mixture was then calcined at a certain temperature between 400-800℃ for another 5 hours under air flow.

In order to reduce the pressure drop, the catalysts were pelletized, crushed and sieved into 0.71 mm to 1.00 mm particles prior to activity test.

The following nomenclatures for the catalyst samples are used: CoO_x-CeO_2 –X (Y:Z) where X represents the type of CeO_2(1 for JRC-CEO-1, 2 for JRC-CEO-2), and (Y:Z) means the weight ratio of CoO_x:CeO_2. For example, CoO_x-CeO_2 ② (1:2) means CoO_x and JRC –CEO-2 were mixed in the weight ratio of 1:2.

2.2 Catalytic activity experiment

The catalytic activity test was carried out in a fixed-bed flow reactor under atmospheric pressure. The reactant gas containing 1000 ppm N_2O, O_2(0% or 10%) and He(balance gas) was fed to the reactor at a flow rate which corresponded to a space velocity of 16000h^{-1}.

Gas chromatography (GC323w; GL Science Co., with Porapak N, Porapak Q and Molecular Sieve 13X column) was used to analyze N_2O.

2.3 Catalyst characterization

Characterizations of the catalysts were performed using TG analyzer (TG8120), XRD (MultiFlex), BET(Autosorb1) and SEM (JSM-5310LV) -EDS (JED-2140).

3. Result and discussion

Figure 1 shows the N_2O conversion by CoO_x-CeO_2 ① (1:1) calcined at different temperatures for the decomposition of N_2O without O_2. For all catalysts, the N2O conversion were almost the same. The CoO_x-$CeO_2$①(1:1) calcined at 500℃ and 600℃ showed a slightly better catalytic activity than others. N_2O began to decompose at temperature about 300-400℃, and achieved 100% of N_2O decomposition at about 650-700℃.

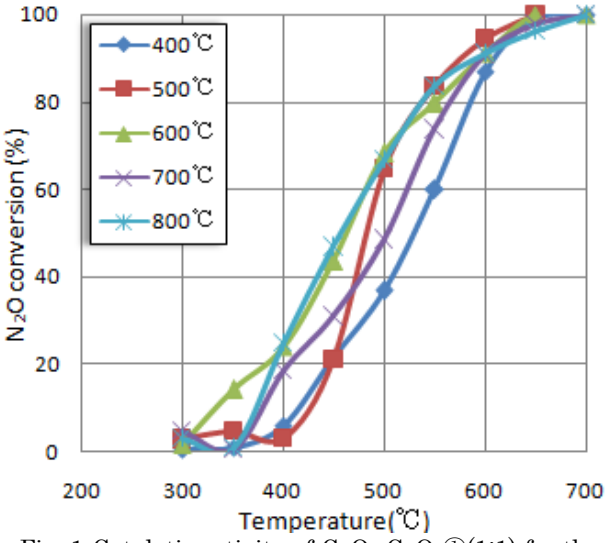

Fig. 1 Catalytic activity of CoO_x-$CeO_2$①(1:1) for the decomposition of N_2O without O_2.

Figure 2 shows the N_2O conversion by CoO_x-$CeO_2$②(1:1) for the decomposition of N_2O in the condition without O_2. For all catalysts, the N_2O conversion were almost the same. The CoO_x-$CeO_2$②(1:1) calcined at 400℃ and 500℃ showed a slightly better catalytic activity than CoO_x-CeO_2 ② (1:1) calcined at others. N_2O

began to decompose at temperature about 350-400 ℃, and achieved 100% of N_2O decomposition at about 600-650 ℃. CoO_x-$CeO_2$①(1:1) and CoO_x-$CeO_2$②(1:1) did not show obvious changes when calcined at different temperatures, and catalysts containing JRC-CEO-2 showed better catalytic activities than catalysts containing JRC-CEO-1.

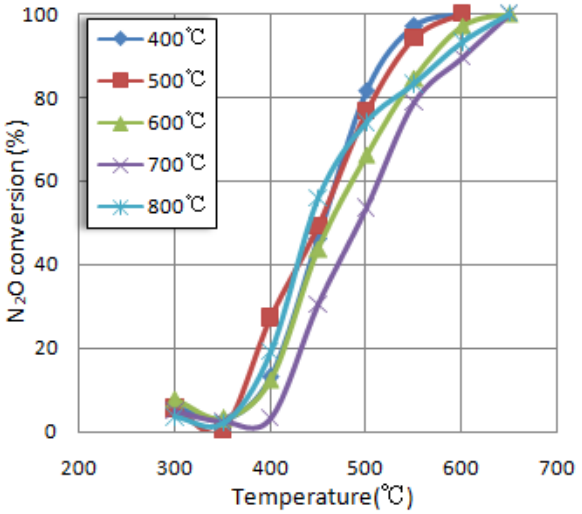

Fig. 2 Catalytic activity of CoO_x-$CeO_2$②(1:1) for the decomposition of N_2O without O_2.

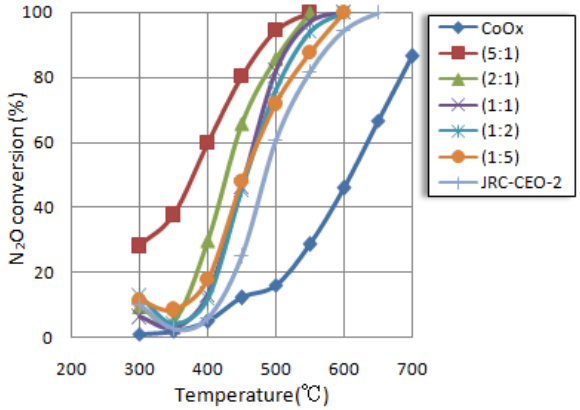

Fig.3 Catalytic activity of CoO_x-$CeO_2$② in various weight ratios calcined at 400℃without O_2

Figure 3 shows the N_2O conversion by CoO_x-$CeO_2$② in different weight ratios of oxides of Co and Ce and calcined at 400℃. CoO_x-CeO_2 ② (5:1) showed better catalytic activity than other catalysts with 100% of N_2O decomposition at 550℃. Mixed oxides showed higher catalytic activities than each bare JRC-CEO-2 and CoO_x. The higher CoO_x content, the higher the catalytic activity is. As the cobalt content increases, the beneficial effect of the cobalt oxide-ceria interface on the activity of the catalyst decreases. At the same time, the share of the activity of cobalt oxide in the overall activity increases[7].

N_2O decomposition shifted to higher temperature in the presence of oxygen showed in Figure 4. The reason for that could be considered that O_2 competed with N_2O in the processes of adsorption on active site[8].

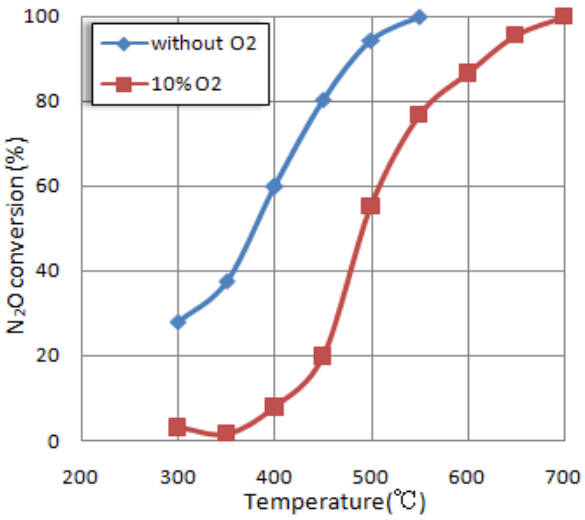

Fig.4 Effect of Oxygen on the catalytic activity of CoO_x-$CeO_2$②(5:1) for the decomposition of N_2O

4. Conclusions

The CoO_x-$CeO_2$①(1:1) calcined at 500℃ and 600 ℃ showed a slightly better catalytic activity than others. The CoO_x-$CeO_2$②(1:1) calcined at 400℃ and 500℃ showed a slightly better catalytic activity than CoO_x-$CeO_2$②(1:1) calcined at others.

Catalysts containing JRC-CEO-2 showed better catalytic activities than catalysts containing JRC-CEO-1.

CoO_x-$CeO_2$②(5:1) without O_2 showed the best catalytic activity with the N_2O decomposition achieving 100% at around 550℃.

N_2O decomposition shifted to higher temperature in the presence of oxygen.

References

[1] S. Kannan, Appl. Clay Sci. 13 (1998) 347.
[2] P. Esteves, Y. Wu, C. Dujardin, M.K. Dongare, P. Granger, Catal. Today 176 (2011) 453.
[3] C. Ohnishi, K. Asano, S. Iwamoto, K. Chikama, M.Inoue, Catal.Today 120(2007)145.
[4] S. Imamura, M. Shono, N. Okamoto, R.Hamada, S. Ishida, Appl. Catal. A 142(1996)279
[5] P. Gao, Master thesis, Tokyo Institute of Technoligy(2011)
[6] Y. Fukuchi, Bachelor thesis, Tokyo Institute of Technology(2012)
[7] E. Iwanek, K. Krawczyk, J. Petryk, J.W. Sobczak, Z. Kaszkur, Appl. Catal.B 106(2011)416
[8] S. Suarez, M. Yates, A.L. Petre, J.A. Martin, P. Avila and J. Blanco, Appl. Catal.B 64(2006)302

Synthesis of Zeolites from Lake Sludge as Ammonium Adsorbent Materials

Student number: 09_04055 Name: Wang Wenjing Supervisor: Hirofumi HINODE, Chris SALIM

1. Introduction

Lakes are important sources of fresh water, however contaminants and nutrient salts are easily accumulated because of the closed water systems and human activities around the lakes.

One of the most effective methods used to rehabilitate lakes is lake dredging. But the usual disposal method of dredged lake sludge is by landfill or incineration. For resource protection, the method of recycling should be considered. According to previous study, lake sludge which contains silica and alumina can be used as raw material to synthesize zeolites by hydrothermal treatment [1]. Zeolites are considered as good cation exchange materials, and they are used for ammonium ion removal in recent years[2].

In this study, zeolites from lake sludge were prepared using hydrothermal synthesis method in alkali solution. Characterization and NH_4^+-adsorption studies were conducted to determine which among the zeolites prepared has the best cation-exchange capacity.

2. Experimental

In this study, the sludge from Kasumigaura lake in Yibaraki was used. The sludge was dried, crushed and sieved (–150μm), and then dried again at about 100℃ for 24 hours. Si/Al ratio was adjusted from 1.9 to 3.0 by addition of Na_2SiO_3 solution. For zeolite synthesis, lake sludge (1.6g) was treated in different alkali solution (1, 1.5, 2, 2.5, 3M 8ml) and put inside shaker for 24 hours in a teflon reaction vessel. Afterwards, the teflon vessel was put into a metal container, and then placed in the oven at 100℃, 120℃, 150℃. Afterwards, the zeolites were washed with deionized water and dried at room temperature.

After synthesis, the characterization study was done by XRD, SEM, and ICP. Finally, the cation exchange capacity was measured by NH_4^+-adsorption using back titration method.

3. Results and discussion

3.1 XRD analysis

The XRD analysis of the zeolites synthesized at different alkali concentrations, temperatures, and Si/Al ratios are shown in Figures1, 2 and 3.

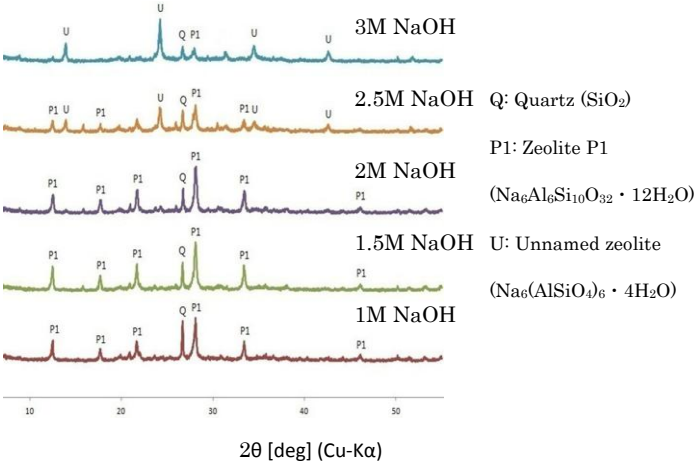

Fig.1 X-ray diffraction patterns of zeolites treated with different alkali concentrations (Si/Al=1.9, 120℃)

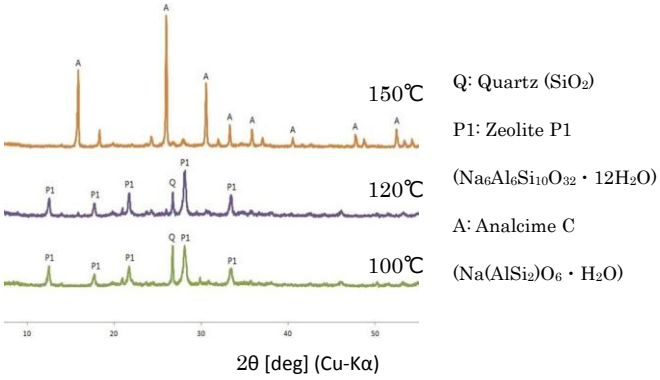

Fig.2 X-ray diffraction patterns of zeolites synthesized at different temperatures (Si/Al=1.9, 2M NaOH)

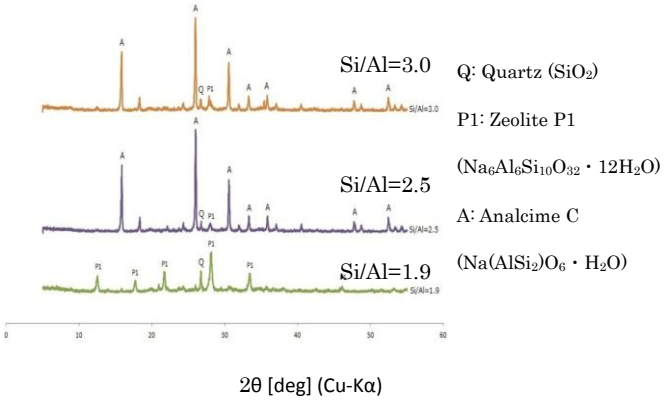

Fig.3 X-ray diffraction patterns of zeolites adjusted to different Si/Al ratios (120℃, 2M NaOH)

Figures 1, 2 and 3 showed that quartz was gradually dissolved in increasing concentration of alkali solution, temperature, and Si/Al ratio. Figures 2 and 3, showed that both increasing temperature and Si/Al ratio can convert Zeolite P1 (Si/Al=1.67) to Analcime C (Si/Al=2) which has a Si-rich structure.

3.2 Cation-exchange capacity

Table.1 shows the Cation-exchange capacity (CEC) values of zeolite products.

Table.1 CEC values of products obtained on various alkali concentrations, temperatures, and Si/Al ratios

Zeolite Preparation Conditions/Parameter		CEC value [meq/100g]	phase
NaOH concentration (Si/Al=1.9 120℃)	1M	131.655	Zeolite P1
	1.5M	159.795	Zeolite P1
	2M	170.952	Zeolite P1
	2.5M	127.300	Zeolite P1 & Unnamed zeolite
	3M	103.850	Unnamed zeolite
Temperature (Si/Al=1.9 2M NaOH)	100℃	150.840	Zeolite P1
	120℃	170.952	Zeolite P1
	150℃	80.448	Analcime-C
Si/Al Ratio (120℃ 2M NaOH)	1.9	170.952	Zeolite P1
	2.5	83.800	Analcime-C
	3.0	97.208	Analcime-C

The highest CEC value was measured at 170.952 meq/100g (Zeolite P1) which was treated with 2M NaOH, and synthesized at 120℃ without Si/Al adjustment. In Fig.1, this sample got the highest intensity in XRD plot which signifies that the crystal structure was completely formed and this is considered as the reason of high CEC. In Fig.2 and 3, Analcime C was generated. The more substitution of Al for Si, the larger charge deficiency occurs, and the more cations required for electrical neutrality[3]. Because the Si/Al ratio of Analcime C is more than the one of Zeolite P1 (Si/Al=1.67), Analcime C showed a lower CEC.

3.3 Ammonium ion adsorption

In this study, the adsorption time is 3h, and the amount of adsorption was measured by back titration method. The maximum NH_4^+-adsorption capacity of Zeolite P1 is determined by Langmuir adsorption isotherm at 46.729 mg/g, and the coefficient of determination is 0.9985. Langmuir adsorption isotherm is plotted in Fig.5.

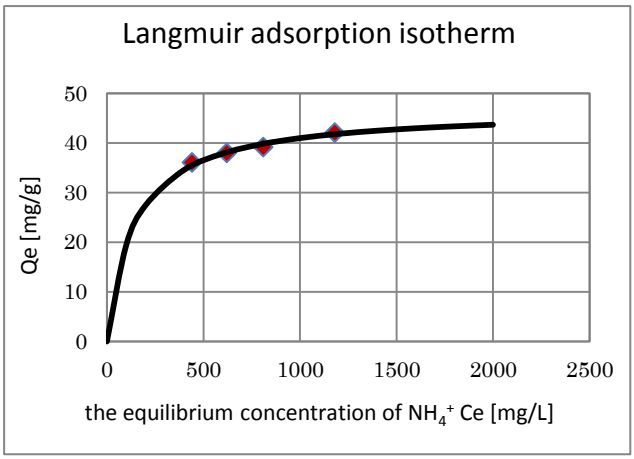

Fig.5 the Langmuir adsorption isotherm of Zeolite P1

4. Conclusions

The recycle of lake sludge is successfully completed in this study. Types of zeolites can be changed by adjusting alkali concentrations, temperatures, and Si/Al ratios. A relatively higher NH_4^+ adsorbent Zeolite P1 was successfully synthesized from lake sludge by hydrothermal synthesis. According to Fig.5, the experimental values fit the Langmuir isotherm very well. By using the Langmuir adsorption model, the maximum NH_4^+-adsorption capacity of Zeolite P1 is measured at 46.729 mg/g. This result is better than those of NaA (44.3mg/g) and faujasite (37.45mg/g), so Zeolite P1 can be considered as a relatively higher quality adsorbent for ammonium ion.

Reference:

[1] Yan Shao, Synthesis of Zeolites from Lake Sludge, International Development Engineering, School of Science and Engineering, Tokyo Institute of Technology

[2] Ayla Arslan, Sevil Veli, Kocaeli University, Turkey (2011)

[3] Japan Association of Zeolite, Zeolite conference home page, http://www.jaz-online.org/, Retrieved in January 13, 2013

衛星雲画像を用いた海風前線の推定および都市が海風に与える影響

学籍番号：09-04196　氏名：大久保　洸平　　指導教官：神田　学

1　はじめに

海風は高温化した都市を冷却し、汚染物質を輸送し、またゲリラ豪雨の引き金にもなりうるため、その挙動を把握することは重要である。都市化と、海風侵入遅延について、蒲生[1]、大和ほか[2]は、それぞれ東京上空におけるブロッキング効果、都市風下域での前線の停滞を、地上観測データを用いることにより指摘している。しかし、都市化と海風前線の内陸侵入の実態をより詳細に把握するためには、現状の地上観測データのみでは、時空間精度が十分であるとは言い難い。そこで、本研究においては、時空間解像度の高い衛星雲画像を導入し、かつ地上気象データも用いることで、都市が海風前線侵入に与える影響について明らかにすることを目的とした。

2　雲画像追跡法と地点法との対応について

この章では、衛星雲画像を用いて海風前線位置を推定する雲画像追跡法を提案する。そして雲画像追跡法と、従来の方法である地点法（地上観測物理量の時系列データの変化から前線到着時刻を推定する方法）とを比較し対応を見る。

データは、雲画像追跡法においては衛星雲画像、地点法においては、関東 7 都道府県の AMeDAS 及び環境省大気汚染局物質広域監視システムの地上観測データを使用した。なお風速は観測地点ごとに観測高度が異なっていたため、解析に先立ち高度補正を行っている。

雲画像追跡法では、輝度値変化の大きいところを海風前線と推定した。図 1 において今回着目する東京湾、相模湾から北上する前線は赤線（図 4 では緑色）で、その他の前線については紫色で示してある。次に地点法との対応を見る。図 2 から、風速、風向が前線を境として海風域では風速が大きく、風向が海風（南風）モードになっていることが分かる。また図 3 から前線上で容積絶対湿度の上昇が見られる。以上より、雲画像追跡法により推定した海風前線位置は、地点法と対応が取れることが分かった。また、いくつかの海風イベントでは、相模湾海風前線上で雲が確認されず、雲画像追跡法で前線を引くことができなかったので、地点法から推定した前線を重ね、次章でのパターン分類を行った。

3　海風前線の時空間発展のパターン分類

解析対象日は 2011 年、2012 年の 7，8，9 月の 11 事例である。全日、既存研究[1]を参考に抽出した海風日に含まれる（日照時間 7 時間以上、日中、降水なし、日平均風速南西から南東）。これを、海風前線の時空間発展の仕方に着目し 4 種類に分類した。以下に各パターンの特徴を記す。

①　2 海風収束による楔形前線の楔形が一旦解消さ

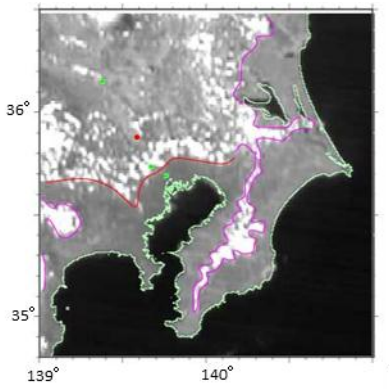

図 1　雲画像と、推定された前線の重ね合わせ(2011 年 9 月 14 日 14 時) 赤丸はさいたまを表す。緑丸は北から熊谷、練馬、東京を表す。

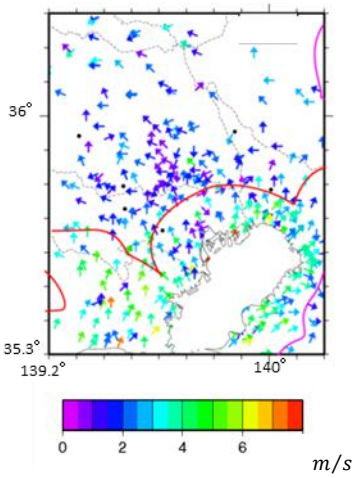

図 2　風系場と、推定された前線の重ね合わせ（図 1 と同時刻）

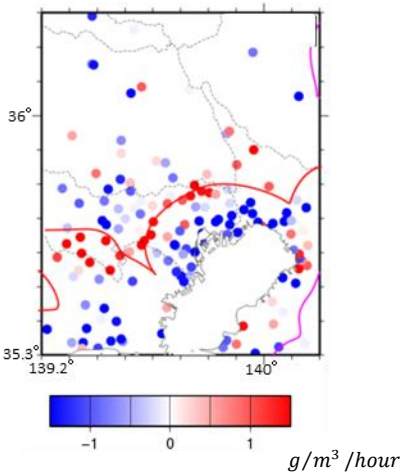

図 3　絶対湿度の変化量と、推定された前線の重ね合わせ（図 1 と同時刻）

れ、さいたま付近において再び楔形前線を形成する（図 4(a),(b),(c)にて例証)

② 2 海風収束による楔形前線が見られず、さいたま付近において初めて楔形前線が形成される

③ 2 海風収束による楔形前線が、その形状のままさいたま方向に移流する（図 4(d),(e),(f)にて例証)

④ 2 海風収束による収束雲がその位置にとどまる

ここで 2 海風収束とは、東京湾と相模湾からの海風の収束のことを意味する。それぞれの事例数は、順に 4，1，4，2 であった。

ここからは、海風前線侵入に対する都市影響を議論する上で重要だと考えられる、さいたま付近での楔形前線に着目し､その形成過程を議論するために、

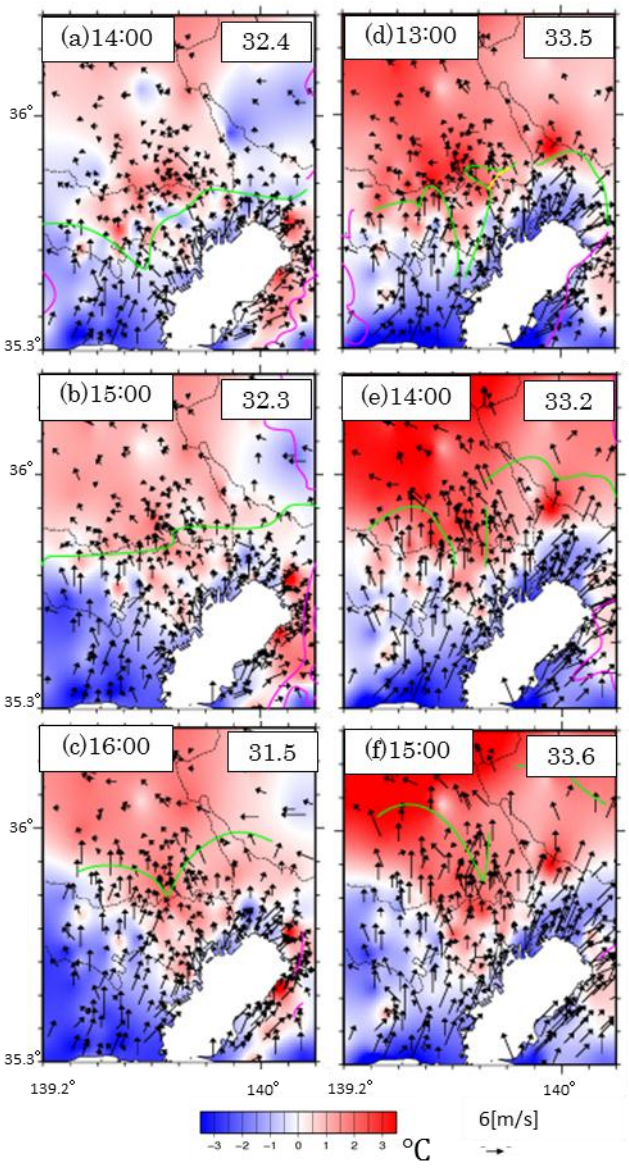

図 4　2011 年 9 月 14 日の 14 時から 16 時(a),(b),(c)および 2012 年 7 月 28 日の 13 時から 15 時(d),(e),(f)における前線と地点データの重ね合わせ

分類 1、分類 3 に注目し説明していく。

図 4 に分類 1 の 2011 年 9 月 14 日(a),(b),(c)、分類 3 の 2012 年 7 月 28 日(d),(e),(f)の海風前線と領域内の平均気温（図中右上[℃])からの偏差、そして風向風速とを重ね合わせた時系列データを記す。(a)で、2 海風の収束による楔形前線が確認できるが、(b)には一旦その楔形は解消される。(c)にさいたま付近で再び楔形前線が確認される。(c)の楔領域において、風速低下、及び風の収束が生じ、また高温化していることが確認される（図中の黄丸)。風速低下領域は，高層建物群による運動量粗度の増加領域に対応している。つまり、(c)に形成される楔形前線は、2 海風収束によるメソ影響ではなく、都市（局所）影響による海風遅延の結果と考えられる。一方、図 4(d),(e),(f)を見るといずれの時間にも､2 海風収束による楔形前線が風向きに対応して（図中の黄丸）さいたま付近の高温域に侵入していくことが確認できる。さいたま付近での楔形前線の形成は両ケースに共通するが、後者の事例ではメソ影響か、都市影響（熱空気力学的作用に伴う収束)かの判断が難しい。なぜなら、関東広域での風系場が南東モードになっており、総観場の気圧傾度により移流されたとも考えられるためだ。メソ影響のみ、もしくはメソ影響と局所影響の 2 つの異なるスケールの現象が共に影響している可能性が考えられる。

4　おわりに

本研究では、新たに雲画像追跡法を提案した。そして、前線の時空間発展を分類することで、さいたま付近での楔形の前線形成過程を確認した。また海風侵入に対する都市影響も確認された。海風侵入のそれぞれのパターンに対する、局所影響、メソ影響を明らかにすることが今後の課題である。

参考文献

[1]　蒲生稔，海風前線位置を読み取る方法の比較，公害，vol. 26, p31-39, 1991

[2] 大和広明，三上武彦，高橋日出男，夏季日中における首都圏のヒートアイランド現象に海風が与える影響，地学雑誌，vol. 120，pp. 325-340，2011

Measurement of audible sound due to crushing progression of snail fossils

Student Number: 09_08691 Name: Wenjie WU Supervisor: Thirapong PIPATPONGSA

1. Introduction

Sound wave has been uniquely and sensitively detected tiny changes of micro level configuration at the grain level because vibrations in granular material are qualitatively different from those found in solids and liquids[1-2]. Crack development and particle crushing in brittle materials can also produce acoustic effect; therefore, acoustic emission (AE) has emerged as in-situ techniques to evaluate rock slope stability[3]. Audible sound of crushing progress can be observed, and might be used to monitor crack developments inside the slope of brittle materials. The large deposit of thickness about 10 meters of snail fossils aging around 12-13 million years has been discovered at the Mae Moh open-pit lignite mine in Thailand since 2003. Due to crushability of snail fossils, audible sound of crushing progress can be observed and used to monitor crack developments inside the slope of snail fossils. This research aims to find the characteristic of the crushing sounds of snail fossil particles under various conditions.

2. Review of the previous study

The snail deposit at the Mae Moh open-pit mine, which is under operation of Electricity Generating Authority of Thailand (EGAT), is regarded as the thickest shell bed in Thailand[4]. The preservation area of snail fossils located a southwest pit has been assigned to prevent damages from mining activities. The detailed studies of characteristics of snail fossil are required in order to preserve this geological heritage while developing the energy resources. As being brittle inhomogeneous material, the layer of snail fossils would lose its strength after exposing to external environment for long time. Therefore, non-invasive monitoring using audio measurement was carried out in a laboratory level for measurement and analysis of crushing sound under compressive loading using commercial microphone[5]. Based on the previous study[5], crushing sounds of snail fossils under compressive loading were recorded by microphones with connection to stethoscopes attached to the oedometer. Noise filtering technique and sound wave analysis were conducted. At laboratory level, linear relationship between the cumulative counts and cumulative settlement can be confirmed.

3. Experimental program

In extension to the previous studies which used snail specimens, this research uses snail fossil particles as the specimen, which were collected from subsurface outside the preservation area and prepared by water sedimentation technique in order to make the sample uniform. Each sample was carefully prepared with the exact ratio of percent finer by weight of each particle size following the grading of the snail fossils after removal of big particle as summarized in Table1.

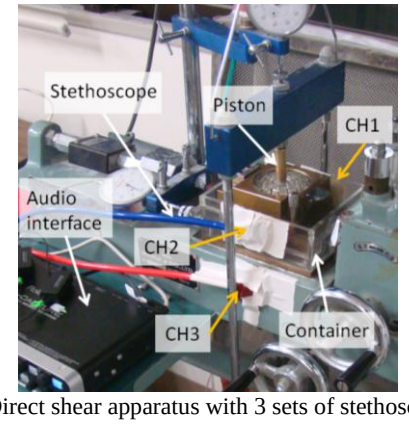

Fig. 1 Direct shear apparatus with 3 sets of stethoscope and microphone connection to three various locations

Table1 Composition of the sample

Sieve No.	Diameter (mm)	Mass (gram)	Percent retain
#20	0.85	30.3	46 %
#40	0.425	19.7	30 %
#60	0.25	9.0	14 %
#100	0.15	4.6	7 %
#200	0.075	2.4	3 %

Table 2 Experiment program where σ′ is vertical stress

Condition	Shearing mode	Sample No.	σ′ (kPa)	OCR
Dry	Constant load	B-DCL14	50	1
		B-DCL15	200	1
		B-DCL16	400	1
	Constant volume	B-DCV11	400	1
Wet	Constant load	B-WCL1	50	1
		B-WCL2	50	8
		B-WCL3	50	4
		B-WCL4	100	1
		B-WCL5	200	1
		B-WCL6	200	2
		B-WCL7	300	1
		B-WCL8	400	1
	Constant volume	B-WCV1	50	1
		B-WCV2	50	8
		B-WCV3	50	4
		B-WCV4	100	1
		B-WCV5	200	1
		B-WCV6	200	2
		B-WCV7	300	1
		B-WCV8	400	1

Direct shear tests were performed by 2 steps: consolidation and shear. Consolidation test is undertaken by applying a normal pressure to a sample and measuring the vertical settlement. Shear test is undertaken by applying shear force and measuring the horizontal displacement. After complete the experiment, the sample was removed and followed by sieving analysis to detect a degree of crushing. Twenty sets of direct shear test in total were conducted in dry and wet conditions under constant pressure and constant volume with different values of over-consolidation ratio (OCR). The amount normal pressure is varied by 50, 100, 200, 300, 400 kPa. After the end of consolidation, the sample was sheared with a shear rate of 0.2 mm/min to reach a shear displacement of 8 mm. Moreover, crushing sound of fossils generated under the consolidation test and shear test were recorded simultaneously by 3 sets of stethoscope connected to miniature microphone attached to the plastic frame of shearing box and direct shear apparatus as shown in Fig. 1.

4. Experimental results

The results of direct shear test are shown in Fig. 2 for comparison between shearing modes in constant load and constant volume. Similarly, comparison between samples prepared in wet and dry conditions also show the same result; therefore, indicating that no matter the shear test was conducted in constant load or volume condition, or whether the sample is wet or dry, the obtained angle of friction is the same.

Sound wave data were filtered by low-pass filter (LPF) at 8 kHz, resampled with frequency 16 kHz down from 44 kHz, finally filtered by high-pass filter (HPF) at 3 kHz using software

GOLDWAVE. By setting a threshold value, a MATLAB script applying acoustic emission algorithm counts the pulses which are over the threshold line. Under consolidation test, a linear relationship between cummulative count and settlement of dry samples can be confrimed as shown in Fig. 3. The reason why the result of B-DCV11 was totally different others although the process were exactly the same is possibly a run out of battary of microphone. No particular relationship between cummulative count and settlement of wet samples under consolidation test as shown in Fig. 4. The crushing sound wave could not be perfectly recorded by the stethoscope through water and plastic shear box as sound medium. Some noice due to the sound caused by placing the weights might be recorded time to time.

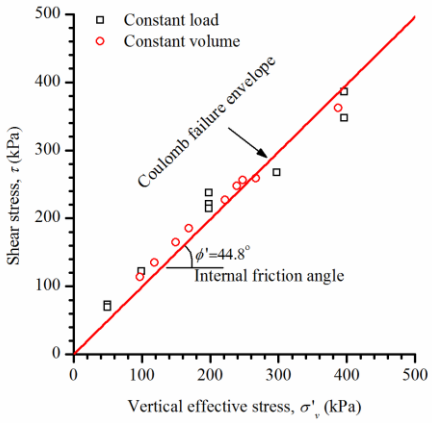

Fig. 2 Comparison between constant load and constant volume

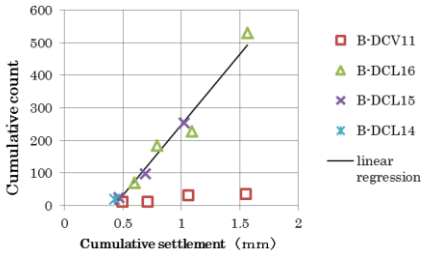

Fig. 3 Cumulative count-Settlement of dry sample

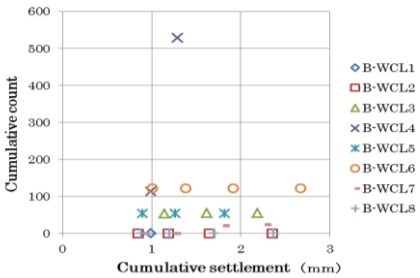

Fig. 4 Cumulative count-Settlement of wet sample

Under shear stage, the number of the filtered waves over the threshold line was counted every 100 second by using MATLAB. After checking several threshold values, the value around 0.0003 was found suitable. Fig.6 shows the result of B-DCL16 (dry, constant load, shear under 400kPa). A linear relationship is found between cumulative count and horizontal displacement from the sound data recorded by Channel 1, but was extremely different from sound data recorded by Channel 2 although the result should be similar because the stethoscopes of Channel 1 and Channel 2 were placed at two sides of the shear box and the same distance. GOLDWAVE was used to observe the sound wave of B-DCL16. Figs.5 and 6 visualized the sound wave for both the original and the processed data started from 29′02″ to 29′18″. For comparison, the processed data based pm sound wave recorded by Channel 2 is in Fig 7. It can be considered that the sound wave caused by the direct shear apparatus might lead to the result of linear relationship shown in Fig.8.

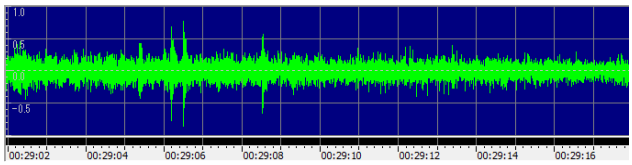

Fig. 5 Original sound data of B-DCL16 (CH1) during shearing

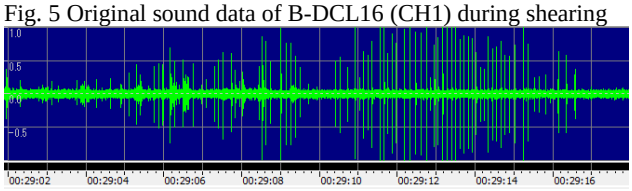

Fig. 6 Filtered sound data of B-DCL16 (CH1) during shearing

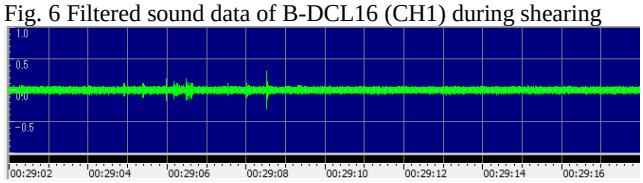

Fig. 7 Filtered sound data of B-DCL16 (CH2) during shearing

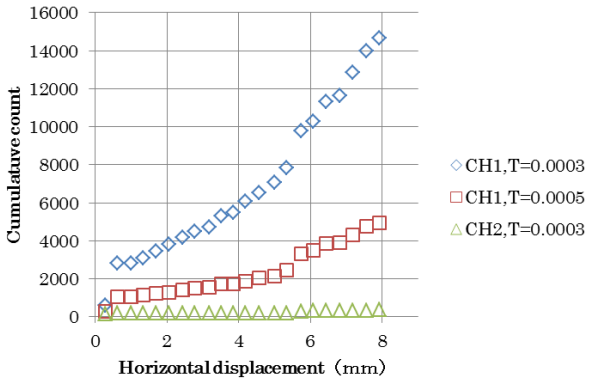

Fig. 8 Cumulative count-horizontal displacement of B-DCL16

5. Conclusion

Linear relationship between the cumulative counts and cumulative settlement can be confirmed on for dry sample of snail fossil particles at laboratory level. Under shearing stage, crushing sound was affected by noises of apparatus. Sound filtering technique is required in the subsequent research.

References

1) K. Tanimoto and Y. Tanaka: Yielding of soil as determined by acoustic emission, Soils and Foundations, 26(3), pp.69-80, 1986.
2) C. Liu and S.R. Nagel: Sound in sand, Physical Review Letters, 68(15), pp.2301-2304, 1992.
3) M. Otsu: Characteristics and Theory of Acoustic Emission, 2nd Edition, Morikita Publishing, 2005 (in Japanese).
4) W. Songtham, et al.: Middle Miocene Molluscan Assemblages in Mae Moh Basin, Lampang Province, Northern Thailand, ScienceAsia, 31(2), pp.183-191, 2005.
5) S. Kitakata: Crushing sound analysis of snail fossils under compressive loading using audible frequency measurement, Tokyo Institute of Technology, Bachelor Thesis, 2012.

Image Coding with 1D Discrete Wavelet Transform using Line-based Prediction

Student Number：09_11888　Name：SHIYU ZHOU　Supervisor：Yukihiko YAMASHITA

1 Introduction

The rapid development of information communication technology has enabled to use not only texts but also still images or videos for communication. However, the amount of information of digitized images and videos is very huge. Therefore, the image coding methods have been invented to reduce irrelevance and redundancy in image data and to store or transmit them in an efficient form.

JPEG is one of the commonly used methods of lossy compression for still images [3]. In the coding process of JPEG, an image is usually split into blocks of 8×8 pixels, and each block is transformed by the discrete cosine transform (DCT). Therefore, JPEG suffers from a problem that visual degradation called block distortion is observed in its decoded image. JPEG2000 solved the problem by using the discrete wavelet transform (DWT). Since DWT has no blockwise process, DWT can solve the problem of block distortion [2, 4, 5].

Prediction is another key technology to enhance the performance of image coding. Since it is difficult to combine prediction with the 2D DWT used in JPEG2000, in this paper, I propose to use 1D DWT and combine with prediction for image coding, develop a prediction program, and evaluate it by experimental results.

2 Discrete wavelet transform (DWT)

Daubechies proposed DWT for multiresolution signal analysis [1]. Its analysis process is as follows. An input signal is split into a low and a high frequency components by a low and a high pass filters. Both components are downsampled by 1/2 and the approximation and the detail coefficients are obtained respectively. The approximation coefficients are iteratively split as an input signal. Its synthesis process is almost the opposite of the analysis process. After the approximation and the detail coefficients are upsampled and filtered by a low and a high pass filters, respectively, the original signal is restored by the sum of both signals.

3 1D wavelet transform with line-based prediction

Since an image is a 2D signal, 2D DWT is used for image coding. An input image (I) is split into approximated and detailed coefficients both vertically and horizontally. Fig. 1 (a) shows the coefficients of DWT. For examples, (H, L) indicates horizontally detail and vertically approximation coefficients of the input image (I), and (LL, LH) indicates horizontally approximation and vertically detail coefficients of (L, L).

However, if we introduce prediction to 2D DWT, the precise prediction is difficult because of a distance of several pixels between the already decoded pixels and pixels to be decoded. To solve this problem, I propose a new usage of DWT, the 1D DWT, in which they are adjacent. In 1D DWT for images, horizontal or vertical transform is performed alternately. Fig.1 (b) shows the coefficients of DWT. For examples, (H, I) indicates horizontally detail and vertically not transformed coefficients of the input image (I).

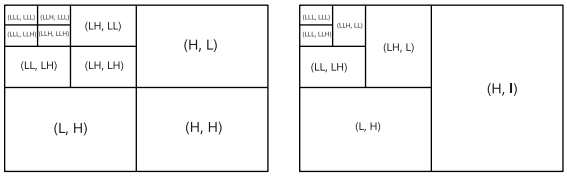

(a) 2D DWT　(b) 1D DWT

Fig. 1: Coefficients of DWT

Fig.2 shows the block diagram of prediction process in the proposed coding scheme. The prediction is done line by line in a target image. In the prediction process, we only have to predict its detail coefficients, since the approximation coefficients are given. The already decoded lines are called the reference lines and the line to be predicted is called the target line.

The detail of prediction process is as follows. **1)** Restore the low frequeny component of target line from approximate coefficients. **2)** Predict the target line by using the reference lines and the low frequency component of target line (Its detail is described below). **3)**

Transform the predicted line by 1D DWT and obtain detailed coefficients. **4)** Quantize the detail coefficients. **5)** Output the quantized difference between the true detailed coefficients and the predicted ones.

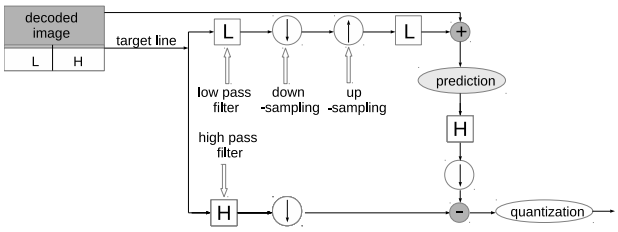

Fig. 2: Block diagram of prediction process

For the line-based prediction, I used the linear prediction with clustering. First, I extracted blocks which size is $b_x \times b_y$. Assume that 1D DWT is done horizontally, y is the vertical coordinate of the block. I set the line at $y = b_y$ to the target line, and the lines at $y = 1, 2, \ldots, b_y - 1$ to the reference lines. Then the block can be expressed by a $(b_x b_y)$-dimensional vector $\boldsymbol{u}$. Let m be the averaged value of all components in $\boldsymbol{u}$, and $\boldsymbol{v}$ be the normalized vector $\frac{\boldsymbol{u}-m\mathbf{1}}{\|\boldsymbol{u}-m\mathbf{1}\|}$, where $\mathbf{1}$ is a vector of which all components are one. Let p and q be the value of target pixel and its normalized version $\frac{p-m}{\|\boldsymbol{u}-m\mathbf{1}\|}$.

For the precise prediction, I cluster the normalized blocks according to their features to make the categories, Ω_c $(c = 1, 2, \ldots, C)$. The k-means method is applied for the clustering. The prediction model in Ω_c is given by

$$q = \langle \boldsymbol{a}_c, \boldsymbol{v} \rangle + b_c, \tag{1}$$

where $\boldsymbol{a}_c$ and b_c are constants for linear prediction. For training data $\boldsymbol{v}_i$ and q_i $(i = 1, 2, \ldots, N_c)$ in Ω_c, $\boldsymbol{a}_c$ and b_c are decided to minimize the following criterion:

$$\sum_{i=1}^{N_c} |q_i - \langle \boldsymbol{a}_c, \boldsymbol{v}_i \rangle - b_c|^2. \tag{2}$$

4 Experimental Results

For experiments, I used the standard image Lenna (Fig. 4). Table 1 shows the mean squared error of the target pixels. From Table 1, we can see the error decreases as the block size and the number of clusters C increased. However, the errors are still large, we have to develop a more precise method.

(a) Original image (b) Predictive image

Fig. 3: Original and predicted images

Table 1: Averaged estimation error of Lenna

	Number of clusters			
bx X by	16	32	64	128
3 X 3	791.645	790.853	789.367	787.645
5 X 3	773.346	770.091	768.156	768.013
7 X 3	771.073	769.013	767.265	765.855

5 Conclusions

In this paper, I proposed an image coding with 1D DWT using line-based prediction, and evaluated the proposed prediction method by experimental results. For future works, I have to develop an image coding system to validate the prediction and investigate prediction methods to improve the accuracy.

References

[1] I. Daubechies, "Ten Lectures on Wavelets," Society for Industrial and Applied Mathematics, Philadelphia, 1992

[2] M. Vetterli,J. Kovaevi, "Wavelets and Subband Coding," PrenticeHall, Englewood Cliffs, 1995.

[3] Sadayasu Ono, Junji Suzuki, "Achievement method of comprehensible JPEG/MPEG2," Ohmsha, Tokyo, 1995 (in Japanese).

[4] C. S. Burrus, R. A. Gopinath, and H. Guo, "introduction to Wavelets and Wavelet Transforms: A Primer," PrenticeHall, Englewood Cliffs, 1997.

[5] Geoffrey M. Davis, Aria Nosratinia, "Wavelet-based Image Coding: An Overview," IEEE Trans. on Circuits and Systems for Video Technology, vol . no. 6, pp.243-250, June. 2002.

A Pareto frontier analysis of household budget and environment for energy saving goods

省エネルギー商品に対する家計予算と環境負荷低減効果のパレート効率性分析

Student ID: 09_12244 Name: Ryoya SUEHARA Supervisor: Naoya ABE

1 Introduction

In 1970s, Japan had suffered from the oil crisis, and the Japanese government has made efforts to secure the energy supply. At the same time, energy conservation activities, which has been mainly taken by private companies for profit, has also become popular among the ordinary people. The central government and local governments now enhance the subsidy programs on energy saving device to households to promote energy conservation activities in the residential sector. The subsidized goods are relatively expensive to conventional goods such as lighting, air-conditioners, etc. Besides, the energy crisis has become a more serious issue after the 2011 Tōhoku earthquake and tsunami and the subsequent nuclear power plant accident, the public attention is being focused on the energy conservation activities. However, Whether households can afford to buy energy saving goods is depends on their budget.

This paper aims to evaluate the trade-off between economy and environment. More specifically, the economy means the saving amount, and the environment means the amount of CO_2 emission reduction of a household. To handle these aspect, multi-objective optimization problem are solved and the Pareto optimal solutions of each problem are obtained. Finally, the fairness of the subsidy programs in Japan is discussed.

This paper focuses the four energy conservation goods; (1) residential photovoltaic systems(PV), (2) residential cogeneration systems(ENE · FARM, EF), (3) solar water heating systems(SWH), and (4) Eco-cars(Prius PHV, EC). In addition, Ōta ward, one of the Tokyo's 23 wards is focused.

2 Subsidy programs and households' incomes

2.1 Subsidy programs on energy conservation goods

The inhabitants of Ōta Ward can enjoy the subsidies offered by the central government, Tokyo Metropolitan Government, and Ōta Ward. For instance, the subsidy on PV is determined by the capacity of the system represented by kW and the same can be said of SWH. EF and EC can not be divided, therefore, the subsidies are determined by the number of systems installed. In this study to simplify the problem, the average installed capacities are calculated with respect to PV and SWH. The average capacity of PV installed in 2011 is about 4.3kW(J-PEC, 2011), and the average capacity of SWH is $3m^2$(SSDA, 2012).

Table 1: Amount of subsidy for each good

Goods	PV	EF	SWH	EC
Subsidizer				
Central Gov.	129	470	0	672
Tokyo Metropolitan Gov.	431	0	210	0
Ōta Ward	216	0	27	0
Total amount of subsidy	776	470	237	672

[Unit: thousand yen per good]

2.2 Households' incomes

Households' decision makings can be influenced by various things in practice. This study, however, is assuming that their decision makings are influenced by their money in their hand; that is, the difference between their savings and liabilities (*real savings*). The data of annual income of Ōta Ward, and the savings and liabilities of workers' households in Japan are used to estimate their budget constraints(shown in tables 2 and 3 respectively).

Table 2: Annual income of the inhabitants Ōta Ward

Less than 5,000	5,001 to 9,999	More than 10,000
58%	32%	10%

Gini index: 0.412

Table 3: savings and liabilities of workers ' households

Income group	≤ 5,200	5,201 to 9,980	≥ 9,981
percentile	40%	50%	10%
Homeownership rate	60%	77%	85%
real savings	2,640	5,820	18,420

[Unit: thousand yen]

The half of the inhabitants have 2,640 thousand yen of *real savings* on average. Therefore, the budget constraint on that income class should be less than 2,660 thousand yen.

3 Methodology

3.1 Multi-objective problem optimization

A multiobjective optimization task considers several conflicting objectives simultaneously. In such a case, there is usually no single optimal solution, but a set of alternatives with different trade-offs, called *Pareto optimal solutions*, or non-dominated solutions. A multiobjective optimization problem are described as follows;

$$\begin{aligned} &\text{minimize} && \{f_1(\mathbf{x}), f_2(\mathbf{x}), \ldots, f_k(\mathbf{x})\} \qquad \text{(eq. 1)} \\ &\text{subject to} && \mathbf{x} \in S. \end{aligned}$$

involving k (≥ 2) conflicting *objective function* $f_i : \mathbf{R}^n \to \mathbf{R}$ to minimize simultaneously. The *decision variable vectors* $\mathbf{x} = (x_1, x_2, \ldots, x_n)^T$ belong to the nonempty *feasible region* $S \subset \mathbf{R}^n$. *Objective vectors* are images of decision vectors and consist of *objective function values* $\mathbf{z} = \mathbf{f}(\mathbf{x}) = (f_1(\mathbf{x}), f_2(\mathbf{x}), \ldots, f_k(\mathbf{x}))^T$. In multiobjective optimization, objective vectors are regarded as optimal if none of the other components can be improved without deterioration to at least one of the other components. More precisely, a decision vector $\mathbf{x}' \in S$ is called *Pareto optimal* if there does not exist another $\mathbf{x} \in S$ such that $f_i(\mathbf{x}) \leq f_i(\mathbf{x}')$ for all $i = 1, \ldots, k$ and $f_i(\mathbf{x}) < f_i(\mathbf{x}')$ for at least one index j.

3.2 Application of the the model

This study focuses the some trade-offs between two objective(See Table.4), for instance, the trade-off between the amount of the savings per year per ten thousand yen

(investment) and the amount of CO_2 emission reduction. the optimization problem is described as;

$$\begin{aligned} \text{minimize} \quad & \{1/f_a(\mathbf{x}), 1/f_b(\mathbf{x})\} \qquad \text{(eq. 2)} \\ \text{subject to} \quad & \mathbf{x} \in S_1. \\ f_a(\mathbf{x}) &= (\mathbf{s} \cdot \mathbf{x})/(\mathbf{p} \cdot \mathbf{x}) \\ f_b(\mathbf{x}) &= \mathbf{r} \cdot \mathbf{x} \qquad \text{(eq. 3)} \end{aligned}$$

It is assumed that the decision variable vector can take only 0 or 1. Therefore, S_1 is consisted of $2^4 = 16$ decision vectors. $f_a(\mathbf{x})$ represents the amount of savings per year, $f_b(\mathbf{x})$ represents the amount of CO_2 emission reduction. The inverse numbers are taken to resolve the problem into the model. **s** is the *saving vector* (**s** = [130 55 39 48]) and provide the saving abilities of goods(the amount of saving per year). **p** is the price vector (**p** = [1,600 2,290 63 3,770]) and provide the subsidized prices (price per system). **r** is the *reduction vector* (**r** = [1,611 1,500 580 829]) and provide the reduction abilities of goods(the amount of CO_2 emission reduction kg per year).

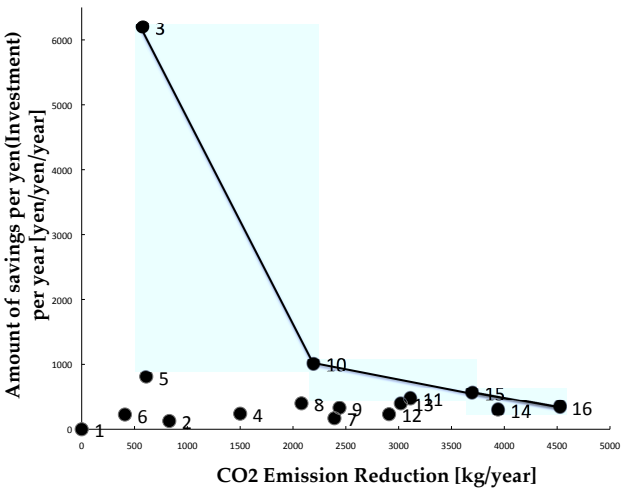

Figure 1: Pareto frontier

4 Results

The number of optimal choices increases as the budget constraint is relaxed. For households, the optimal solution is to choose choices 1, 3, 10, and 15. For governments, it is desired when choices 1, 2, 3, 8, and 16 is chosen. Therefore, the intersectional solution is choice 3, installing WHS only or installing all goods.

5 Conclusions and policy implications

The result shows that the optimal choices varied based on the household's strategy and budget constraint. When a household is interested only in the return of investment, they would choose choices 1and 3, no choice or installing only WHS. When a household is interested in both the return and the environment, they could choose choices 1, 3, 10, 15, 16. The governments seems to reduce the CO_2 emission as well as minimize the expenditure. Therefore, the desirable choices are choice 1, 2, 3, 8, 16. As a result, there are a few choices possibly being chosen. Moreover, the households who do not have their own house can not buy PV and SWH, and they mostly belong to the low income group. The governments should consider the fairness more in the process of policy design and implementation.

6 Further study

In this paper, the impact of Feed-in-tariff is not taken into account to simplify the problem. The households which install PV can sell their surplus electricity to electric power companies at the higher rate than the rate at which they buy electricity from the power companies. Therefore, the budget constraints could be changed only when the household install residential photovoltaic systems into its house. This impact would not be small and should be considered.

Moreover, The number of goods focused in this paper are only four. In fact, households decide their consumption from a great number of goods in their daily lives. When they purchase appliances, non-subsidized goods can appear in their options. This change in the choice set could influence the Pareto optimal choices.

References

[1] Japan Photovoltaic Expansion Center (J–PEC). 2011.

[2] Solar System Development Association (SSDA). *Solar System Data Book*. 2012.

[3] Branke, J., K. Deb., K. Miettinen, and R. Słowiński. 2008. *Multiobjective Optimization: Interactive and Evolutionary Approaches*. Germany: Springer.

Table 4: Results of frontiers

Choice	DMV				Actual	Max CO_2 &	Max Sv &	Max Sv/¥ &	Max CO_2/¥ and	Max CO_2/S¥ and	Max CO_2/S¥ and	Max Sv/¥ and	Min S¥ and
	PV	EF	SWH	EC	Cost [k¥]	Min cost	Min cost	Min Cost	min Cost	min Cost	max CO_2	max CO_2	max CO_2
1	0	0	0	0	0	○	○	○	○			○	○
2	0	0	0	1	3,770								○
3	0	0	1	0	63	○	○	○	○	○		○	○
4	0	1	0	0	2,290					○	○		
5	1	0	0	0	1,600	○	○						
6	0	0	1	1	3,833				Never appeared in Pareto frontier				
7	0	1	0	1	6,060						○		
8	0	1	1	0	2,353						○		○
9	1	0	0	1	5,370				Never appeared in Pareto frontier				
10	1	0	1	0	1,663	○	○					○	
11	1	1	0	0	3,890		○				○		
12	0	1	1	1	6,123						○		
13	1	0	1	1	5,433				Never appeared in Pareto frontier				
14	1	1	0	1	7,660	○	○						
15	1	1	1	0	3,953	○	○				○	○	
16	1	1	1	1	7,723	○	○				○	○	○

CO_2: the amount of CO_2 emission reduction, DMV: decision making vector, Sv: savings, S¥: yen subsidized.

Study on the Propagation of the Tidal Waves in the Mekong River

Student Number:09B13746 Name:Yuto TAKAHASHI Supervisor:Hiroshi TAKAGI

1. Introduction

There are many researches on floods in the lower Mekong River basin mainly focusing on the influence of the river discharge from the upstream of the river, but there has so far been little research that carefully considers the influence of ocean tides. Due to its low-lying nature, the region is very likely vulnerable to the influence of sea-level rise. The objective of this study is to investigate the characteristics of tidal waves traveling upstream.

2. Field survey

The authors carried out the field survey on March 2012 and obtained the bathymetric data and the water level of the Mekong River in Vietnam. Figs.1 and 2 show scenes of the measurement. These data are used in the numerical simulation.

Fig.1 Scene of measurement for depth of river (Left)

Fig.2 Scene of measurement for water level (Right)

3. Analysis of the characteristics of the water level in the lower Mekong River

The purpose of this study is to investigate the characteristics of water level (WL) associated with tides in Can Tho city which is the largest city in the Mekong delta region and located about 80km from the coast. Fig.3 shows the location of Can Tho.

In addition to WL measured by the authors themselves, the data of water level at every 15 minutes observed by MRC (Mekong River Commission) was obtained and used for a basic analysis. The data analysis have been made using the data at two WL stations in Dinh An which is a small town nearby the coast as well as Can Tho.

The amplitude spectrum is calculated by the fast Fourier transform for WL between 2009 and 2010. The result is shown in Fig.4. Both cities show that the amplitudes around half day, one day, and one year are remarkable. It appears that these amplifications are caused by astronomical tides with tidal constituents of M2/S2, O1/K1, Sa respectively. It is natural that WL at Dinh An indicates tidal patterns because it is located at a coast. However, it should be noted that WL at Can Tho, which is about 80km upstream from the coast, also indicates similar results. This means that the fluctuation of water level at Can Tho is mainly determined by astronomical tides. Therefore, it can be emphasized that an analysis on the flood in lower Mekong Delta should be carried out in consideration of astronomical tides as well as river discharges.

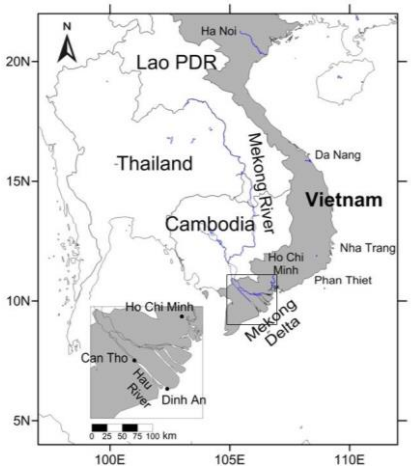

Fig.3 The lower Mekong River basin

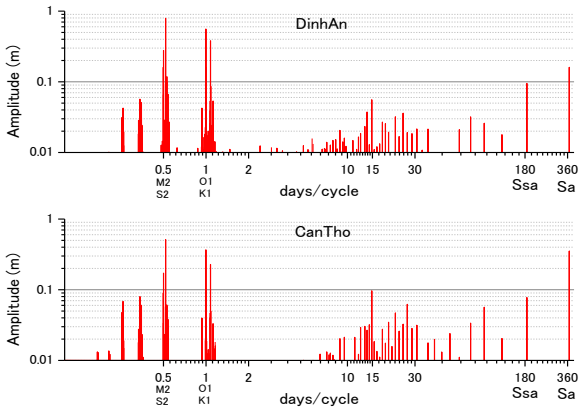

Fig.4 Amplitude spectrum (Top: Dinh An, Bottom: Can Tho)

4. Numerical simulation of tidal waves along the river

4.1 Conditions of the simulation

Since the detailed data necessary for the numerical simulation is scarce in the Mekong River, it is necessary to postulate some of these data such as river discharge (Q), Manning's coefficient of roughness (n), and the depth of river (h). Using the data of annual average amount of river discharge published by MRC, the estimated river discharges for three seasons (flood, normal, and dry seasons) are estimated to be Q=20000, 6000, 3000 m^3/s respectively. Manning's coefficient of roughness is n=0.03 and 0.06, the depth of river is h=20 and 15m which are roughly estimated by the bathymetric survey by the authors. Fig.5 shows the computational domain of the Mekong River and an example of WL during a tide propagates. The tidal propagation was simulated using Delft3D-FLOW originally developed by Delft University of Technology. The results were compared with the observed WL by the authors on March 2012.

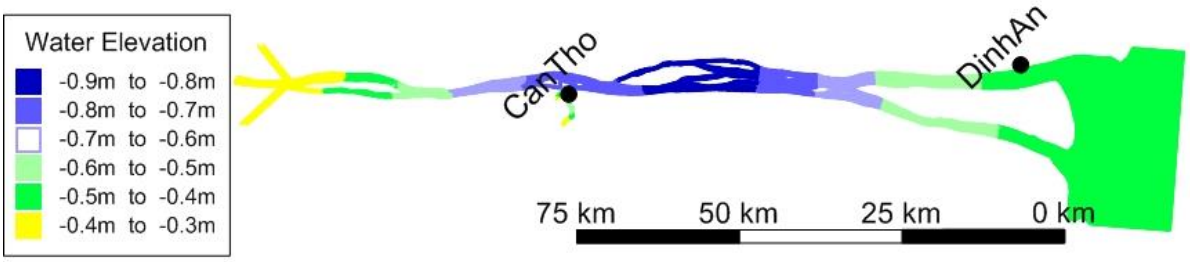

Fig.5 The computational domain of the lower Mekong River(10-Mar-2012 11:00).

4.2 Tidal damping

It is necessary to investigate the interaction mechanism between river flows and tidal waves in order to estimate WL in the lower river basin precisely. It is known that the amplitude of tidal wave is decreased as the amount of river discharge increases because the velocity of going downstream is added and the run-up is suppressed [1]. In the present research, the numerical simulation is performed in order to identify how river flows and tidal waves affect with each other.

5. Result and discussion

A series of simulations with changes in Q, n, and h were performed in order to identify the sensitivity to WL. Some of these results are shown in Fig.6 in which the simulation was performed for the settings of Q=6,000m^3/s, h=15m, and n=0.03 or n=0.06. The result shows that the tidal damping appears to be too large in the case of n=0.06, whereas the computational result with n=0.03 agrees well with the observed data at Can Tho in terms of both amplitude and phase.

Calculating the amplitude of tidal waves for 20 points at interval of 5km from the coast to the upper boundary of the model, the damping (or amplification) ratio of the amplitude (amplitude at a certain point divided by the value at the coast) is obtained as shown in Fig.7. Regardless of the difference in the river discharge, the tidal amplitude demonstrates a stable or slight increase up to about 50km and starts rapidly decreasing after 50km. Fig.7 also shows the width of the Mekong River at each point. It shows that the tidal damping tends to be accelerated as the width of river become narrow. This trend can be explained by the fact that the bottom friction that leads to decreasing the amplitude will increase as the tidal velocity gets increase when the wave travels along a narrow part of the river.

On the other hand, the damping effect by the difference of the river discharge seems to be unclear. One of the possible reason is that the horizontal 2D simulation used in the present research underestimates the vertical turbulence that may bring about a significant loss of energy.

6. Conclusions

- Computational result with Q=6,000m^3/s, h=15m, n=0.03 agrees well with the observed data at Can Tho in terms of both amplitude and phase.
- The numerical simulation shows that the tidal damping is accelerated by a narrow part of the river where tidal velocity significantly increases, whereas the influence of river discharges is not remarkable.

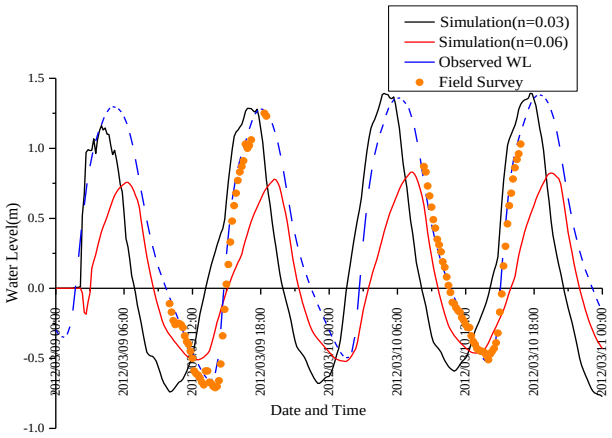

Fig.6 The result of simulation and the comparison of calculated result with measured value.

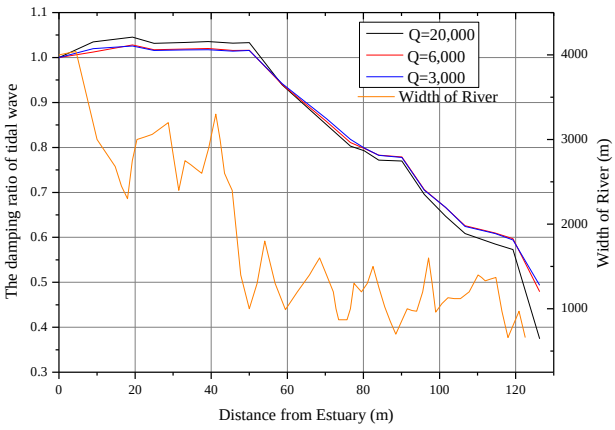

Fig.7 The damping ratio of tidal wave and the width of the river

References

[1] A.C. Horrevoets, H.H.G. Savenije, J.N. Schuurman and S. Graas. The influence of river discharge on tidal damping in alluvial estuaries, *Journal of Hydrology*, pp.1-3, 2004

Production of monomers for biodegradable plastics with lignin as raw material

Student Number:09_15277 Name: Ngoc Linh TRAN Supervisor: Ryuichi EGASHIRA, Hiroaki HABAKI

1. Introduction

Bio-base polyesters exhibiting smooth degradation have been widely studied as environmentally friendly polymeric material. They can be derived from renewable feedstock, thereby reducing greenhouse gas emissions. For instance, polyhydroxyalkanoates and lactic acid (raw materials for polylactic acid) can be produced by fermentative biotechnological processes using agricultural products and microorganisms. However the rate of these fermentative reactions is small, so production of these monomers in bulk is still difficult.

Kaneko et al. [1] reported that coumaric acid derivative homo-polymers which are one type of bio-base polyester showed smooth in-soil degradation. **Figure 1** shows chemical structures of various coumaric acid derivative monomers and synthesis of their polymers [1]

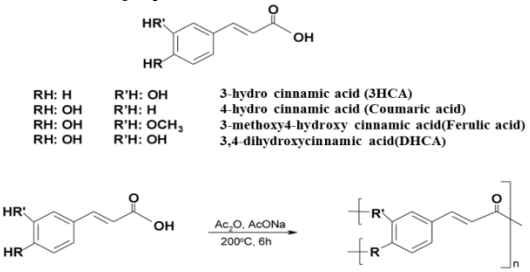

Figure 1: Chemical structures of various coumaric acid derivative monomers and synthesis of their homo-polymers

These coumaric and ferulic acids are contained as the main phenyl propane construction monomers in lignin [2]. Lignin is one of the major substances in plant together with cellulose and hemicellulose; however there are a great quantity of lignin residue in the world such as rice straw and pulp industry residue. Production of biodegradation plastics from lignin residue is one of effective methods to resolve the environmental problems.

In this work, the preparation of coumaric and ferulic acids from lignin is studied. The pyrolysis of lignin under steam atmosphere was conducted to decompose the complexity construction of lignin structure to simple substances. Liquid products from pyrolysis of lignin were analyzed by UV spectroscopy and high performance liquid chromatography (HPLC) to study the existence of coumaric acid and ferulic acid. After that, extraction experiment was conducted to recover the obtained acids. Moreover, the pyrolysis of the agriculture residue of rice straw, which contains about 19~21% lignin by mass, was also studied.

2. Experimental

Material. Lignin powder was purchased from Kasei Kanto Co. Coumaric acid and ferulic acid were purchased from Wako pure chemical Co. Rice straw was obtained from Hiroshima. Dried rice straw was ground and sieved to obtain particles ranging between 1.7 and 0.35 mm.

Pyrolysis. Figure 2 shows the schematic diagram of pyrolysis experimental system. The sample holder was filled with lignin or rice straw, and placed at the center of the pyrolysis reactor. Nitrogen and water were supplied during the pyrolysis. All of the gases flowing out from the end of the actor were sent to the liquid product trap to obtain the liquid product of crude pyroligneous acid (PCA). Non-condensable gases were discharged to open air. The experimental conditions for pyrolysis of lignin and rice straw are showed at **Table 1.** The thermal decomposition of lignin should take place at temperature above 350℃[4] and the temperatures of pyrolysis were fixed at 500℃, 600℃, 700℃, 800℃ with lignin, and at 600℃ with rice straw, respectively.

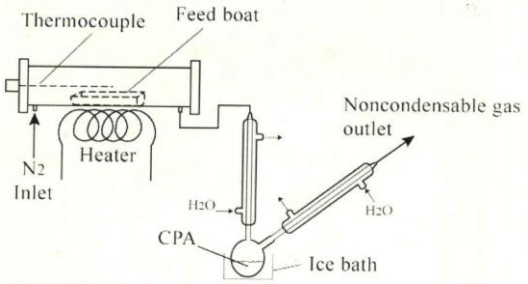

Figure 2. Schematic diagram of pyrolysis experimental system

Table1 Experimental condition of thermal treatment of lignin

Feed		Lignin (Rice straw)
Mass of feed	m_{Feed}[g]	12~15
Atmosphere	N_2	
Flow rate of atmosphere	f_{N_2}[mL/min]	50
Flow rate of moisture	f_{H_2O} [mL/min]	1
Temperature	T [℃]	500, 600, 700, 800
Holding time	t [h]	1

Extraction of coumaric acid from liquid products.

At extraction experiment, ether and then aqueous sodium hydrogen carbonate solution were added in liquid products one by one. The obtained acids in liquid products should be converted to sodium salt forms after reacting with sodium hydrogen carbonate, and dissolved in aqueous phase. Each phase of this process was analyzed by UV spectroscopy. The experimental condition of extraction is showed at **table 2**

Table2 Experimental condition of extraction of liquid products

Feed		Liquid products
Aqueous phase		Aqueous solution of $NaHCO_3$
Organic phase		Ether
Concentration aqueous solution of $NaHCO_3$	$C_{NaHCO3,aqe0}$[kmol/m^3]	0.01
Volume of feed	V_{feed} [m^3]	3.0×10^{-5}
Volume of aqueous phase	V_{aq} [m^3]	3.0×10^{-5}
Volume of organic phase	V_{org} [m^3]	3.0×10^{-5}
Temperature	T [℃]	298

Analysis of liquid products. Liquid products from the pyrolysis were analyzed by UV Probe 2.43 and HPLC (Shimada. Co). At HPLC analysis, the mobile phase is methanol. The mobile phase was delivered at a rate of 0.5 mL/min. The detection was monitored at 280nm.

3. Results and Discussion

Pyrolysis

The products obtained from the pyrolysis were solid, liquid, and gas ones. Because of the quantity of moisture supplied during heat treatment, mass of liquid products were greater than mass of feed material. In **Figure 3,** the blue and red points show the yield of solid products and fractional yield of liquid products relative to material.

In pyrolysis of lignin, there was a significant reduction in yield of solid products at higher temperature. In contrast, it only had a little change in the fractional yield of liquid products relative to feed material. Therefore, it was considered that the

gas products increased proportionally at higher temperature. In the temperature range from 500℃ to 800℃, the pyrolysis temperature had significant effects on the yields of solid and gas products, but it had little effects on the yield of liquid products.

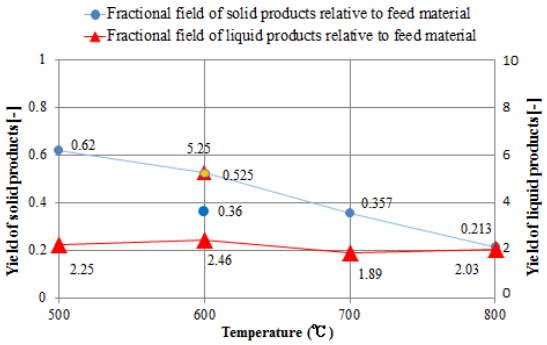

Figure 3. Fractional yield of solid products and liquid products relative to feed material

Comparing between pyrolysis of lignin and rice straw at 600℃, rice straw was degraded more than lignin. Liquid products from pyrolysis of rice straw were more than two times to these from lignin. It might be caused by the degradation of hemicellulose and cellulose in rice straw. These substances were degraded at lower temperature than lignin.

Figure 4 shows the UV spectroscopy of liquid products from pyrolysis of lignin and rice straw at 600℃. The wavelengths of the absorptions were observed at 311nm of coumaric acid, 322nm of ferulic acid and 274 nm of phenol, respectively.

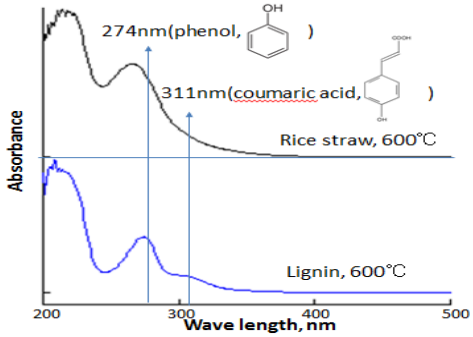

Figure 4. UV-spectroscopy of liquid products from pyrolysis of lignin and rice straw at 600℃

There were broad absorption bands with peaks around 260-280 nm in both the samples. Because the absorption at 322 nm was relatively small, only little amount of ferulic acid could be generated. The absorption at around 311nm was observed in liquid products obtained from pyrolysis of lignin. The absorption of coumaric acid was also at 311nm, as shown above.

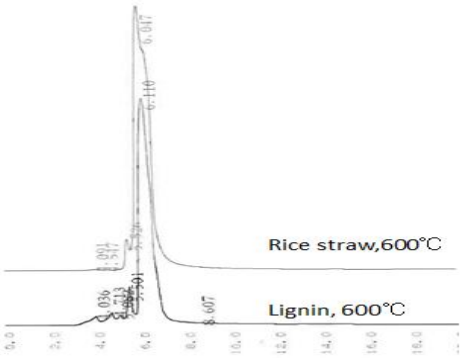

Figure 5. HPLC of liquid products from pyrolysis of lignin and rice straw at 600℃

It was found that the aqueous solutions of coumaric sodium salt showed absorption at around 286 nm. Mixture of liquid products and sodium hydrogen carbon solution presented the peak of 5.5 min which did not present at liquid products sample only. The result of HPLC analysis is showed at **Figure 5**

Then, the concentration of coumaric acid was quantified. The fractional yields of coumaric acid relative to feed material were shown in **Table 3**.

Table 3 Concentration of sodium salts of coumaric acid

Samples	Concentration coumaric acid in liquid products[mg/ml]	Fractional yield of coumaric acid relative to feed
Lignin 500℃	0.465	0.0010
Lignin 600℃	0.488	0.0012
Lignin 700℃	0.430	0.0008
Lignin 800℃	0.459	0.0009
Rice straw 600℃	0.464	0.0024

Although rice straw contained lignin with only about 0.2 by mass fraction, the yield of coumaric acid was greater than that with lignin. For examples, from these results, it could obtain about 2.4 g of coumaric acid from 1kg feedstock of rice straw. The yield of coumaric acid exceeded slightly in liquid products heat treatment at 600℃ than other temperature. Therefore, operating heat treatment of lignin at 600℃ should be preferable. However yield of coumaric acid from lignin heat treatment products was still small.

Extraction of coumaric acid from liquid products.

Figure 6 shows UV spectroscopy of liquid products, ether phase, aqueous phase

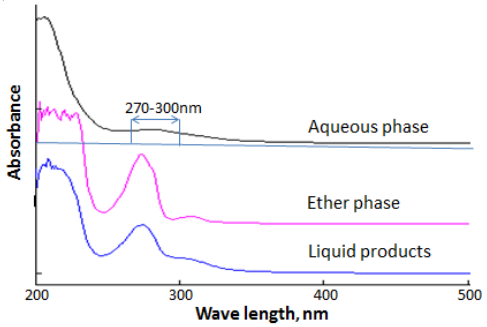

Figure 6. UV spectroscopy of liquid products, ether phase, water phase

The distribution coefficient, D_i, was defined as,

$$D_i = \frac{Concentration\ in\ water\ phase}{Concentration\ in\ ether\ phase}$$

Phenol was considered as the major impurity for the recovery of coumaric acid from liquid products. The D_is of coumaric acid and phenol were measured as 2.2 and 0.055, respectively with liquid products of thermal treatment of lignin at 600℃. Coumaric acid was extracted in the aqueous phase while most of phenol remained in ether phase. Although the purity of coumaric acid is still problem, this extraction experiment method can remove a quantity of impurities in liquid products away coumaric acid.

4. Conclusions

It can be concluded that coumaric acid exits in liquid products from thermal treatment of lignin. Thermal treatment lignin at 600℃ is most adequate to obtain more quantity of coumaric acid. Separation of sodium salt of coumaric acid from liquid products by HPLC is analytically succeeded. Small quantity of coumaric acid is extracted from main impurities in liquid products. It is necessary to take account of more efficient extraction method or thermal treatment experimental conditions to obtain more quantity and pure of coumaric acid.

References

[1]T.Kaneko, D.Kaneko, S.Wang, High-performance lignin-mimetic polyesters, Plant Biotechnology 27, 2010, 243-250

[2] S. M. Notley and M. Norgren, The Nanoscience and Technology of Renewable Biomaterials, ed. L. A. Lucia and O. J. Rojas, JohnWiley & Sons, Ltd, Chichester, 2009, ch. 7, pp. 173–205.

[3] Guedira, F., Pyrolise lente de la biomasse: comportement compare destourteux d'olives, de la bagasse de canne a sucre et la sciure de bois. Maroc, These (Docteur) – Universite Mohamed,1988, p. 122.

Tsunami Vulnerability Assessment in Tokyo Bay Using a Numerical Simulation

Student Number：09_16970　Name：Shouhei Nagase　Supervisor：Hiroshi Takagi

1. Introduction

Tokyo Bay has been considered to be safe against tsunamis because of its semi-closed shape that would effectively reduce the incoming tsunami energy. However, it is fact that a 3m tsunami was observed at the fishing port of the Chiba prefecture and a 1.5m tsunami was also observed in the Sumida River after the Great East Japan Earthquake on March 11th 2011 [1]. It should be noted that the observed tsunami height exceeds the estimated maximum level of 1.2m which was simulated by the Tokyo disaster prevention council in 1991. Facing unexpectedly large tsunami, it is required to reinvestigate the influence of tsunami on Tokyo Bay with the new findings and review the disaster mitigation plan in consideration of future possible tsunamis.

The aim of this research is to investigate the characteristics of tsunami propagation across Tokyo Bay and to identify the local amplification mechanism of tsunami heights due to a man-made structure such as floodgates and dykes.

2. Numerical simulation

In this research, the tsunami propagation was simulated using Delft3D-FLOW originally developed by Delft University of Technology.

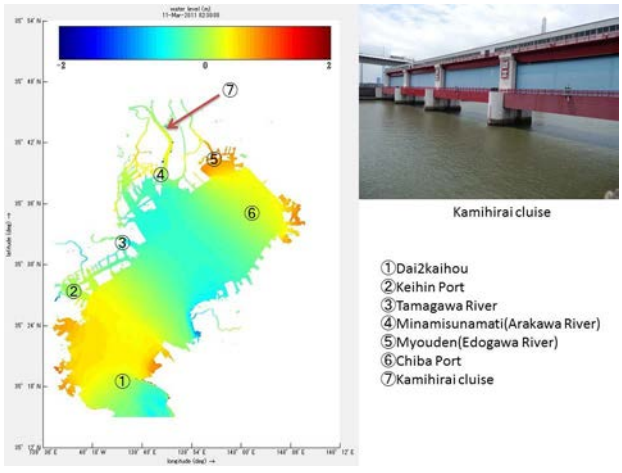

Fig.1 : Observation point

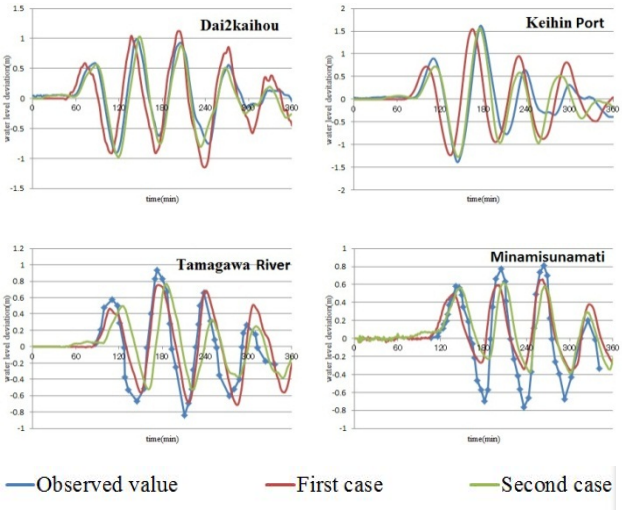

Fig.2 : Comparison between observed and calculated values

First, the simulation was performed for the broad domain with a coarse grid which encompasses the tsunami source generated by the earthquake on March 2011 [2]. In order to verify the model, the result was checked with several tidal gauges along the coastline in Tokyo Bay. Second, the simulation that is limited within the area of Tokyo Bay was performed in order to achieve the reduction of computational time which enables a number of computations repeatedly. For the second case, tsunamis were generated from the open boundary which is placed at the baymouth. The validity of the model was also checked in the same way.

3. Local amplification mechanism of tsunami

This research focuses on the resonance phenomenon that can increase tsunami heights in the bay when the natural frequency of the bay agrees with the frequency of tsunami. It is also hypothesized that the tsunami height would be amplified in front of a floodgate closed due to the reflection of tsunami and may result in increasing the flood risk round the area. To investigate these risks, several types of test tsunamis with different period of sinusoidal waves were generated from the open boundary.

Table.1: Calculation Settings

Item	Outline
Calculating area	Largest mesh(200m square mesh), Second mesh(40m square mesh) Third mesh(20m square mesh)
Time step	Δt=0.1sec
Tide level condition	Mean sea-level of Tokyo Bay (T.P.+0.0m)
Computation time	3-6hours (It changes according to a cycle)
Bathymetric data	Largest mesh: the Maritime Safety Agency data Second mesh: ditto Third mesh: uniformly T.P. -3.2m
Ground levels	It creates from 10m mesh data of Geographical Survey Institute
Relative roughness	0.025 is uniformly set to a water area

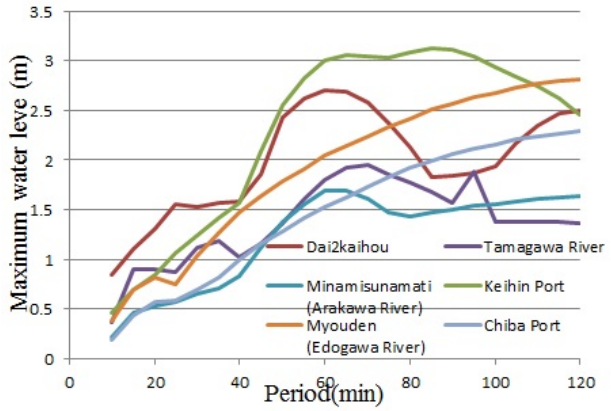

Fig.3: Maximum water level

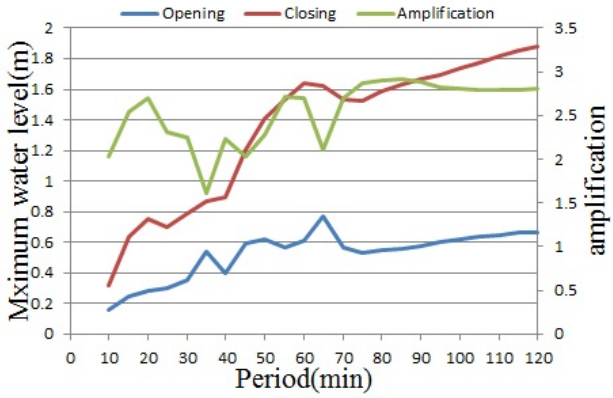

Fig4:Difference in maximum water level at the Kamihirai sluice between two different gate operational patterns: openig and closing

It is shown that the water level deviation tend to increase with an increase in period in Fig.3. Three out of five points show significant increases in water level around 50 to 90 minutes that clearly demonstrate the resonance. This result agrees with the analysis performed by Hino et al. [3] in which the range of natural oscillation period of Tokyo Bay is shown in between 60 and 90 minutes. Fig.4 indicates that the water levels in front of the floodgates are much larger when closing than when opening. This amplification can be explained by the reflection of tsunami in front of the gate closed. However, it appears to be excessive because the reflection can only explain the amplification that should be less than 2 times. One of the reasons for this excessive amplification is that the tsunami which breaks in the shallow water turns into a bore which causes mass transportation towards upstream, and eventually is accumulated in the front of the gate.

3. Conclusions

The numerical simulation is indispensable in order to estimate a future possible tsunami. In this research, the following conclusions are obtained:

- The tsunami simulation for the great tsunami on March 2011 was performed and validated its accuracy with the observed water elevations.
- The period of resonance in Tokyo Bay appears to be around 50 to 90 minutes, and the resonance causes significant increase in tsunami heights.
- The amplification of water level in front of a floodgate closed can be reached more than two times with that of a gate opened.

It is necessary to advance the research about the following subjects.

- Development of the tsunami risk evaluation methods under more complex conditions in consideration of the damaged dykes due to earthquakes and liquefactions.
- Numerical simulation which can incorporate the gate operation in the process of the calculation.

References

[1] Jun Sasaki et al., Behavior of The 2011 Tohoku Earthquake Tsunami and Resultant Damage in Tokyo Bay, *Coastal Engineering Jounal*, Vol.54, No.1, p.26, Mar.2012.

[2] Tatsuhiko Saito et al., Tsunami source of the 2011 Tohoku-Oki earthquake, Japan:Inversion analysis based on dispaersive tsunami simulations, *GEOPHYSICAL RESEARCH LETTERS*, VOL.38, Isuue 7(2011)

[3] 日野幹雄, 日野和子, 東京湾の進入長波に対する振動応答特性, 海岸工学論文集, 第 11 回, 1964.

CARBONATION PHENOMENA AND CORROSION BEHAVIOR OF STAINLESS STEEL BAR IN THE MORTAR MIXED WITH SEAWATER

Student Number: 09-17052 Name: Tomohiro Nagata Supervisor: Nobuaki Otsuki

1 Introduction

Worldwide shortage of freshwater is expected in the future, and perspective for the availability of concrete mixed with seawater is required.

The most dangerous factor for concrete mixed with seawater is corrosion of reinforcing bars. Especially in land environment reinforcing bars are under the danger of carbonation phenomena.

Carbonation decreases the pH of concrete, moreover it is reported that internal chloride ion from seawater is concentrated to the inner by carbonation phenomena [1]. Therefore, reinforcing bars in the carbonated concrete mixed with seawater are exposed to a severe environment with low pH and large amount of chloride ion.

To overcome this problem, the usage of stainless steel as reinforcing bar is commonly practiced. However the corrosion behavior of stainless steel reinforcing bars in carbonated concrete mixed with seawater is not investigated enough.

Thus, the objectives of this study are set below,

(1)To evaluate the effect of seawater on carbonation phenomena from carbonation rate of mortar mixed with seawater.

(2)To clarify chloride ion concentration in the carbonated mortar mixed with seawater from micro analysis

(3)To clarify corrosion behavior of stainless steel reinforcing bars in mortar mixed with seawater under carbonation from electro chemical measurement.

(4)To suggest the proper combination for concrete mixed with seawater under carbonation.

2 Experiment procedures

2.1 Materials

The materials used in this study were two types of cement, three types of bar, and two types of mixing water. Two types of cement were Portland blast -furnace cement class B (BB) and Ordinary Portland Cement (OPC) Three types of bar were two types of stainless steel bars (SUS304SD and SUS410SD) and plain bar (SD295A). SUS410SD has smaller content of Chromium (Cr) ratio than SUS304SD. Table 1 shows the chemical properties of bars. Two types of mixing water, freshwater and artificial seawater (ASTM-D-1141-98(2003)) were used. As fine aggregate land sand (fineness modulus:2.52 density in saturated surface-dry condition:2.61g/cm^3 water absorption:1.88) was used.

Table 1 Chemical properties of bars (mass%)

	Fe	C	Si	Mn	P	S	Ni	Cr
SD295A	98.33	0.2	0.24	0.74	0.22	0.27	-	-
SUS410SD	86.7	0.01	0.28	0.34	0.2	0.02	0.18	12.57
SUS304SD	71.4	0.06	0.38	1.48	0.32	0.21	8.14	18.32

Table 2 Mix proportions of mortar

Type of Cement	W/C	Unit weight(Kg/m^3)				
		W	OPC	BFS	Gypsum	Sand
OPC	50 %	316	632	0	0	1264
BB		315	378	247	5	1259

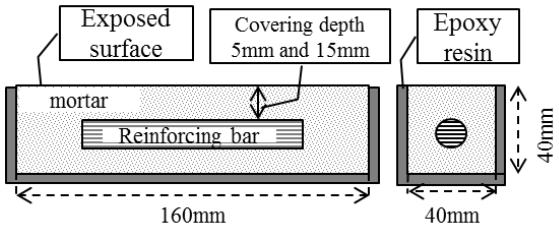

Fig.1 Schematic of specimen

2.2 Specimen

The size of mortar specimens was 40×40×160mm and the types of covering depth of specimens were 5mm and 15mm, as shown in Fig.1. The specimens were cured for the span defined by concrete standard specifications (OPC:5days-curing、BB:7days-curing) , and for only 1day (1day-curing). Table 2 shows the mix properties of mortar. After curing, sides of specimens are sealed with epoxy resin (Fig.1). After that they are exposed to carbonation chamber (the density of CO_2:5% humidity: 60%).

2.3 Measurement items and method

(1)Carbonation rate was evaluated by measuring periodically carbonation depth of specimen, using phenolphthalein method (JIS-A-1152). Based on that, the carbonation rate coefficient was derived from $\sqrt{t}$ method.

(2)To clarify concentration of chloride ion by carbonation phenomena, micro analyses were conducted on the section of mortar specimen by EPMA method.

(3)To clarify corrosion behavior of stainless steel bars, the corrosion current density of specimen were measured periodically. Moreover the relationship between corrosion current density and carbonation rate was evaluated.

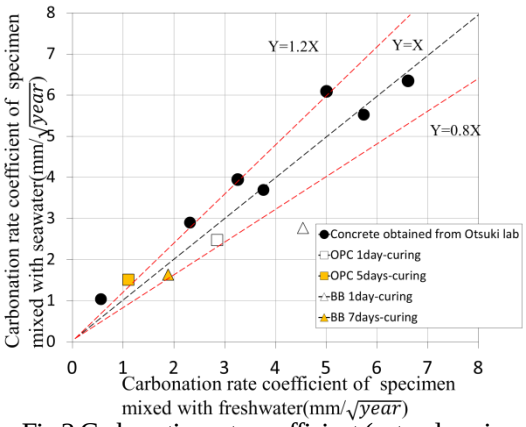

Fig.2 Carbonation rate coefficient (natural environment)

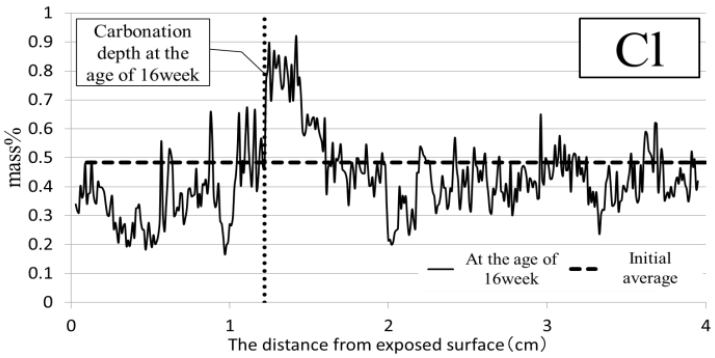

Fig.3 The distribution map of chloride ion of BB (1day-curing)

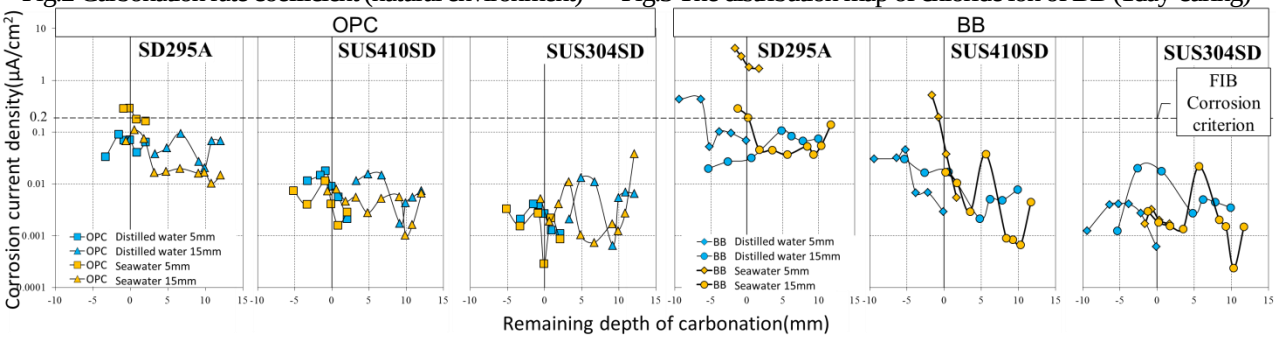

Fig.4 The relationship between remaining depth of carbonation and corrosion current density

3 Experimental results

3.1Carbonation phenomena

Fig.2 shows the carbonation rate coefficient of each specimen and data obtained by Otsuki laboratory [2]. Carbonation rate coefficients were converted into natural environment (the density of CO_2:0.0315%) by Uomoto formula [3]

From this figure and within the scope of this study carbonation rate of mortar mixed with seawater was almost same as that mixed with freshwater.

Besides, Fig.3 shows the chloride ion distribution map of BB (1day-curing) mixed with seawater at the age of 16weeks. From this figure it is confirmed that chloride ion is concentrated into the inner part due to carbonation phenomena.

3.2 Corrosion behavior of stainless steel bars

Fig.4 shows the relationship between remaining depth of carbonation and corrosion current density of each specimen. Remaining depth of carbonation is the difference between carbonation depth and covering depth.

From this figure, in the case of stainless steel bars, corrosion current density of SUS304SD was maintained at low level regardless of type of cement. However, in the case of SUS410SD, before the carbonation reached the covering depth the corrosion current density was maintained at low level, but after the carbonation reached the covering depth, corrosion current density of BB mixed with seawater reached 0.2μA/cm^2(corrosion criterion of FIB).

On the other hand, corrosion current density of SD295A increased as carbonation progresses, regardless of type of cement. When carbonation reaches the covering depth, current density of SD295A in mortar mixed with seawater increased and reached 0.2μA/cm^2.

4 Conclusions

(1)Carbonation coefficient of specimen mixed with seawater was almost same as that mixed with freshwater.

(2)Chloride ion is concentrated to the inner by carbonation phenomena in the case of mortar mixed with seawater.

(3)When mortar mixed with seawater is carbonated, stainless steel bars isn't corroded except for SUS410SD embedded in Portland blast -furnace cement class B.

(4)The combination of SUS304SD and any cement, and the combination of SUS410SD and Ordinary Portland Cement may be proper for concrete mixed with seawater under carbonation.

References

[1] Koichi Kishitani etc, The Relationship between Rebar Corrosion and Neutralization in the Concrete Containing Chloride, Proceedings of annual conference of JCI,Vol.13、No.1. pp.601-2, 1991

[2] Takahiro Nishida etc, Resistance to transfer of materials in the case of concrete mixed with seawater, Proceedings of annual conference of JCI, 2013 (under reviewing)

[3] Kento Uomoto etc, Influence of Concentration Carbon Dioxide on Carbonation Ratio of Concrete, production study, Vol.43, pp.35-38, 1991

Image Compression by using Vector Quantization and Vector-Embedded Karhunen-Loève Transform

Students Number: 09_18761 Name: Kiung Park Supervisor: Yukihiko Yamasita

I Introduction

JPEG is an international standard for still image compression. Even if it has problems such as blocking distortion and image quality degradation in edge region, it has been used widely because its algorithm is simple and fast, and the compression ratio is high.

Quantization used in JPEG is scalar quantization (SQ). Shannon's rate-distortion theory indicates that a better performance can be achieved by coding vectors instead of scalars [1], [2]. Thus, if we introduce vector quantization (VQ) into JPEG, we can expect better compression performance. However, current image coding methods by VQ have a problem that the size of representative vectors is small. It degrades coding efficiency.

This paper proposes a new image copmression scheme by coding the difference between input vector and its representative vetor to overcome the problem. VEKLT (Vector-Embedded Karhunen-Loève Transform) [3] is used as the transformation instead of DCT to introduce statistically adaptive transformation.

The rest of this paper is organized as follows. In Section 2, we will give an overview of the proposed image compression scheme. Some key techniques of the proposed scheme are presented in Sections 3 and 4. The experimental results demonstrate the advantages of the proposed scheme in Setion 5. Finally, Setion 6 concludes this paper.

II Overview of Proposed Method

The proposed image compression scheme is illustrated in Fig. 1. The proposed encoder is based on JPEG and the decoder is nearly the same as the inverse of encoder.

The proposed process is the same as that of JPEG until "Subtract 128 from each pixel". At first, DC coefficients of input blocks are obtained by inner product with the first DCT basis. And then, the block is normalized and the index of the nearest representative vector is selected from dataset by using recognizer based on MSE. After obtaining difference data from the representative vector, VEKLT is performed by using the covariance matrix. Next, they are coded by arithmetic coder. Actually, Huffman coder is used in JPEG, but the code book isn't optimized in proposed scheme. Thus, I use arithmetic coder into all of transformed data for fair comparison. After comparing the code-length of AC coefficients from DCT and the sum of code-lengths of AC coefficients from VEKLT and VQ coefficient and index, the shorter one is selected. If DCT is selected, its index is changed to 0 and its VQ coefficient is deleted. Finally the coder outputs data structure which consists of DC coefficients and revised indexes and VQ coefficients and seleted AC coefficients.

III Representative Vectors and Corresponding Covariance Matrixes

A. Representative Vectors

At first, normalized input vectors are obtained by using the same method in Fig. 1 from prepared 160 training images (512×512).GMM (Gaussian Mixture Model) which is a clustering method is implemented. The initial mean vectors are decided by k-means. Because the mean vector has the highest probability in each cluster, it appears very often in images. Thus, I sample it from training images. In my research, I sample 400 mean vectors from every training image. Then, 64000 candidates are obtained for representative dataset. Finally, I choose 100 vectors from the candidates by k-means and normalize them again. The last 100 normalized vectors are used as the representative vectors for VQ.

B. Covariance Matrixes for VEKLT

Because VEKLT is a kind of KLT, a covariance matrix is needed for making a transformation matrix. In my research, the covariance matrix is made by the difference vectors that have a same index. Then, if the number of representative vectors is 100, I have to prepare 100 covariance matrixes. Therefore, I made 100 covariance matrixes from 160 training images used for making VQ dataset.

IV Implementation of VEKLT

Let f_i be the i-th block of image **f**, it can be written as

$$f_i =< f_i, \Phi_{DC} > \Phi_{DC} + < f_i, \Phi_{i,AC} > \Phi_{i,AC}.$$

By normalizing f_i, $\Phi_{i,AC}$ is obtained. And then, the nearest vector $\hat{\Phi}_{i,VQ}$ to $\Phi_{i,AC}$ is selected from VQ dataset by using recognizer. In case of 8×8 block size, the dimension of f_i is 64. Because Φ_{DC} and $\hat{\Phi}_{i,VQ}$ are perpendicular, f_i can be expanded as

$$\begin{aligned} f_i &= < f_i, \Phi_{DC} > \Phi_{DC} + < f_i, \hat{\Phi}_{i,VQ} > \hat{\Phi}_{i,VQ} \\ &+ \sum_{j=1}^{62} < f_i, \Phi_{ij} > \Phi_{ij}. \end{aligned}$$

where Φ_{ij} is perpendicular to Φ_{DC} and $\hat{\Phi}_{i,VQ}$.

The remaining basis Φ_{ij} is obtained by VEKLT. Let $\mathbf{R}_\mathrm{i}$ be the covariance matrix of f_i and $\mathbf{W} = \Phi_{DC}\Phi_{DC}^\mathrm{T} + \hat{\Phi}_{i,VQ}\hat{\Phi}_{i,VQ}^\mathrm{T}$, the symmetric matrix $\mathbf{Q}_\mathrm{i}$ is defined by

$$\mathbf{Q}_\mathrm{i} = \mathbf{R}_\mathrm{i} - \mathbf{R}_\mathrm{i}\mathbf{W} - \mathbf{W}\mathbf{R}_\mathrm{i} + \mathbf{W}\mathbf{R}_\mathrm{i}\mathbf{W}.$$

Φ_{ij} $(j = 1, \ldots, 62)$ is given by eigenvectors of $\mathbf{Q}_\mathrm{i}$ corresponding nonzero eigenvalues. The transformation matrix

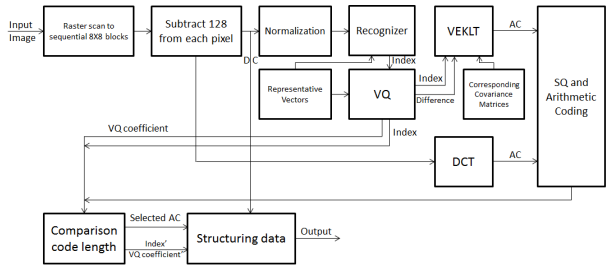

Fig. 1. The proposed encoder

$\mathbf{T}_{\mathrm{i}}$ is given by

$$\mathbf{T}_{\mathrm{i}} = [\Phi_{\mathrm{i}1}, \ldots, \Phi_{\mathrm{i}62}]^{\mathrm{T}}$$

After transforming f_i as $\mathbf{T}_{\mathrm{i}} f_i$, the coefficients $< f_i, \Phi_{ij} >$ are obtained.

V Experimental Results

A. Rate-Distortion Relation

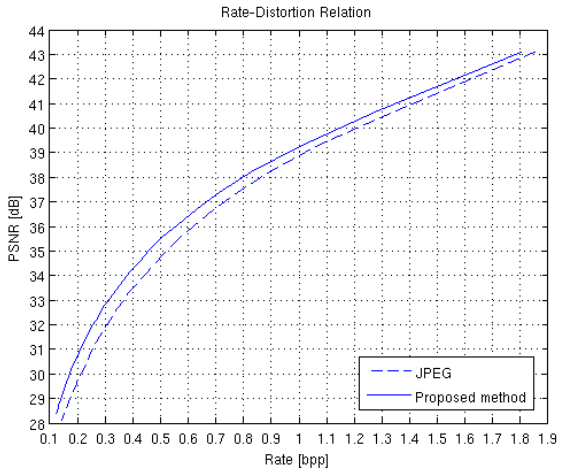

Fig. 2. Rate-distortion curve (Lena)

I used a standard image Lena (512×512) to demonstrate the performance of the proposed scheme. Fig. 2 and TABLE. I show the rate-distortion relation. In all of bpp (bits per pixel) range, the proposed scheme outperforms JPEG 0.2∼1.0dB in PSNR (Peak Signal-to-Noise Ratio). Especially, when bpp is low, it outperforms JPEG clearly.

TABLE I

Lena		
bpp	PSNR in dB	
	Proposed Scheme	JPEG
0.24	**31.69**	30.67
0.50	**35.47**	34.73
1.00	**39.27**	38.90

B. Visual Quality

Images in Fig. 3 and Fig. 4 are reconstructed respectively by JPEG and the proposed scheme. We can see the visual quality of the proposed scheme is better than JPEG.

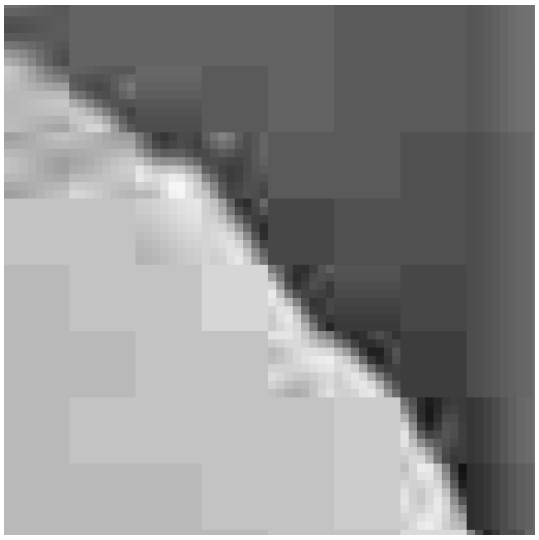

Fig. 3. Cropped Lena reconstructed by JPEG (bpp : 0.24)

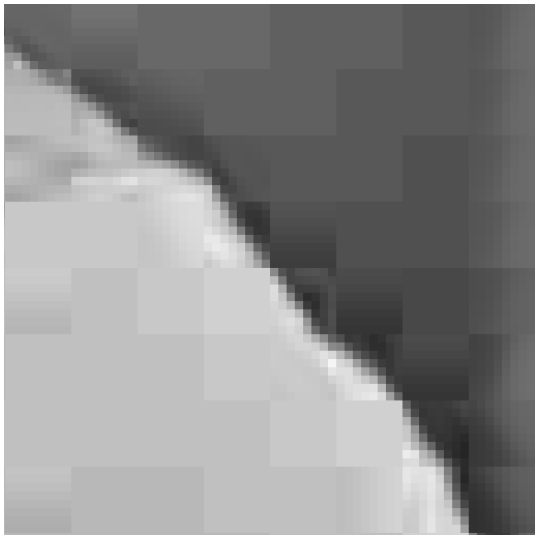

Fig. 4. Cropped Lena reconstructed by proposed scheme (bpp : 0.24)

VI Conclusion

This paper proposes a new image compression scheme by using VQ and VEKLT. Experimental results fully demonstrate the advantages of the proposed techniques. Its PSNR outperforms JPEG 0.2∼1.0dB and its visual quality in edge region is better than JPEG especially at low bpp.

However, there are still many aspects to be investigated in the future, such as indexing method, approximation of real covariance matrix, number of representative vectors, their mining method, coding for transformed blocks by VEKLT, and so on.

References

[1] C. E. Shannon *A mathematical theory of communication*, Bell System Tech. Journal, vol. 27, pp. 379-423, 623-656, 1948.

[2] Feng Wu, Xiaoyan Sun *Image Compression by Visual Pattern Vector Quantization(VPVQ)*, IEEE Data Compression Conference, pp. 123-131, 2008.

[3] Toshihisa TANAKA, Yukihiko YAMASHITA *Vector-Embedded KLT and Its Application in Orientation Adaptive Coding of Images*, IEICE TRANS. FUNDAMENTALS, vol. E38-A, No.6 2000

Development of Millimeter-wave Radio Channel Sounder

Student Number: 09B20284 Name: Pham Kinh Hung Supervisor: Jun-ichi Takada, Minseok Kim

1 Introduction

Millimeter-wave with 1 mm to 10 mm wavelength and 30 GHz to 300 GHz frequency range is an alternative frequency bands to be applied in high speed wireless communication systems. In this study, a millimeter-wave channel sounder has been developed to investigate the propagation characteristics at 60 GHz bands. Because of using low cost off-the-shelf RF transceiver, the measurement accuracy is affected by many error factors, mainly phase noise and IQ Imbalance. This study discussed about the design of the sounding signal and compensation requirement for an accurate measurement by investigating the effect of phase noise and I/Q imbalance in the numerical simulation.

2 Developed hardware

Millimeter-wave channel sounder consists of transmitter, receiver and local oscillator which supply signal to synthesize transmit signal and carrier signal. Each transmitter consists of baseband (BB) circuit and radio frequency (RF) circuit. Fig.1 is the millimeter-wave channel sounder used in the experiment. Channel sounder is used to estimate the transfer function $H(f)$ between the transmitter and the receiver. The relation of $H(f)$ with Fourier transforms of transmit signal $X(f)$, receive signal $Y(f)$ and white noise $N(f)$ is represented as:

$$Y(f) = H(f)X(f) + N(f), \quad (1)$$

In practice, as shown in Fig.2, multiplicative error factors such as the phase noise ($\phi_t(t)$, $\phi_r(t)$) and I/Q imbalance (ε, θ) degrade the measurement accuracy. Since we can measure $X(f)$, $Y(f)$ and $N(f)$, estimating $H(f)$ accurately requires us to define the influence of phase noise and IQ imbalance, then find the way to calibrate or reduce the influence.

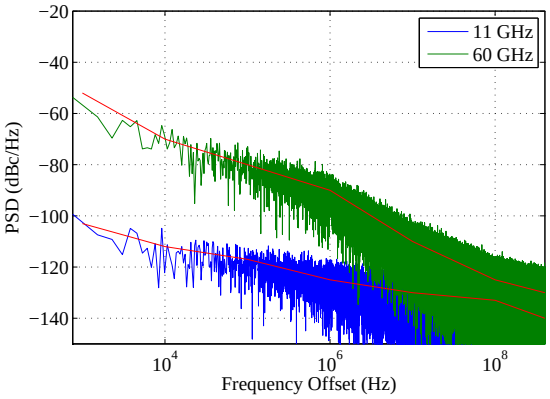

Figure 3: Spectrum of Phase Noise

3 Phase Noise Influence and Channel Sounding Method

Phase noise is the frequency fluctuations of the local oscillators at the transceiver. In the frequency domain, a pure sine wave would be represented as a delta function. However, all oscillators, that generate carrier signal in RF circuit, have phase modulated noise components. The phase noise components spread the power of signal to adjacent frequencies, resulting in noise sidebands, thus causing interference between sub-frequencies. To reduce influence of phase noise to measurement result, we have to choose appropriate sounding method.

In previous research, we have already developed channel sounder at 11 GHz. In 11 GHz system, the phase noise power is small, so it almost does not affect to the system [1]. The transmit signal is multi-tone which consists of 2048 single-tones arranged on

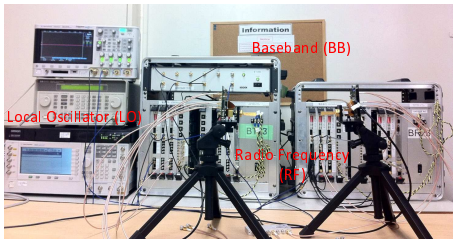

Figure 1: Millimeter-wave Channel Sounder

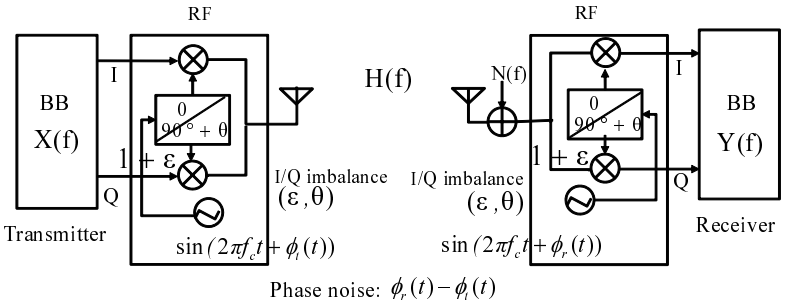

Figure 2: Channel Sounder Model

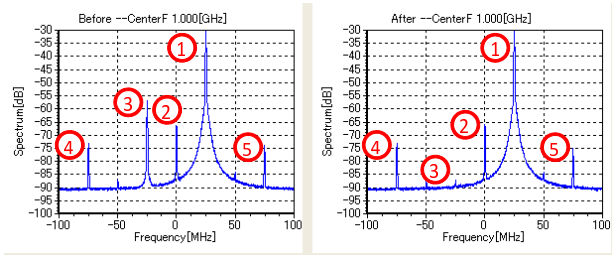

Figure 4: IQ Imbalance Compensation Result

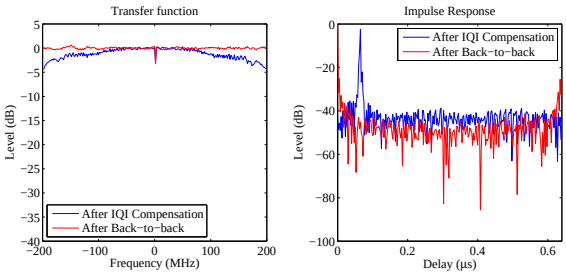

Figure 5: The Transfer Function and Impulse Response after Calibration

bandwidth of 400 MHz. However, in millimeter-wave sounder, the phase noise power becomes stronger. It is needed to increase the interval among tones (Δ_f), so that the number of tones on the whole bandwidth will decrease because of the fixed bandwidth. On the other hand, the measurement time delay calculated as the time signal transmit from transmitter to receiver, should be smaller than the length of symbol ($1/\Delta_f$) to avoid interference among other channels. From those conditions, the number of tones is decided as 256 tones. Fig.3 shows the comparison of spectrum of phase noise between 11 GHz and millimeter-wave channel sounder (at 60 GHz).

4 IQ Compensation

As can be seen Fig.2, IQ imbalance is caused by a slight discrepancy between the in-phase and quadrature components in the quadrature modulator. In this IQ imbalance model, ε, and θ denote the amplitude difference and the phase offset of the quadrature oscillator branches, respectively. Meanwhile, $\mathbf{E}$ represents the error matrix of ε and θ. We also denote $\mathbf{w}(t)$ and $\mathbf{x}(t)$ as the carrier signal and baseband signal, respectively. The distorted output signal can be calculated as:

$$\begin{aligned} \tilde{z}(t) &= (\mathbf{E}\mathbf{w}(t))^T\mathbf{x}(t) \\ &= z(t) + z_{ei}(t), \end{aligned} \quad (2)$$

where $z(t)$, $z_{ei}(t)$ are the ideal output and the image distortion components respectively. In the equation (2), if the baseband signal is distorted as

$$\mathbf{x}'(t) = (\mathbf{E}^{-T}\mathbf{x}(t)), \quad (3)$$

the output signal can be generated ideally. That means when we know the error parameters in model, we can easily eliminate IQ imbalance using digital pre-distortion on the original input signal. By using the spectrum analyzer, we can measure the power spectrum of image distortion which can be use to estimate the error parameters for taking a compensation. The detailed algorithm can be seen in [3].

In this compensation method, the model parameters are optimized to suppress the values of L_{IRR}, that denotes the image power reduction ratio (IRR).

$$L_{\mathrm{IRR}} = \frac{E[\mathbf{z}_{ei}(t)]}{E[\mathbf{z}(t)]} = \frac{(\varepsilon^2+\varepsilon+2) - 2(1+\varepsilon)\ cos\ \theta}{4}, \quad (4)$$

NMSE (Normalized Mean Square Value) is used to evaluate the effect of IQ imbalance From (4), it can be derived that NMSE corresponds to L_{IRR}.

Fig.4 shows the result of IQ imbalance compensation in millimeter-wave channel sounder. In this figure, from (1) to (5) are fundamental component, carrier leakage, image distortion, image of third harmonic and second harmonic component. By comparing left side and right side, we can see the image distortion has already reduced, and L_{IRR} becomes greater than 60 dB, thus the NMSE is less than 10^{-6}. Since millimeter-wave radio frequency circuit does not allow direct current to pass through, carrier leakage can not be compensated. Similarly, the second harmonic component and image of third harmonic component also can not be compensated, but they are small enough compared to the fundamental component.

After compensating for both transmitter and receiver, we connect them directly to estimate the instrument characteristic, then eliminate it to obtain the unknown channel characteristic. The result is shown in the Fig.5.

5 Conclusion

This research proposed an appropriate channel sounding method for millimeter-wave channel sounder and a calibration method to increase accuracy of measurement result.

As future works, we plan to design 4×4 MIMO millimeter-wave channel sounder to measure propagation characteristic of the millimeter-wave.

References

[1] M. Kim, J. Takada, Y. Konishi, "Novel Scalable MIMO Channel Sounding Technique and Measurement Accuracy Evaluation with Transceiver Impairments," IEEE Trans. Instrum. Meas., Vol.61, No. 12, pp. 3185-3197, Dec. 2012

[2] M.Ghoraishi, M.Kim, J.Takada, "Influence of phase noise on the frequency division multiplexing channel sounding," 2010 Asia Pacific Microwave Conference, Yokohama, Japan, Dec. 2010

[3]M. Kim, Y. Konishi, J. Takada, B.Gao, " I/Q Imbalance Compensation Technique for Quadrature Modulation by Single-Tone Testing," submitted to IEICE Trans.Commun.

Identification of riboflavin producing yeast in the fermentation process for Puer tea

Student Number: 09-21088 Name: Ryutaro BESSHO Supervisor: Kiyohiko NAKASAKI

1 Introduction

Puer tea is a unique fermented tea manufactured in the Yunnan province of China. It has been consumed by Chinese people for centuries, and has recently become popular in Japan as well, as a functional beverage [1]. Pure tea is produced from green tea as raw material by the act of microorganisms whereas black tea or oolong tea is produced by the act of enzymes contained in the tea leaves themselves. It is known that in general, Puer tea contain higher concentration of riboflavin, a kind of vitamin B_2 compared to the green tea, which indicates that riboflavin in the leaves was enriched by the act of microorganisms during the fermentation. The objectives of this study were the identification and the isolation of a microorganism that has the ability to produce riboflavin using the tea leaves as substrate.

2 Materials and methods

2-1 Puer tea samples and process characterization

Tea leaf samples under the fermentation process were obtained from a company at Fuken in China. At the factory, harvested tea leaves were heat-treated to inactivate the indigenous enzymes in the tea leaves. Then, the leaves were softened by mixing, and dried under sunlight. To promote the microbial activity at the start of fermentation, water was added to the leaves. Then the leaves were piled in a windrow shape in the fermentation room. During the fermentation, leaves were turned over roughly once a week to ensure the homogeneity of the tea leaves.

Temperature of the leaves was measured at the center of the pile. Tea leaf samples were collected from the piles on days 0, 1, 14, 21, 35, and 50 of the fermentation process and were subjected to the measurements of pH, water content and riboflavin concentration, and to the microbial analyses.

2-2 Determination of riboflavin concentration in the Puer tea samples

A 1-gram of leaf sample was homogenized in 9 mL of distilled water. Extraction conditions were the same as described by Capozzi et al [2].

2-3 Microbial community analysis of Puer tea samples

The microbial community in the leaf samples was determined by denaturing gradient gel electrophoresis (DGGE) analysis [3]. In the DGGE analysis, fungal 26S rRNA gene fragment was used. Characteristic bands in the DGGE gel were excised and base sequences of the DNA contained in the bands were determined.

2-4 Isolation of a yeast strain

A 3-gram of leaf sample was homogenized in 27mL of distilled water and was diluted appropriately. The diluted solutions were spread onto rose-bengal agar medium and were cultivated at 30°C for 2 d. After that, the colonies appeared on the plates were picked up and streaked several times in order to purify the isolated yeast.

2-5 Real-time PCR

The cell density of strain YPT2 in the Puer tea samples was measured by real-time PCR method using the DNA extracted from the Puer tea samples as a template. The primers specific to strain YPT2, Y2RTf, 5′-CGAGAGGTGTGAAAGGTACAC-3’, and Y2RTr, 5′-GATGGCTGTTGCTATATCCCC-3’ were designed and used. The real-time PCR was performed using Smart Cycler® II system (Cepheid, California, USA) and SYBR® premix *EX Taq*™ (TaKaRa Biomedicals, Shiga, Japan).

2-6 Pure cultivation of the strain YPT2 on the tea leaves

Chinese green tea leaves sterilized by 1 Mrad/h of Co-60 gamma ray irradiation for 3 h were placed in a 500 mL Erlenmeyer flask and the water content of the leaves was adjusted to around 30 % by adding sterilized distilled water. Strain YPT2 was cultivated for 2 d in potato dextrose medium beforehand and was inoculated to the leaves so that the initial cell density of strain YPT2 was about 6 log CFU/g-ds. Cultivation was performed at 30 °C for 5 days with the air flow rate of 3 mL/min. The samples were collected daily and were subjected to the measurements of water content, pH, cell density of the strain YPT2 and riboflavin concentration. The cell density of strain YPT2 was measured by dilution plating method.

3 Results and discussion

3-1 Characterization of the fermentation process

The courses of temperature, pH and water content are shown in Fig. 1. Gradual increase in temperature by the heat of microbial activity and instant decrease in temperature due to the turning over of the pile took place alternately during the fermentation. The pH value of the starting material was 5.5 and fell slightly to 4.3 by day 14. After that the pH value gradually increased and finally attained at around 5.8. The water content of the raw material was as low as 10% at the beginning of the

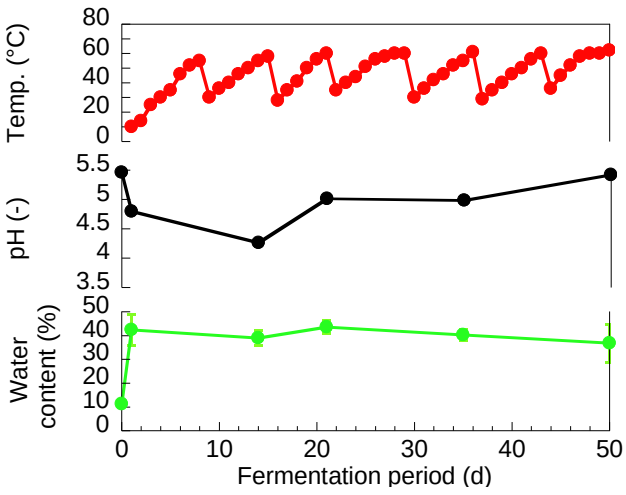

Fig. 1 The course of temperature, pH and water content in Puer tea pile at the tea processing factory in China

process and increased to around 40% on day 1 by the addition of water, then, it maintained around 40% during the fermentation.

3-2 Concentration of riboflavin in Puer tea samples

The course of riboflavin concentration in the Puer tea samples is shown in Fig. 2. The initial riboflavin concentration was 2 μg/g-ds, and it increased to 10 μg/g-ds until the end of fermentation. Since enzymes contained in the leaves were inactivated by heat-treatment, it is considered that the riboflavin was produced by the microorganisms in the leaves.

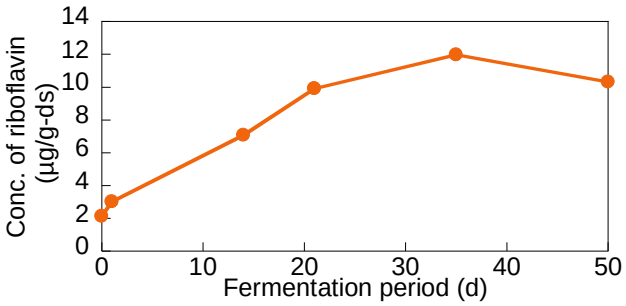

Fig. 2 The course of riboflavin concentration in Puer tea samples

3-3 PCR-DGGE analysis

DGGE image obtained from amplification of the 26S rRNA gene fragment derived from the tea leaves is shown in Fig. 3. There were five distinct bands, band a, b, c, d and e which appeared consistently for certain periods during the fermentation. Among the 5 distinct bands, band a was not reproducible when the tea leaf samples obtained from another fermentation piles were subjected to the PCR-DGGE analysis. Therefore, the other 4 bands except the band a were excised from the DGGE gel and DNA sequences were determined. The nucleotide blast of these sequences indicated the closely related species for the fungi corresponding to those bands as follows, band b: *Blastobotrys adeninivorans*, band c: *Debaryomyces hansenii* var. *fabryi*, band d: *Aspergillus* sp., band e: *Talaromyces* sp. Among those 4 kinds of fungal species, *Debaryomyces hansenii* corresponding to the band c is famous for the high riboflavin producing ability and it was deduced that the fungal strain corresponding to the band c produced riboflavin during the Puer tea fermentation. In the attempts to isolate the fungi corresponding to the distinct bands appeared in the DGGE gel, strain YPT2 was isolated. When the strain YPT2 was subjected to PCR-DGGE analysis, the band was observed at positions identical to that of the band c (Fig. 3).

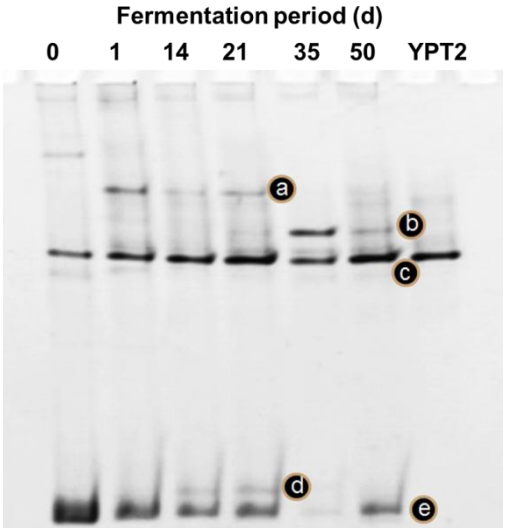

Fig. 3 PCR-DGGE fingerprint for the Puer tea samples

3-4 Concentration of strain YPT2 in Puer tea samples

The course of cell density of strain YPT2 in the Puer tea samples determined by real-time PCR method is shown in Fig. 4. The initial concentration of strain YPT2 was 6.4 log CFU/g-ds. As early as day 1 of fermentation, 8.1 log CFU/g-ds of strain YPT2 appeared. Then, the cell density decreased gradually until the end of fermentation and finally, it reached 5.6 log CFU/g-ds. The cell density of YPT2 kept high at around 8.0 log CFU/g-ds from day 1 to 21 and during the same period of fermentation, the increase in the concentration of riboflavin was observed, suggesting that the strain YPT2 have contributed to the riboflavin production during the Puer tea fermentation.

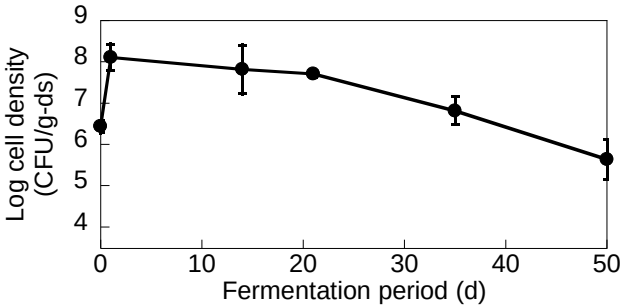

Fig. 4 The course of cell density of strain YPT2 in Puer tea samples

3-5 Pure cultivation of strain YPT2 on Puer tea leaves

Riboflavin producing ability of strain YPT2 was verified by pure cultivation on green tea leaves that were the raw materials of Puer tea. As was not shown here, the increase in the riboflavin concentration was observed in the raw materials along with the growth of strain YPT2.

4 Conclusions

It was confirmed that riboflavin concentration in Puer tea leaves increased during the Puer tea fermentation and strain YPT2, the genus of which was famous for riboflavin production was isolated and identified. It was also verified that riboflavin concentration in Puer tea leaves increased when cell density of strain YPT2 was high and that strain YPT2 had the ability to produce riboflavin in the cultivation using the green tea leaves as substrate.

References

[1] Sano, M., et al.: Effects of Pu-erh tea on lipid metabolism in rats, Chem. Pharm. Bull., **34**, 221-228, (1986)

[2] Capozzi, V., et al.: Biotechnological Production of Vitamin B2-enriched Bread and Pasta, J. Agric. Food Chem., **59**, 8013-8020, (2011)

[3] Abe, M., et al.: Characteristic fungi observed in the fermentation process for Puer tea, Int. J. Food Microbiol., **124**, 199-203, (2008)

大域的射影変換を用いたパターンマッチングに関する研究

学籍番号：09_23408　学生氏名：苗春亭　指導教員：山下幸彦

1　はじめに

光学的文字読取装置 (OCR) は，スキャナなどによって入力した画像の文字をコンピュータによって認識する装置である。近年では，その認識は統計的処理によって行うものが多い。しかしながら，そのためには学習の際に多数の文字データが必要となる。そのような多数の文字データが得られない場合に対して，パターンマッチングによって文字を認識する手法が提案されている。一般に認識対象となる文字 (入力文字) は，学習した文字 (学習文字) と全く同じではなく，各種の変形を受けている。アフィン変換は，2 次元座標の線形変換と平行移動からなる変換である。画像全体に対するアフィン変換に対して頑健な，入力文字と学習文字の相関値の算出法である，大局的アフィン変換 (GAT) 相関法 [1,2,3] が提案され，パターンマッチングによる文字認識手法としては，高い認識率を実現している。

アフィン変換を拡張したものに，射影変換がある。射影変換は，3 次元空間の平面を別の平面に透視して得られる変換である。本論文では，GAT 相関法において頑健となるアフィン変換を射影変換に拡張した，大域的射影変換 (GPT) 相関法を提案する。そして，GPT 相関法の具体的アルゴリズムを示し，計算機実験によってその有効性を確認する。

2　GAT 相関法

2 次元座標を表す 2 次元ベクトルを $\boldsymbol{x}$ とおき，アフィン変換したベクトルを $\boldsymbol{x}'$ とおけば，

$$\boldsymbol{x}' = \boldsymbol{A}\boldsymbol{x} + \boldsymbol{b} \tag{1}$$

が成立する。ここで，$\boldsymbol{A}$ と $\boldsymbol{b}$ はアフィン変換を表す $(2,2)$-行列と 2 次元ベクトルである。定義域が D である画像 $f(\boldsymbol{x})$ を，式 (1) のアフィン変換で変換した画像を $f_A(\boldsymbol{x})$ とおけば，

$$f_A(x) = \frac{1}{|\boldsymbol{A}|} f(\boldsymbol{A}^{-1}(\boldsymbol{x} - \boldsymbol{b})) \tag{2}$$

が成立する。2 つの画像 $f(\boldsymbol{x})$ と $g(\boldsymbol{x})$ の GAT 相関値は，様々なアフィン変換に対する

$$\int_D f_A(\boldsymbol{x}) g(\boldsymbol{x}) d\boldsymbol{x} \tag{3}$$

の最大値として定義される。

式 (3) の最大化を直接計算することは難しいため，若原らは次に示す解法を提案した [1,2,3]。まず，2 次元ガウス関数 $G(\boldsymbol{x})$

$$G(\mathbf{x}) = \sqrt{\gamma} e^{-\gamma \|\boldsymbol{x}\|^2} \tag{4}$$

を定義する。そして，式 (3) を，

$$\int_D \int_D G(A\boldsymbol{x}_1 + \boldsymbol{b} - \boldsymbol{x}_2) f(\boldsymbol{x}) g(\boldsymbol{x}) d\boldsymbol{x}_1 d\boldsymbol{x}_2 \tag{5}$$

で近似する。この式は，ガウス関数でぼかした画像の相関を意味している。この近似により，未知成分 $\boldsymbol{A}$, $\boldsymbol{b}$ が画像の中ではなく，ガウス関数の中に含まれるようになり，微分などが容易に計算できるようになった。さらに，エッジ方向の同一性を導入し，

$$\begin{aligned} J_{GAT} \quad = \quad & \int_D \int_D G(A\boldsymbol{x}_1 + \boldsymbol{b} - \boldsymbol{x}_2) \\ & \delta(\nabla f(\boldsymbol{x}_1), \nabla g(\boldsymbol{x}_2)) f(\boldsymbol{x}) g(\boldsymbol{x}) d\boldsymbol{x}_1 d\boldsymbol{x}_2 \end{aligned}$$

を定義し，この最大値を GAT 相関値としている。ここで，$\delta(\nabla f(\boldsymbol{x}_1), \nabla g(\boldsymbol{x}_2))$ は，2 つの画像のエッジ方向が等しいときに 1，それ以外のときは 0 とする関数である。$\boldsymbol{x}_1$, $\boldsymbol{x}_2$ の関数 (行列またはベクトルの場合もある) $h(\boldsymbol{x}_1, \boldsymbol{x}_2)$ に対して，式 (6) の被積分関数による期待値を

$$\begin{aligned} \overline{h(\boldsymbol{x}_1, \boldsymbol{x}_2)} \quad \equiv \quad & \int_D \int_D h(\boldsymbol{x}_1, \boldsymbol{x}_2) G(A\boldsymbol{x}_1 + \boldsymbol{b} - \boldsymbol{x}_2) \\ & \delta(\nabla f(\boldsymbol{x}_1), \nabla g(\boldsymbol{x}_2)) f(\boldsymbol{x}) g(\boldsymbol{x}) d\boldsymbol{x}_1 d\boldsymbol{x}_2 \end{aligned}$$

で定義する。

GAT 相関法では，$\boldsymbol{A}$ と $\boldsymbol{b}$ に対する J_{GAT} の微分を 0 として最大値を求める。このとき，得られた式のガウス関数 $G(\boldsymbol{x})$ の中では，$\boldsymbol{A} = \boldsymbol{O}$, $\boldsymbol{b} = \mathbf{0}$ という第 0 近似を使って，$\boldsymbol{A}$ と $\boldsymbol{b}$ に対する線形方程式を求めて，次式により $\boldsymbol{A}$ と $\boldsymbol{b}$ を求めている。

$$\begin{aligned} \boldsymbol{A} \quad &= \quad \left(\overline{\boldsymbol{x}_2 \boldsymbol{x}_1^T} - \frac{\overline{\boldsymbol{x}_2}\,\overline{\boldsymbol{x}_1}^T}{\overline{1}} \right) \left(\overline{\boldsymbol{x}_1 \boldsymbol{x}_1^T} - \frac{\overline{\boldsymbol{x}_1}\,\overline{\boldsymbol{x}_1}^T}{\overline{1}} \right)^{-1} \\ \boldsymbol{b} \quad &= \quad -\frac{A\overline{\boldsymbol{x}_1}}{\overline{1}} + \frac{\overline{\boldsymbol{x}_2}}{\overline{1}} \end{aligned} \tag{6}$$

ガウス関数に近似を適用したため，一般には式 (6) の解は真の最大点を与えない。従って，そのアフィン変換で画像を変換し，式 (6) を再計算する。この操作を繰り返し，相関値が収束した時に，その相関値を GAT 相関値として出力する。

3 GPT 相関法

2 次元ベクトルを $\boldsymbol{x}$ に対して，射影変換したベクトルを $\boldsymbol{x}'$ とおけば，次式が成立する。

$$\boldsymbol{x}' = (\boldsymbol{A}\boldsymbol{x} + \boldsymbol{b})/(1 + \langle \boldsymbol{c}, \boldsymbol{x} \rangle) \tag{7}$$

上式で、$\boldsymbol{c} = \boldsymbol{0}$ とすれば，式 (7) は，アフィン変換を表す。ここで，部分射影変換 (PPT) を，

$$\boldsymbol{x}' = \boldsymbol{x}/(1 + \langle \boldsymbol{c}, \boldsymbol{x} \rangle) \tag{8}$$

で定義する。射影変換はアフィン変換と部分射影変換の組み合わせで表すことができる。部分射影変換を求めるための評価基準を，

$$J_{PPT} = \int_D \int_D G\left(\frac{\boldsymbol{x}_1}{1 + \langle \boldsymbol{c}, \boldsymbol{x}_1 \rangle} - \boldsymbol{x}_2\right) \delta(\nabla f(\boldsymbol{x}_1), \nabla g(\boldsymbol{x}_2)) f(\boldsymbol{x}) g(\boldsymbol{x}) d\boldsymbol{x}_1 d\boldsymbol{x}_2$$

と定義する。この $\boldsymbol{c}$ の近似値は，GAT 相関と同様に次式で求めることができる。

$$\boldsymbol{c} = (\overline{\langle \boldsymbol{x}_1, \boldsymbol{x}_1 \rangle \boldsymbol{x}_1})^{-1} (\overline{\langle \boldsymbol{x}_1, \boldsymbol{x}_1 \rangle \boldsymbol{x}_1} - \overline{\langle \boldsymbol{x}_1, \boldsymbol{x}_2 \rangle \boldsymbol{x}_1}) \tag{9}$$

アフィン変換と部分射影変換を交互に収束するまで計算し，その結果を統合して相関を最大にする射影変換とする。そして，そのときの相関値を GPT 相関と定義する。図 1 に，GPT のフローチャートを示す

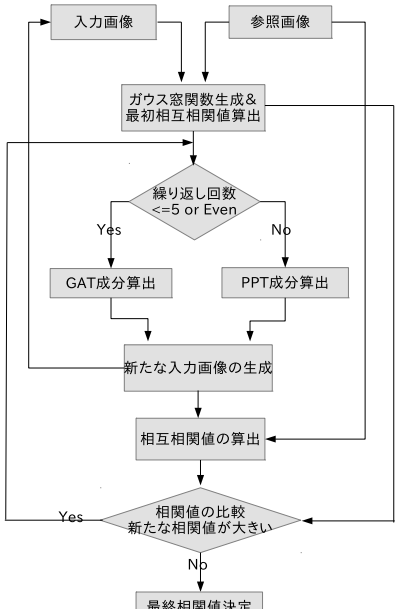

図 1: GPT フローチャート

4 実験結果

手書き数字を使い，射影変換により変形させた画像と原画像の GAT 相関値と GPT 相関値を比較する計算機実験を行った。表 4 にその結果を示す。変形は，$A \sim D$ で表す 4 種類の部分射影変換 $\boldsymbol{c} = (0.01, 0)$, $(0.02, 0)$, $(0, 0.01)$, $(0, 0.02)$，X で表す縦 0.9 倍横 0.75 倍の縮小変換，Y で表す時計方向20°回転，Z で表す縦横を15°傾けるせん断を組み合わせた 12 種類である。表の値は，初期相関値，GAT 相関値，GPT 相関値，GPT 相関値から GAT 相関値を引いたものである。また，BZ 場合の変換画像を図 2 に示す。

表 1: 相関法による相関値

	Org	GAT	GPT	GPT - GAT
AX	0.8144	0.9631	0.9901	0.0270
BX	0.7938	0.8796	0.9758	0.0962
CX	0.7370	0.9453	0.9625	0.0172
DX	0.6746	0.8618	0.8861	0.0243
AY	0.5252	0.9456	0.9542	0.0086
BY	0.4845	0.8845	0.9469	0.0624
CY	0.5211	0.9234	0.9398	0.0164
DY	0.4734	0.7620	0.8856	0.1236
AZ	0.6633	0.9600	0.9965	0.0365
BZ	0.6023	0.8758	0.9970	0.1212
CZ	0.6573	0.9436	0.9909	0.0473
DZ	0.5528	0.8540	0.9111	0.0571

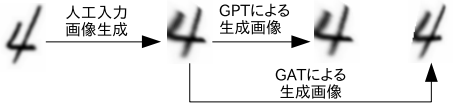

図 2: 変形 BZ による結果の画像

表 4 より，GPT 相関値の方が GAT 相関値の方が，射影変換に対して高い値が得られ，射影変換に対して頑健であることがわかる。

5 おわりに

本論文では，射影変換に対して頑健な相関値を与える GPT 相関を提案し，その有効性を計算機実験によって確認した。今後の課題としては，アフィン変換と部分射影変換の相互の関係を解明し，計算精度を向上させることである。

References

[1] 若原　徹, 小高　和己, 大局的アフィン変換を用いた形状マッチング, 信学技報, PRMU96-2, May, 1996.

[2] 若原　徹, 木村　義政, 山下　喜義, *GAT* 反復を用いたアフィン変換不変の濃淡文字相関法, 信学技報, PRMU99-31, June, 1999.

[3] Toru Wakahara, Yukihiko Yamashita, “Acceleration of GAT Correlation for Distortion-tolerant Image Matching”, Proc. of ICPR 2012, pp746–749, Tsukuba, Dec. 11-15, 2012.

Effect of beam's shape on adhesion between a multi-beam structure and rough surface

Student number：09_24320 name：Takehiko YAZAKI surpervisor：Kunio TAKAHASHI

1. Introduction

Geckos can quickly move on rough surface. This ability depends on adhesion force [1] which occurs between objects and hair structure on their feet. In order to apply this mechanism to development of grip devices, analyzing adhesion force is necessary.

Sekiguchi assumed contacts between a hair structure and objects as a contact between elastic beam and flat surface of a rigid body, and analyzed adhesion force [2]. Using his model, effects of a hair structure's dimensions or elastic module on adhesion force could be discussed, but it could discuss only the uniform shape of a hair structure. Judging from the evidence that a hair structure of geckos has a shape like a spatula, analyzing the adhesion force which is caused by hair structure of various shapes is important. In order to analyze the adhesion force which is caused by hair structure of various shapes, the purpose of this study is to advance Sekiguchi's adhesion model [2] as follows.

1) Modeling a beam of various shapes and analyzing the adhesion force which occurs between the beam and flat surface of a rigid body.
2) Considering contacts between a multi-beam structure and rough surface of a rigid body by superposition to the adhesion force of a single beam.

2. Model

2.1 The model of the contact between a single beam and flat surface of a rigid body.

A beam of various shapes is modeled as a beam which is changed in the distribution of bending stiffness *EI,* expressed as follows.

$$EI = E_0 I_0 \left(1 - \frac{x}{L}\right)^n \qquad (0 \le n < 1)$$

$E_0 I_0$ is *EI* at the base of beam. Figure 1 shows this function.

Figure 2 shows various shapes of beams in response to *n*. If *n*=0, then beam's shape is straight, it is called straight beam in this study. If *n*>0, then the beam's upper surface is curved toward the edge of the bottom of the beam in response to *n*, it is called tapering beam in this study. Deformation of the tapering beam is approximately represented by linear beam theory of a straight beam.

When the beam approaches, loading process, flat surface of a rigid body at angle θ, the beam firstly contacts to the rigid body at the edge of one end of the beam as shown in Fig 3 (a). This contact is called line contact. The rigid body presses the edge of the beam and the beam starts deforming. Consequently, the side surface of the beam adheres to the rigid body as shown in Fig 3 (b) and this contact is called area contact.

The total energy depends on the work of adhesion $\Delta\gamma$, beam's dimensions of the length *L,* width *W,* $E_0 I_0$ and *n*. Now the dimensionless parameter of the work of adhesion is defined as follows.

$$\Gamma = \sqrt{(\Delta\gamma W L^2)/(2\, E_0 I_0)}$$

The energy is determined if the $\Gamma/\tan\theta$ and *n* are set, and the adhered area is equilibrium at the minimum energy condition. From the above, the relation between the displacement *d* and the force *f* is determined and the maximum tensile force which corresponds to arbitrary *d* equals to the grip force.

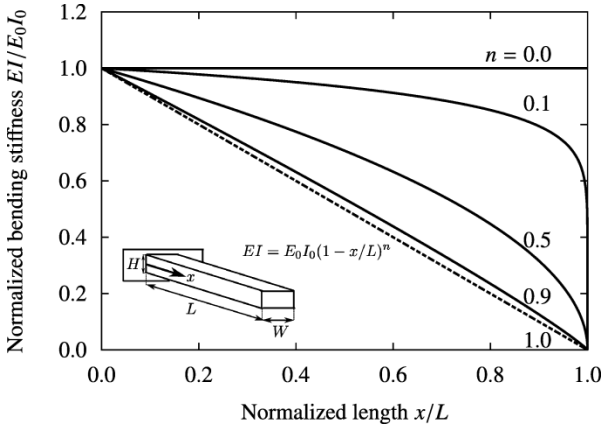

Figure 1: Distribution of the bending stiffness.

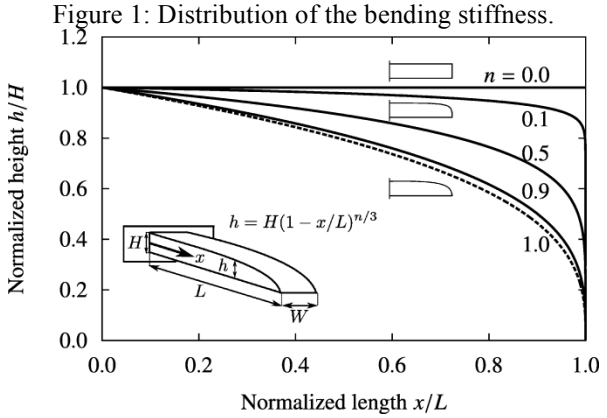

Figure 2: Various shapes of beam in response to *n*.

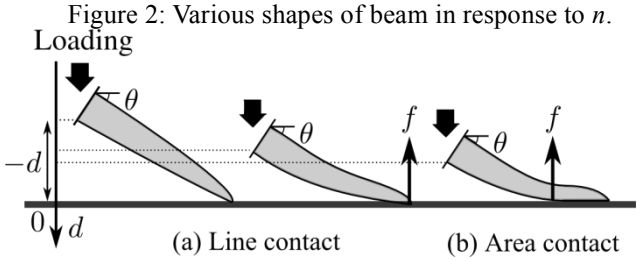

Figure 3: Schematic illustrations of contacts between an elastic beam and flat surface of a rigid body.

2.2 The model of the contact between a multi-beam structure and rough surface.

A multi-beam structure consists of beams of the

same shape fixed to a rigid substrate as shown in Fig 4 (a). Beams are fixed on board at even intervals and even angles θ. The beams are arranged at intervals wide enough to avoid mutual contact. Rough surface of a rigid body is represented as sine wave with amplitude A as shown in Fig 4 (b).

In order to simplify states of a contact between several beams and rigid body surface, the contact area of rigid body surface with several beams is approximated as flat surface is parallel to the multi-beam's substrate as shown in Fig 5. Because of this approximation, the multi-beam structure's force is the sum of the forces between several contact beams and flat surface of the rigid body with different displacements d.

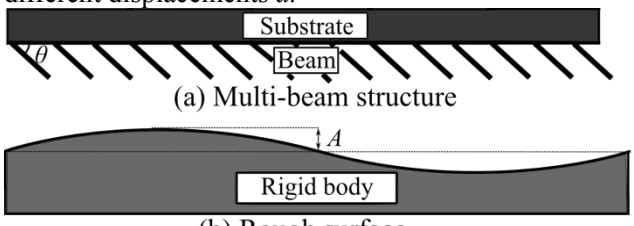

Figure 4: Schematic illustrations of a multi-beam structure and rough surface of a rigid body.

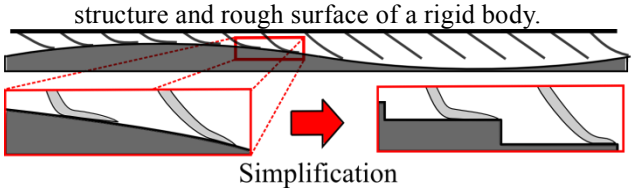

Figure 5: Simplification of contact area of the rigid body.

3. Analysis results and discussion

A numerical simulation was done for analyzing the grip force of a multi-beam structure under the condition that $\Gamma/\tan\theta$ =2.0 and the number of beams is 100.

Figure 6 shows the relation between the amplitude of surface roughness and the grip force of the multi-beam structure in case of the structure consisting of straight beams (n = 0) or tapering beams (n = 0.99). Comparing the two structures of multi straight beam and multi tapering beam, when the amplitude is small the grip force of the multi straight beam structure is relativity larger, when the amplitude is large, the grip force of the multi tapering beam structure is relativity larger. This tendency can be discussed by analyzing contacts between a single beam and a flat surface of rigid body.

If the amplitude of surface roughness is small, the grip force of a multi-beam structure depends on the adhesion force of individual beams. Figure 7 shows the relation between the displacement and the force of a single beam. The adhesion force of a tapering beam is smaller than a straight beam, so the grip force of a multi-beam structure is larger for the case of consisting of straight beams.

If the amplitude of surface roughness is large, the number of beams which adhere to rigid body surface depends on beam's shape, so the structure which consisting of beams adhere easily can cause larger grip force. When $= L\sin\theta/(n-3)$, this means a tapering beam can adhere more easily than a straight beam.

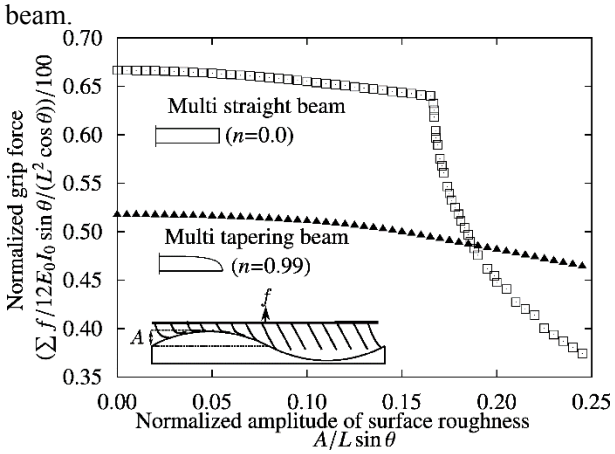

Figure 6: Relation between the normalized amplitude of surface roughness and the normalized grip force of multi-beam structure.

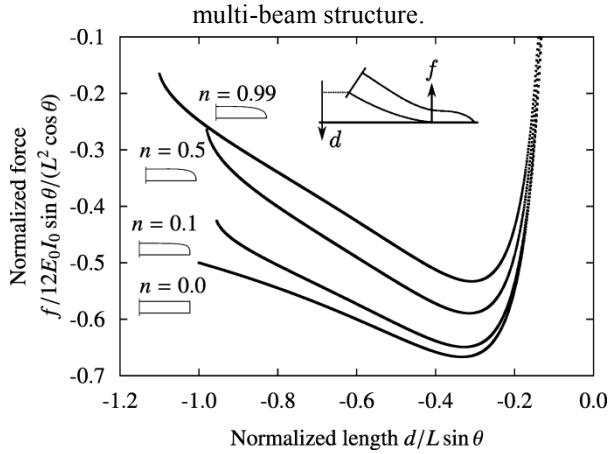

Figure 7: Relation between the normalized force of a single beam and the normalized displacement.

4. Conclusion

The model of a beam of various shapes as shown Fig 2 was proposed. Analysis results of the grip force of multi-beam structures against rough surface of a rigid body showed the possibility that beam's shape can increase application performance to surface roughness.

Reference

[1] K. Autumn, et al., "Adhesive force of a single gecko foot-hair", Nature 405, 2000, 681-685

[2] Yu Sekiguchi, et al., "Adhesion between side surface of an elastic beam and flat surface of a rigid body", Journal of Adhesion Science and Technology Vol. 26, No. 23, December 2012, 2615–2626

Influences of atmospheric conditions to EHD thruster for planetary explorations

Student Number:09-26298 Name: Tianyue Li Supervisor: Yoshihiro MOCHIMARU

1. Introduction

When a high electric voltage such as tens kV is applied to a capacitor of an asymmetric structure, as shown in Fig.1,a net force directing to a physically smaller electrode is generated. This physical phenomenon is called Biefeld-Brown Effect. [1] A thruster based on this effect is usually called Electrohydrodynmaics (EHD) thruster or Asymmetric Capacitor Thruster (ACT).

Because the EHD thruster has simple structure, it is suitable as a propulsion system for in-situ planetary explorations. Although the mechanism of Biefeld-Brown Effect is not clearly understood so far, some basic feature of the EHD thruster has been experimentally investigated. [2] For example, the relationship between a force on the electrode and dimensions of the electrode are one of them. In this study, the EHD thruster in various atmospheric pressures and gas species are experimentally investigated.

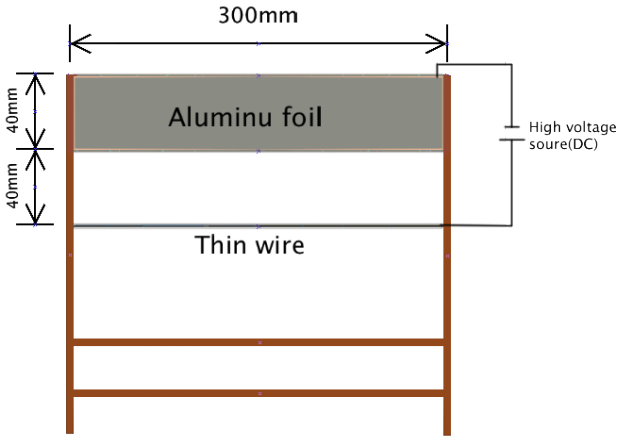

Fig.1 Structure of EHD thruster

2.Experimental method

The experimental system is shown in Fig. 2. The main components of this system are a model of the EHD thruster , an electronic balance, and a DC high voltage power supply. The EHD thruster is placed in a acrylic gas chamber to change the atmospheric conditions around the EHD thruster. As a voltage between asymmetric electrodes changes, a force is measured by the electronic balance. The voltage and current data are monitored and saved in a PC during the measurement.

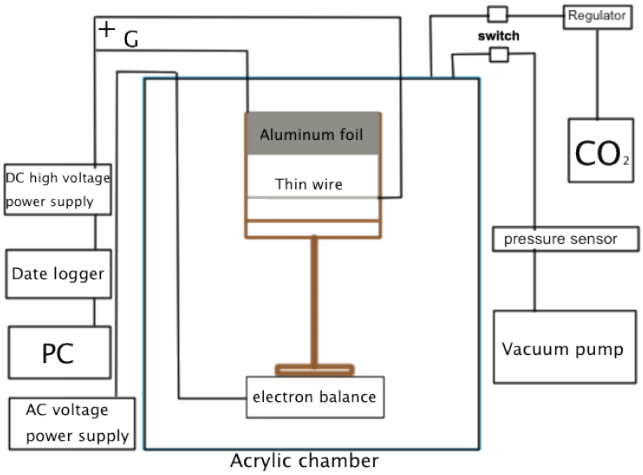

Fig.2 Experimental System

3.Experimental results

Figure 3 shows the relationship between forces on the EHD thruster and atmospheric pressures under various constant applied voltages. In the cases that the applied voltage is relatively low, the EHD thruster obtains a stronger force under a lower atmospheric pressure condition. However, when the applied voltage exceeds a certain threshold, the atmospheric pressure's influence becomes negligible. If the voltage continues to increase, the force becomes proportional to the atmospheric pressure.

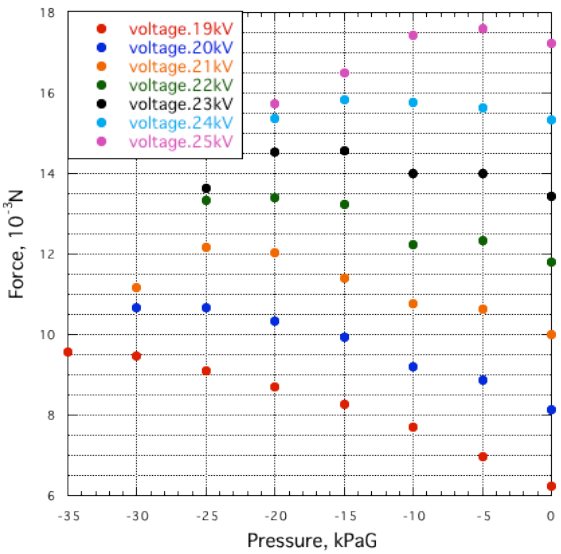

Fig.3 Force on EHD thruster vs. atmospheric Pressure

Figure 4 shows the relationship between the atmospheric pressure and the current. The current becomes lower as the atmospheric pressure is increased. From Fig.3 and Fig.4, we cannot find that the current dominates the propulsion force of the EHD thruster . As voltage changes, the force presents different variation trend with atmospheric pressure.

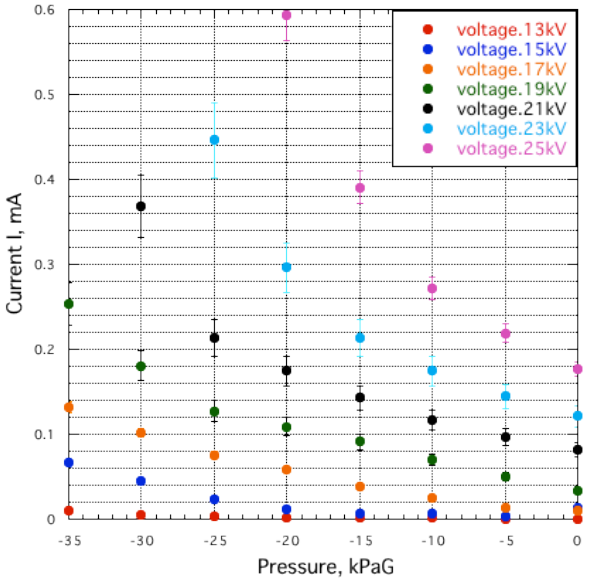

Fig.4 Current vs. Pressure

Figure 5 shows the relationship between the force and the atmospheric pressure under various applied voltages in air or CO_2. EHD thruster in air obtains

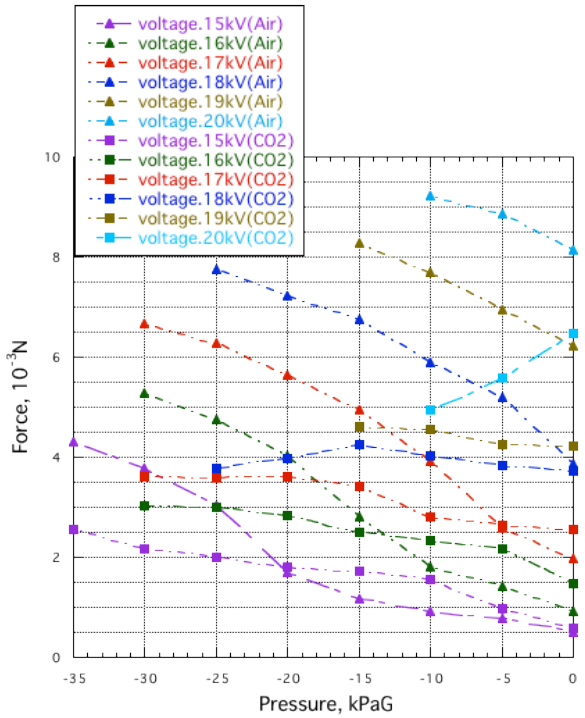

Fig.5 Force vs. Pressure on Air or CO_2

stronger propulsion force than that in CO_2. However, as atmospheric pressure increases, the force in CO_2 increases with the prossure. Therefore, force in CO_2 becomes bigger than that in air at some pressure values.

Figure 6 shows the relationship between the maximum propulsion force on the EHD thruster and the atmospheric pressure in air or CO_2. The maximum force is almost proportional to the atmospheric pressure, in both air and CO_2 under the present experimental conditions.

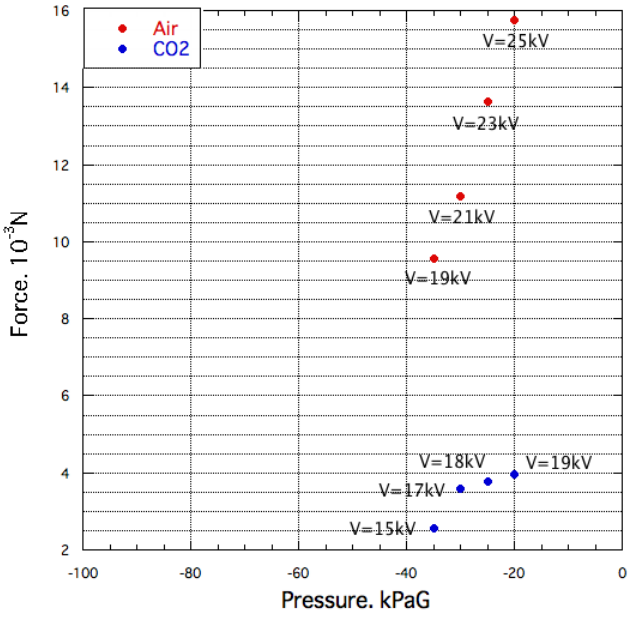

Fig.6 Maximal force vs. Pressure in Air or CO_2

4.Conclusion

In this study, influences of atmospheric conditions to a EHD thruster are investigated. Besides the applied voltage and the dimensions of the EHD thruster, the atmospheric condition is indeed an important parameter. For improvements in the EHD thruster performance, detailed understandings of the ionization and dissociation process of gas particles around the EHD thruster are necesary.

5.References

[1]Biefeld-Brown Effect
http://blazelabs.com/l-intro.asp
access 19 Feb,2013
[2]Wei Liu, “Experiment on Planetary Propulsion System using Electrostatic Force”, graduation thesis Tokyo Institute of Technology,2010

COMPARATIVE ANALYSIS OF AVIATION PASSENGER ATTRIBUTES IN VIETNAM

Student Number: 09-26387 Name: Le Yen Lan Supervisor: Shinya HANAOKA

1 Introduction

Vietnam's economy is developing rapidly during a last few years, thus income level is also increasing. This triggers an increasing aviation demand. Compared with 2007, the number of domestic passenger in 2011 increased 75%. Then, the wave of low-cost carriers (LCCs) has come to Vietnam.

Compared to other Southeast Asian countries, Vietnam is the latest country that LCCs appears after Malaysia, Singapore, Thailand, Indonesia and Philippines. In 2008, after being renamed from Pacific Airlines, Jetstar Pacific Airlines became the first LCC in Vietnam. The second one is VietJet Air which started operation in 2011. There are 2 questions in this research: (1) How is aviation passenger market changed in Vietnam after LCC operation? (2) How different are Vietnam's LCCs compared to other Asian LCCs?

In this research, passenger questionnaire survey was conducted in two biggest airports of Vietnam – Noi Bai airport in Ha Noi (HN) and Tan Son Nhat airport in Ho Chi Minh City (HCM) with two purposes: (1) To clarify Vietnam's LCCs' current situation. (2) To identify and compare the passenger attributes between LCCs and legacy carriers in Vietnam.

2 Results

The number of collected effective samples is more than 2500 in two airports. Major results are shown below.

2.1 Routes and Fare:

VietJet Air has more routes than Jetstar but in some routes Jetstar has more flights than VietJet Air as shown in Table 1. In most routes, the average fare of LCCs was cheaper than Vietnam Airlines (VNA). The durations of survey at Ho Chi Minh City is near Vietnamese Lunar New Year, so fare of LCCs was increased, sometimes more expensive than Vietnam Airlines.

Table 1- Routes, Frequency and Fare

O	D	km	VNA		Vietjet		Jetstar		Sam-ples
			F	AF	F	AF	F	AF	
HN	HCM	1719	16	117	8	73	8	71	1056
HN	DN	759	9	86	2	53	1	61	205
HN	DLat	1481	1	85	1	~	0	~	8
HCM	HN	1719	17	114	8	94	8	101	632
HCM	DN	960	8	90	3	70	3	81	252
HCM	HPh	1618	4	114	1	124	2	97	191
HCM	Vinh	1426	3	107	1	81	2	88	81
HCM	P.Qu	500	5	89	1	46	0	~	37
HCM	Hue	1065	1	91	1	91	0	~	49
HCM	N.Tr	439	4	74	1	44	0	~	41
DN	HCM	960	8	~	4	~	3	~	0
Total									2552

F: frequency (flights/ day)

AF: Average fare (USD)

2.2 Monthly Household Income

Most of Vietnam Airlines' passengers are more than 1500USD in their monthly household income. But most passengers of LCCs are between 400 and 600USD (see Figure 1). Because of the entry of LCCs, middle income earners can travel using airlines.

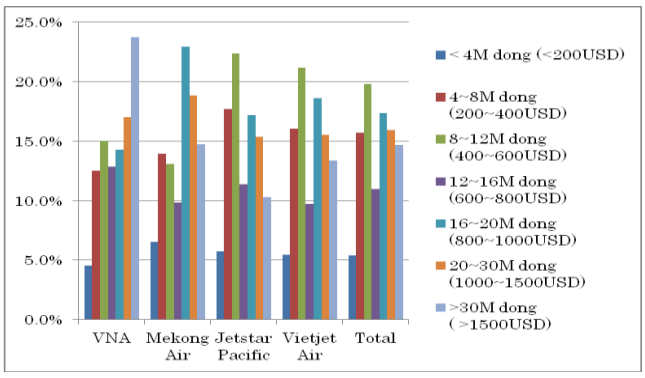

Figure 1: Monthly Household Income

2.3 Travel purpose

Passengers use Vietnam Airlines for work purpose, but use LCCs for other private purposes (see Figure 2). The survey duration is near Lunar New Year in HCM, so passengers who use for "back home" purpose are more numerous than usually.

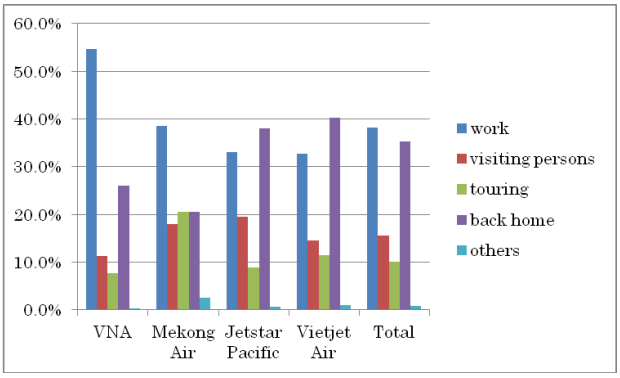

Figure 2: Travel purpose

2.4 Reasons of choosing airlines

Figure 3 shows the result of survey question "What are the reason to choose this airline this time for comparing with other airlines?". Based on the result, passengers choose LCCs because of low fare, suitable flight time and convenient ticket. On the other hand passengers use legacy carriers because of less delay, no cancel flight, safety, well-known and comfortable seat.

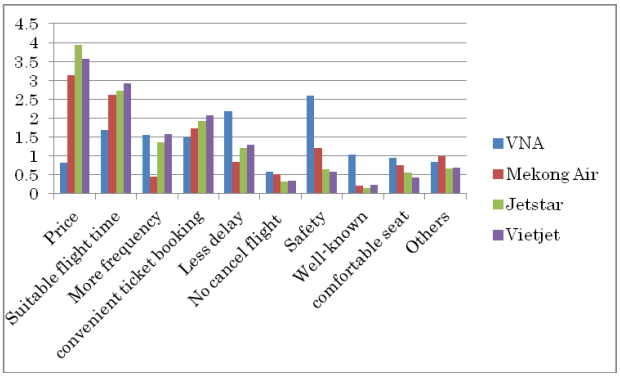

Figure 3: Reasons of choosing airlines

2.5 Transport mode before using aviation

There are many new demands on both of Vietnam Airlines and LCCs. There are many LCCs demand shift from rail and bus (see Table 2).

Table 2: Previous transportation of air transport's first boarding passengers

	VNA	Mekong Air	Jetstar Pacific	VietJet Air
Never use	60	10	87	106
Rail	35	11	106	120
Bus	22	8	94	76
Car	4	0	6	5
Other	1	0	0	1
Total	122/577	29/126	293/877	308/957

2.6 Alternative choice

Most people will choose other airlines if it meets their schedule. More users of Vietnam Airlines will choose same airline than other airlines. The ratio of LCCs' users who will choose bus or railway is higher than Vietnam Airlines' users. One of possible reason is that fare of LCCs is not much more expensive than bus or train, but fare of Vietnam Airlines is much more expensive.

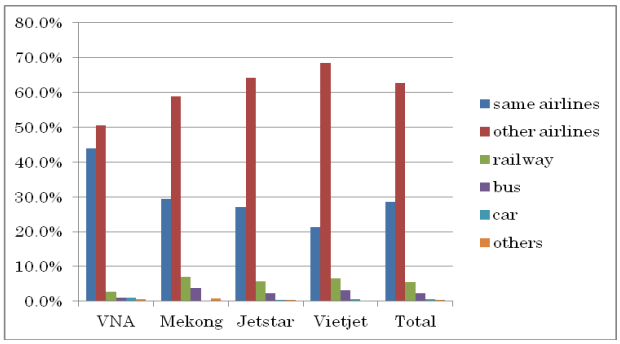

Figure 4: Alternative choice

3 Conclusion

With the entry of low-cost carriers, Vietnam aviation market has changed significantly. More persons who are lower income can travel by air transport. And more people who used to use bus or train changed to use air. People can use air transport for other private purposes than before.

Vietnam's economy will continue to develop and demand for aviation will potentially increase. It creats more opportunity for LCCs to operate in Vietnam.

Prediction of Indoor MIMO Channel for Specific Systems using Ray Tracing Simulation

学籍番号: 10B15328　名前: チョウ　カツシ　指導教員: 高田　潤一・金　ミンソク

1　概要

現在, 無線通信技術への期待は高まる一方で, 周波数資源の需要もそれと共に増えている. その結果 3 GHz 以下の周波数帯域は隙間なく割当られ, 周波数が枯渇するという厳しい現状になってきた. 解決策として高周波数帯における通信技術の開発が強く求められている. また周波数資源を有効に利用して通信の高速化を図るために, MIMO 技術の導入が期待される [1]. 周波数が高くなるにつれて回折の効果が小さくなり，マルチパスの効果が減少するため，特に 10GHz を超える高い周波数帯における MIMO チャネルの特性は，現在の無線通信で用いられている 6GHz 以下の周波数とはかなり異なると考えられる.

このようなチャネルの特性を調べるためには, サウンディング実験 [2] – [5] が広く用いられているが, 実験するためのコストが膨大である. 本論文では，レイトレースシミュレーションによるチャネル特性の予測に注目し，サウンディング実験の結果と比較することでシミュレーションの適用範囲と誤差要因を検討することを目的としている.

まずは 11 GHz において屋内サウンディング実験を行った, 次に実験環境における構造物をモデル化してレイトレースシミュレーションを行った. シミュレーション結果は無限の角度・遅延時間分解能を有するため，実測結果と直接比較することは困難である. 本研究では，レイトレースシミュレーションの結果から，アンテナ指向性と測定信号の帯域幅を考慮して，予測される実験結果を算出し，実際の実験結果と比較検討を行った. 比較には遅延スペクトル及び双角度スペクトルを用いた. 比較結果から，シミュレーションの妥当性と誤差要因を考察した.

2　屋内 MIMO チャネルサウンディング実験

東京工業大学大岡山キャンパス百年記念館（図 1）において、MIMO チャネルサウンディング実験を行った。実験を表 1 のようなパラメータで行った [2]。

実験で得られたデータは各アンテナ間の複素電力からなる伝達関数である。

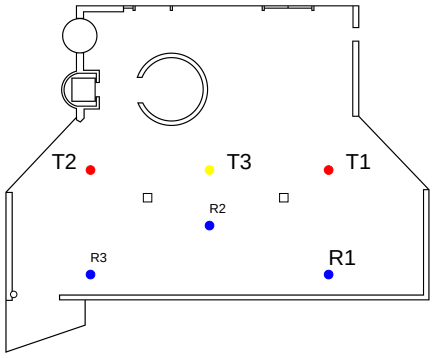

図 1: 百年記念館

表 1: 実験パラメータ

周波数	11 GHz
帯域幅	400 MHz
アンテナ高さ	1.7 m
アンテナ	偏波多重 12 素子円形アレー

3　レイトレースシミュレーション

レイトレースシミュレーションには商用シミュレータである RapLab [4] を使用した. レイトレースシミュレーションは幾何光学近似に基づき，電波を光に見立て，パスを検索する [6]. RapLab の場合には，拘束条件として最大反射回数・最大回折回数を与えることで，有限個のパスが探索される. 具体的なシミュレーションのパラメタは表 2 の通りである.

レイトレースシミュレーションをすることにより，パス損失，遅延，放射方向，到来方向などが分かるが. シミュレーション結果はそのまま実験結果と比較できないため，本論文ではシミュレーション結果に実験条件の帯域制限とアンテナ応答を適用し，予測される実験結果を求めている [7] [8].

4　実験結果とシミュレーション結果の比較

MIMO 伝送は次の式でモデル化される.

$$\mathbf{y}(f) = \mathbf{H}(f)\mathbf{x}(f) + \mathbf{n}(f) \tag{1}$$

$\mathbf{x}(f)$ は送信信号スペクトル，$\mathbf{y}(f)$ は受信信号スペクトル，$\mathbf{n}(f)$ は雑音スペクトルであり，$\mathbf{H}(f)$ は MIMO チャネル伝達関数である. 実験で測定した結果とシミュレーションの結果に対し同じ手法で解析を行う. 遅延スペクトルは伝達関数のフーリエ逆変換より求めることができる. 双角度電力スペクトルは，角度に対する

表 2: シミュレーションパラメータ

周波数	11 GHz
帯域	無限大
アンテナ高さ	1.7 m
最大反射回数	2 回
最大回折回数	1 回
構造物の媒質モデル	コンクリート

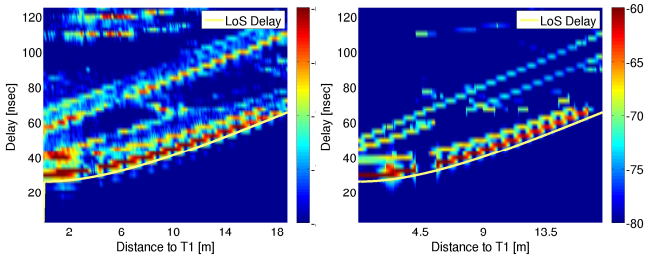

測定結果　　シミュレーション結果

図 2: 遅延スペクトル

アレー応答ベクトルを用いて，ビームフォーミングにより次の式で求められる．

$$Y_f(\varphi_{\mathrm{T}}, \varphi_{\mathrm{R}}) = \frac{\mathbf{a}_f^H(\varphi_{\mathrm{R}})\mathbf{H}_f\mathbf{a}_f^*(\varphi_{\mathrm{T}})}{||\mathbf{a}_f^H(\varphi_{\mathrm{R}})||^2||\mathbf{a}_f(\varphi_{\mathrm{T}})||^2} \tag{2}$$

$\mathbf{a}_f(\varphi_{\mathrm{R}}), \mathbf{a}_f(\varphi_{\mathrm{T}})$ はそれぞれ受信アンテナ，送信アンテナのアレー応答ベクトルである [2] [3] [9].

図 2 は送信点を T1 から T2 まで直線的に移動したときの測定結果及びシミュレーション結果より得られた遅延スペクトルである．図 2 より，モデルの材質の反射率が異なるため，レベルの差が見られるが，直接波（LoS）と電力の強い一回反射波は双方で一致している．遅延の大きいパスについては，正しく推定できなかった．

図 1 の T1 と T2 の中点 (T3) における双角度スペクトルが図 3 である．図 2 と同様にシミュレーションでは，直接波と一部の一回反射波のみ推定され，電力の強いパスの角度をすべて推定するのは困難だった．シミュレーションでは建物壁面のみを考慮しているのに対して，実験では，多くの椅子やテーブルなどの物体が配置されていた，従って誤差の主原因は，レイトレースシミュレーションで考慮されていない物体の影響と考えられる．レイトレースでは幾何光学近似を用いるため，比較的小さい物体や表面が複雑な形状に対する散乱を正しく取り扱うことができない．したがって，物理光学近似など，より近似度の高い解法を導入して，これら小物体の散乱を考慮することで，シミュレーションの確度を上げることができると期待される [4] [6].

5　結論

本研究ではサウンディング実験結果をビームフォーミングの手法で解析した．またモデル化した環境においてレイトレースシミュレーションをし，それにアンテナ指向性と測定信号の帯域幅を考慮して予測結果を算出した．実験結果とシミュレーション結果を比較することで以下のような結論を得た．

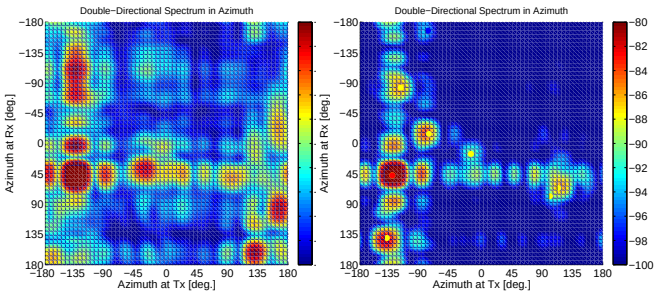

測定結果　　シミュレーション結果

図 3: 角度スペクトル

シミュレーションはコストは小さいが，周囲の環境を想定していないためシミュレータの精度が高くない．また，レイトレースによりチャネルの特性を正しく推定できることに加え，直接波を含めいくつかの強いパスも正しく推定できる．しかし，それぞれの位置におけるチャネルの詳細な性質や弱いパスの推定には限界がある．

今後の研究ではシミュレーションの精度と実用性をあげる．具体的には，小さい物体を単純な形状で近似してモデル化することでシミュレーション確度が上がるかどうかを検討する．

参考文献

[1] 大種武雄・小川恭孝, 分かりやすい MIMO システム技術, オーム社, 2009.

[2] 菊間信良, アダプティブアンテナ技術, オーム社, 2003.

[3] Andreas F. Mollisch, *Wireless Communications*, WILEY, Now York, USA, 2005.

[4] Raplab Kozo Keikaku Engineering Inc., ”http://www4.kke.co.jp/network/raplab/index.html”

[5] Andrea Goldsmith, *Wireless Communications*, Cambridge, New York, USA, 2005.

[6] 吉敷由起子, レイトレース法を用いた電波伝搬シミュレーションのための非幾何光学の手法の導入, 東京工業大学博士論文, 2011.

[7] Andreas Richter, *Estimation of Radio Channel Parameters: Models and Algorithms*, Doctoral Thesis, Ilmenau University of Technology, 2005.

[8] Martin Steinbauer, *The Radio Propagation Channel – A Non-Directional, Directional and Double-Directional Point-of-View*, Doctoral Thesis, Technical University of Vienna, 2001.

[9] Yuyuan CHANG, et.al. ”Analysis of Field Measurement with Wideband MIMO Sounder at 11 GHz Frequency”, IEICE, Technical Report, AP2012-153 Jan 2013.